AN ADJUSTABLE IMPEDANCE MATCHING NETWORK USING RF MEMS TECHNOLOGY

A THESIS SUBMITTED TO
THE GRADUATE SCHOOL OF APPLIED AND NATURAL SCIENCES
OF
THE MIDDLE EAST TECHNICAL UNIVERSITY

BY

MEHMET ÜNLÜ

IN PARTIAL FULFILMENT OF THE REQUIREMENTS FOR THE DEGREE OF
MASTER OF SCIENCE
IN
THE DEPARTMENT OF ELECTRICAL AND ELECTRONICS ENGINEERING

SEPTEMBER 2003

Approval of Graduate School of Natural and Applied Sciences.

_____

Prof. Dr. Canan ÖZGEN
Director

I certify that this thesis satisfies all the requirements as a thesis for the degree of Master of Science.

_____

Prof. Dr. Mübeccel DEMİREKLER
Head of Department

This is to certify that we have read this thesis and that in our opinion it is fully adequate, in scope and quality, as a thesis for the degree of Master of Science.

Asst. Prof. Dr. Şimşek DEMİR Supervisor	Assoc. Prof. Dr. Tayfun AKIN Co-Supervisor

Examining Committee Members

Prof. Dr. Canan TOKER _____

Prof. Dr. Altunkan HIZAL _____

Asst. Prof. Dr. Şimşek DEMİR _____

Assoc. Prof. Dr. Tayfun AKIN _____

Ümit Kenan ÇAĞLAR _____

ABSTRACT

AN ADJUSTABLE IMPEDANCE MATCHING NETWORK USING RF MEMS TECHNOLOGY

Ünlü, Mehmet
M. Sc., Department of Electrical and Electronics Engineering
Supervisor: Asst. Prof. Dr. Şimşek Demir
Co-Supervisor: Assoc. Prof. Dr. Tayfun Akın

September 2003, 137 pages

This thesis presents design, modeling, and fabrication of an RF MEMS adjustable impedance matching network. The device employs the basic triple stub matching technique for impedance matching. It has three adjustable length stubs which are implemented using capacitively loaded coplanar waveguides. The capacitive loading of the stubs are realized using the MEMS switches which are evenly distributed over the stubs. There are 40 MEMS bridges on each stub which

are separated with λ/40 spacing making a total of 120 MEMS switches in the structure. The variability of the stub length is accomplished by closing the MEMS switch nearest to the required stub length, and making a virtual short circuit to ground. The device is theoretically capable of doing matching to every point on the Smith chart.

The device is built on coplanar waveguide transmission lines. It has a center operating frequency of 10GHz, but because of its adjustability property it is expected to work in 1-40GHz range. It has dimensions of $8950 \times 5720 \mu m^2$.

This work is the continuation of the first national work on fabrication of RF MEMS devices. The device in this work is fabricated using the surface micromachining technology in the microelectronic facilities of Middle East Technical University.

Keywords: Impedance matcher, RF MEMS, capacitively loaded line, CPW, micromachining.

ÖZ

RF MEMS TEKNOLOJİSİ İLE AYARLANABİLİR EMPEDANS UYUMLAMA DEVRESİ

Ünlü, Mehmet
Yüksek Lisans, Elektrik ve Elektronik Mühendisliği Bölümü
Tez Yöneticisi: Yrd. Doç. Dr. Şimşek Demir
Ortak Tez Yöneticisi: Doç. Dr. Tayfun Akın

Eylül 2003, 137 sayfa

Bu tez RF MEMS ayarlanabilir empedans uyumlama devresinin tasarım, modelleme ve üretimini sunmaktadır. Aygıt empedans uyumlama için temel üç kütüklü empedans uyumlama tekniğini kullanmaktadır. Aygıtın üç adet, sığal (kapasitif) yüklenmiş eşdüzlemli dalga kılavuzu olarak inşa edilmiş ayarlanabilir uzunlukta kütüğü bulunmaktadır. Kütüklerin sığal olarak yüklenmesi kütükler üzerine eş aralıklarla yerleştirilmiş MEMS anahtarlarla gerçekleştirilmektedir. Her

kütük üzerinde $\lambda/40$ aralıklarla yerleştirilmiş 40, toplam olarak da aygıtta 120 MEMS anahtar bulunmaktadır. Kütük uzunluğunun ayarlanabilirliği istenen uzunluğa en yakın MEMS anahtarın kapatılması ve toprağa sanal bir kısa devre yapılmasıyla sağlanmaktadır. Aygıt teorik olarak Smith abağı üzerinde her noktaya uyumlama yapma yeteneğine sahiptir.

Aygıt, iletim hattı olarak eşdüzlemli dalga kılavuzu kullanmaktadır. Aygıtın çalışma frekansı 10GHz'dir, ama aygıtın ayarlanabilirlik özelliğinden dolayı aygıtın 1-40GHz arasında çalışması beklenmektedir. Aygıtın boyutları $8950 \times 5720 \mu m^2$'dir.

Bu çalışma RF MEMS aygıtların üretimi üzerine yapılan ilk ulusal çalışmanın devamıdır. Bu çalışmadaki aygıt yüzey mikroişleme teknolojisi ile Orta Doğu Teknik Üniversitesi mikroelektronik tesislerinde üretilmiştir.

Anahtar kelimeler: Empedans uyumlayıcı, RF MEMS, sığal (kapasitif) yüklenmiş hat, eşdüzlemli dalga kılavuzu, mikroişleme.

To my parents and brothers...

ACKNOWLEDGEMENTS

I would like to thank my advisors Prof. Şimşek Demir for his sincere friendship, guidance, and support at my hard times, and Prof. Tayfun Akın for his friendship, support, and encouragement for this nice work. I owe much to both of them.

I also would like to thank Prof. Semih Sencer Koç and Prof. Özlem Aydın Çivi for their innovative ideas and contribution to this research. I would like to acknowledge Prof. Altunkan Hızal for sharing his great theoretical and experimental experience and providing the millimeter wave laboratory.

It is a pleasure to thank my brother Kağan Topallı for everything he did in these two beautiful years. Without him, my life would be much more difficult and boring. I am also grateful to Hüseyin Sağkol, The Master, for his great friendship and the great times we had together. He had a contribution in every single thing I did here.

I would like express my appreciation to thank Orhan Akar. He is a very nice man and a real professional. I would like to thank Said Emre Alper, Refet Fırat Yazıcıoğlu, and Mehmet Akif Erişmiş for their great friendship and support during processing, Murat Tepegöz and Dr. Selim Eminoğlu for nice chats and computer support, Burak Okcan, Mahmud Yusuf Tanrıkulu, Özge Zorlu, Mustafa Seçmen, and the other MEMS group members for their friendship.

I also would like to thank Dr. Deniz Sabuncuoğlu Tezcan and Mahmud Yusuf Tanrıkulu for the SEM sessions, METU III-V group members for process support, and METUMET staff for their patience and support.

My very special thanks go to my parents, my grandfather and first master Kenan Kul, and my whole family for their eternal love and support.

This research is supported by TÜBİTAK BİLTEN.

TABLE OF CONTENTS

ABSTRACT ..... **iii**
ÖZ ..... **v**
DEDICATION ..... **vii**
ACKNOWLEDGEMENTS ..... **viii**
TABLE OF CONTENTS ..... **x**
LIST OF TABLES ..... **xii**
LIST OF FIGURES ..... **xiii**
CHAPTER
1. INTRODUCTION **1**
1.1 RF MEMS: History and General View 3
1.2 Previous Work on Adjustable Impedance Matchers 7
1.3 The Impedance Matching Network Developed in This Thesis 9
1.4 Research Objectives and Organization of the Thesis 11
2. THEORY OF IMPEDANCE MATCHER AND ITS MEMS IMPLEMENTATION **14**
2.1 Stub Matching 14
2.1.1 Single-Stub Matching 15
2.1.2 Double-Stub Matching 16
2.1.3 Triple-Stub Matching 20
2.2 Coplanar Waveguides 23
2.2.1 Conductor-Backed Coplanar Waveguides (CBCPW): Basic expressions 24
2.2.2 Dispersion and Effects of Metallization Thickness 25

2.2.3 Losses in CPW 26
2.3 MEMS Shunt Capacitive Switch 28
2.3.1 Mechanical Properties 29
2.3.2 Electromagnetic Model 36
2.4 Capacitively-Loaded Distributed Transmission Lines 43
2.4.1 Analysis of Capacitively Loaded MEMS CPW 43
2.4.2 Loss of the Capacitively Loaded MEMS CPW 48
3. DESIGN OF MEMS IMPEDANCE MATCHER 50
3.1 CPW Design 51
3.2 Shunt, Capacitive MEMS Switch Design 56
3.2.1 Mechanical Design Phase 57
3.2.2 Electromagnetic Design Phase 59
3.3 Variable Length MEMS Stub Design 69
3.4 MEMS Triple Stub Matcher 88
3.5 Conclusion 96
4. FABRICATION OF THE MEMS IMPEDANCE MATCHER 98
4.1 Mask Drawing 99
4.2 Materials Used and Their Deposition Techniques 102
4.3 Process Flow 106
5. FABRICATION AND TEST RESULTS OF THE MEMS IMPEDANCE MATCHER 111
5.1 RF Measurement Setup 113
5.2 First Metallization Measurements 115
5.3 Stub Measurements 117
5.4 SEM Pictures 119
6. CONCLUSION AND FUTURE WORK 122
REFERENCES 125
APPENDIX 135

LIST OF TABLES

TABLE

3.1 The dimensions and the characteristic impedances of the CPWs used in the impedance matchers. 53

3.2 Losses for the CPW lines. All are in dB/cm. 53

3.3 Up and down state capacitance values for MEMS switches. 61

3.4 (a) to (c) The values of the new MEMS switch model used in fitting. 67

3.5 The schematic element values of the proposed model that is used to fit the simulation results. 85

3.6 The element values for the transmission line-capacitor model that is used to fit the simulation results. 86

3.7 The input impedance values of the variable length stub with different switch positions actuated. 87

5.1 Calibration coefficients of Picoprobe 40A-GSG-150P CPW probe [79].. ... 115

LIST OF FIGURES

FIGURE

1.1 3D view of the MEMS variable impedance matching network. 10
1.2 The schematic of the variable impedance matching network. 11
2.1 Single-stub matching..... 15
2.2 Schematic of double-stub matcher. 17
2.3 Double-stub matching steps shown on the Smith chart [60]. 18
2.4 The limitations of the double-stub matching (for $d = \lambda/8$) [60]. 20
2.5 Schematic of the triple-stub matching..... 21
2.6 The use of third stub to guarantee the matching for $d = \lambda/8$ [60]. 22
2.7 Coplanar waveguide structure. 24
2.8 Shunt, capacitive, RF MEMS switch [59]. 29
2.9 The diagram of a fixed-fixed beam with force applied uniformly over the entire beam…… 30
2.10 The dimensions and the forces on the fixed-fixed beam..... 32
2.11 The equivalent circuit for the MEMS shunt switches [21]. 37
2.12 (a) The general unit section for a capacitively loaded line. (b) Cascade connection of unit sections. 44
2.13 (a) MEMS capacitively loaded CPW line top view (b) its lumped element unit section [21]. 46
3.1 CBCPW structure with dimensions. 52
3.2 (a)-(b) HFSS simulation results for the unloaded CPW designs..... 55
3.3 Mechanical structure of the shunt, capacitive MEMS switch. 57
3.4 Change in the actuation voltage due to residual stress for $W = 74$ μm. 58

3.5 The fitted MEMS switch model. 62
3.6 Field distribution of a CBCPW with a top cover [76]. 63
3.7 (a) to (f) S-parameters of the switches with total lengths 200μm, 260μm, 420μm. 67
3.8 The HFSS model for an 8-bridge stub. 70
3.9 (a) to(c) The field distribution of the simulated MEMS variable length stub. 72
3.10 Schematic model for a 4 bridge MEMS variable stub. 73
3.11 (a) to (t) Imaginary and real parts of Z_{11} obtained from HFSS EM simulations and the proposed model. 84
3.12 The model used to fit the T-junction. 89
3.13 (a) to (e) S-parameters of the EM simulated and modeled T-junction. 92
3.14 The Microwave Office circuit used for final simulations. 93
3.15 The comparison of solutions selected from ideal set and all combinations. . 94
3.16 (a) to (b) Real and imaginary part of input impedance seen into the matcher when it is set to transform different impedances to desired values..... 96
4.1 General device structure of the MEMS impedance matcher. 100
4.2 (a) to (b) Masks drawn for the production of MEMS variable length stub... 101
4.3 Process flow for the first metallization (a) Adhesion layer Ti (gray) and seed layer Cu (light brown) are coated, and photoresist is coated and patterned for electroplating (pink). (b) Cu is electroplated for first metallization (dark brown), and Au coated as the cover layer (yellow). (c) Au is patterned using lift-off technique. (d) Ti and seed Cu layers are etched. Cover Au layer protects the electroplated Cu underneath during the etching. 104
4.4 (a) to (i) The process flow followed during the production of MEMS impedance matchers. 110
5.1 Photograph of the RF testing setup used for MEMS variable impedance matcher measurements. 113
5.2 (a) to (b) Simulated and measured S-parameters of the first metallization... 117
5.3 (a) to (b) Measurement results for 20-bridge MEMS short-circuited stub. .. 119
5.4 Two stubs of the MEMS adjustable impedance matching network..... 120

5.5 A closer view of a stub of the MEMS impedance matching network. 120
5.6 Close view of the MEMS bridge that is used to load the CPW. 121

CHAPTER I

INTRODUCTION

Impedance matching has always been a major problem of the microwave and millimeter-wave systems. It can be generally defined as the problem of adjusting the input impedance of a device to match the output impedance of another device to which it is connected. Impedance matching is required to minimize the power reflection from the connection point, and hence maximize the power transfer in between the devices. For most of the cases, the input or output impedance of the device are constant or changing them may alter the device characteristics, thus another device, which has an input and output impedance to match both devices, is required. This device is an impedance matching network. The impedance matching networks are expected to have little insertion loss, wide band, and high performance as a general necessity for a microwave component.

As microwave and millimeter-wave technology has advanced considerably in the last few decades by concentrating on fabricating high performance and low cost systems, the requirements on the impedance matching networks have also increased as well as the other microwave components. The components are awaited to have small dimensions and to be compatible with the common production techniques in addition to being low loss, wide band, and high

performance. This is because of the basic aim of the technology is towards to build system in which all parts of the system are fabricated monolithically, in other words to build systems on a chip. Since the new systems are also targeted to be dynamic in terms of operation frequencies, the components are being compelled to work at different frequencies as well, which, indeed, creates the need for adjustable components.

The need for low cost, low size, high performance, wide band, and adjustable impedance matching networks is first attempted to solve with the IC technology. The possibility of using FETs in IC technology gives one chance to build variable impedance matching networks [1]-[3]. The invention of micro electromechanical systems (MEMS) technology and its application of this technology to RF systems, however, have given a new and broader sight to the researchers. With this new technology, it is possible to fabricate adjustable passive components with very high performance, very low power dissipation, very high linearity, and very low cost.

This thesis proposes a new type of variable impedance matcher that is fabricated monolithically using the MEMS technology. Using the conventional triple stub matching theory, the matching is obtained by setting the stubs' lengths to the calculated values. The variable length stubs are obtained using the MEMS capacitive shunt switches which are periodically placed with $\lambda/40$ spacing over the stubs of the variable impedance matcher in a loaded line manner. To obtain a stub with a fixed length, the MEMS switch closest to the corresponding length is closed, forming a virtual short circuit to ground. In this case, a short circuited stub with the predefined length is obtained. The stubs, which are used to add susceptances to the main line to have a matched circuit, have a maximum length of $\lambda/2$ that can allow any susceptance value to be used. It is advantageous over the double stub matchers which can only match a limited area on the Smith chart. The monolithic fabrication procedure prevents the parasitic effects coming from the

junction points. With the use of three stubs which has a length of λ/2, the MEMS variable impedance matcher can theoretically transform any given impedance point on the Smith chart to any other desired impedance point. However, since the stub length will be equivalent to more than an electrical length of λ/2 for frequencies greater than 10GHz, the device can work for any other frequency up to the cut off frequency of the MEMS switches. The total die area of the MEMS variable impedance matcher is $8950 \times 5720 \mu m^2$.

This chapter briefly summarizes the work of this thesis. Subsection 1.1 explains the history of MEMS devices which are crucially important to understand the MEMS variable impedance matchers. Subsection 1.2 summarizes the previous research on variable impedance matcher including MEMS impedance matchers. Subsection 1.3, finally, gives the basic details of the work contained in this thesis and the organization of the thesis.

1.1 RF MEMS: History and General View

Microelectromechanical systems have been researched since 1970s for different types of sensors and accelerometers, but application of MEMS technology to the high frequency systems dates only back to start of 1990s. The first RF MEMS structure was a MEMS relay for microwave applications which was produced in 1991 [4]. Though the device was not mature, the performance of the device was outstanding, so the researchers focused on the subject. In 1995, following the idea, one series for DC to 60GHz and one parallel for 10 to 120GHz MEMS switches are produced by Rockwell Science Center and Texas Instruments respectively [5]-[6]. Many types of MEMS switches are developed such as low-spring constant shunt [7]-[8], high capacitance ratio [9]-[10], shunt DC contact [11]-[12], series DC contact [13]-[14], inline DC contact [15]-[16], push-pull type actuated shunt [17], thermally actuated DC contact [18],

magnetically actuated series [19], lateral DC contact [20], piezoelectrically actuated [21], and rotary [21] switches with the increasing amount of researchers all around the world on RF MEMS in the mean time.

The application of MEMS as RF components is not limited with the MEMS switches. Inductors [22]-[25], tunable capacitors and varactors [26]-[31], transmission lines [32]-[34], high-Q micromechanical filters [35]-[36], and thin film bulk acoustic resonators (FBAR) [37] are also fabricated using MEMS technology using the basic idea of electromechanical operation principles.

Other than using single RF MEMS circuit elements, it is possible to make more complicated RF circuits using the basic elements of the RF MEMS technology. One important type of component is the MEMS loaded lines. Capacitively loaded MEMS transmission lines are implemented placing MEMS variable capacitors or switches over a transmission line. Changing the MEMS loading capacitance values changes the phase velocity of the wave traveling in the device, hence it is possible to fabricate MEMS phase shifters depending on this basis [38]-[41]. In addition to loaded line type phase shifters, it is also possible to design reflective analog and digital type [42]-[43] and switched line digital type [44]-[46] MEMS phase shifters which employ MEMS switches and MEMS variable capacitors. Other types of adjustable elements that use MEMS switches and actuators are tunable antennas [47]-[49], tunable frequency selective surfaces [21], tunable resonators [21], and tunable filters [50]-[52].

The basic advantages that all RF MEMS devices offer can be summarized as follows:

- Near zero power consumption: Most MEMS devices are actuated electromechanically, so they consume power only during the switching between its states, and this power dissipation is about 0.05-0.1mW including the voltage upconverter and the drive circuitry [21].

- Very low loss: MEMS technology offers RF devices with very low loss. The reported loss of MEMS switches are 0.05-0.2dB for 1-100GHz [21]. MEMS phase shifters also offer an average loss of -0.6/bit for Ka-band applications [21].
- Very high isolation (for switches): MEMS switches offer very high isolation up to frequencies of 100GHz. For series switches, this is because of the up state capacitance values that are as low as 2fF. In addition, it is possible to design tuned switches to obtain at least more than -20dB isolation for a band of 20-30GHz at Ka, V, and W bands [21].
- Intermodulation products: Since the MEMS devices contain no semiconductor or any other nonlinear components, they are extremely linear and they propose very low intermodulation products. For MEMS switches, the performance is about 30dB better than its rivals PIN or FET switches.
- Adjustability: The electromechanical movement provided by the MEMS technology allows one to design adjustable components such as filters and matching networks.

Even though MEMS components have very good performance values, the following problems have not been solved yet:

- Low speed: The speed of the devices is relatively low compared to semiconductor devices. This is because of the low resonant frequencies of its mechanical structure. MEMS switches have a switching time of 1-300μs [21].
- High actuation voltage: The MEMS switches have actuation voltages of 20-80V [21] which are not suitable for most of the systems. However, this voltage amount is required with very little amounts of current; a simple DC-DC converter can handle the problem.

- Power handling: MEMS switches can only handle medium power levels such as 30-300mW for capacitive switches and 10-100mW for DC contact switches [21].
- Reliability: MEMS switches were tested to work more than 1 billion cycles. Examples, which are tested for more than 25-60 billion cycles, are also present [21]. However, these values are not sufficient for today's wireless systems some of which require more than 100 billion cycles. It is believed that MEMS switches with more than 100 billion switching cycles can be produced.
- Packaging: The operation of RF MEMS devices is affected by the environment conditions for long term operations, so a good packaging requires. The packaging increases device cost and can affect the device performance.

With the above mentioned properties of RF MEMS elements, they are candidates to be used in many applications which can be summed up under four titles: switching networks, low-noise and low-power circuits, portable wireless systems, and phased arrays. One possible application of MEMS switching networks is satellite systems where high isolation, low insertion loss, low intermodulation products, and high power switches are needed. The cost of the high performance switches currently being used in these systems sometimes can go up to million dollar range, so a low cost high performance switch can be an alternative. The are of low-noise, low-power circuits is another feasible area for high performance and ultra linear MEMS devices. The high quality factor inductors and varactors are also required for these circuits and this is quiet possible with MEMS technology. Varactors with a Q of 60-100 [21] are easy to obtain with capacitance values in the order of picoFarads. The third possible area is the portable wireless systems. In a three-band wireless system, there are several elements which can be replaced with tunable MEMS components such as filters, antennas, oscillators, matching networks, and switches. Of course, this is true for

MEMS components with reliability problems solved for commercial applications. Finally, phased-array systems area is an important application area of the RF MEMS. The use of low loss and tunable MEMS phase shifters can reduce the system complexity noticeably since several phase shifters and switches are required for these systems. These elements can reduce the power loss up to 6-8dB (in W-band) per phase shifter element which is a very important amount. The power consumption of the system can also be reduced significantly as the MEMS elements do not dissipate DC power.

Considering the wide range of applications areas, variety of the devices, and the performance values presented in the literature, RF MEMS devices seem to have major roles in the tomorrow's wireless systems.

1.2 Previous Work on Adjustable Impedance Matchers

Although different tunable components for microwave and millimeter-wave systems are present in the literature, there are not many tunable impedance transformers. The first adjustable impedance matching network example is presented by [1]. The idea behind the working principle is placing fixed capacitors which are switched by transistors on a transmission line. When one of the capacitors is switched, this means that it is virtually shifted over the transmission line. The device is monolithic and produced using HEMT technology.

Another example is reported by Sinky and Westgate [3]. They used a variable transmission line which is implemented using variable lumped elements. Since the lumped element model of a transmission line requires inductors other than capacitors, they used variable capacitors placed between two J-inverters to obtain a variable inductive behavior. With this method, they implemented all elements of a lumped element transmission line with variable values. They report

a transformation range of 4-392Ω with an insertion loss of 0.6-0.9dB in a tunable bandwidth about 15%.

An application of tunable impedance tuners to on-wafer measurements is presented by McIntosh et al [2]. They proposed an impedance tuner which is implemented by loading a transmission line with pHEMT transistors. The device was designed to reduce the mismatch losses between the device under test and the probes.

Other than the adjustable impedance matchers fabricated using FETs, there are some examples which are fabricated using the MEMS technology. The first example is presented by Chiao et al. [53]. It has the same working principle with the mechanical waveguide end short tuners. The structure is implemented over a planar transmission line and a movable short circuit is placed over it. By mechanical movement of the short circuit, the length of the short circuited transmission line can be adjusted. The structure has a very complicated processing phase.

The three types of devices were reported by Kim et al. [54]. The first device was an analog device composed of a MEMS variable capacitor connected parallel to a point on each stub of a double stub tuner, and an inductor implemented by a transmission line. Since the tuning range of the variable capacitors is limited, they used an LC resonance circuit to have high change of impedance. This is because the impedance changes very rapidly near the resonance. To have a frequency-variable device, they also proposed a second analog design which employs resonant cells with J-inverters. They used tunable capacitors as tunable inductors by means of J-inverters to move the resonance frequency of the device. The third type of device they reported was a digital type impedance tuner. This structure, again, used the double stub matching, but they

placed tunable MEMS capacitors with on and off state. The electrical length of the stubs change when one of the capacitors one each stub is actuated.

The last example of adjustable MEMS impedance tuners is reported by Papapolymerou et al [55]. They again used the variable capacitance at the end of each stub connected in series with a fixed capacitance, and changed the electrical length of the stub by tuning the capacitors. They also used a set of different initial state capacitances, each forming 1-bit, and selecting the bits by MEMS switches, different zones on the Smith chart can be matched in a digital manner.

1.3 The Impedance Matching Network Developed in This Thesis

The 3-D view and schematic of the impedance matching network developed in this thesis can be seen in Figure 1.1 and Figure 1.2 respectively. The device uses the basic triple matching theory. The variability of the device comes from its variable length stubs. The stubs of the device are implemented using coplanar waveguides (CPW) over which MEMS bridges equally spaced. The MEMS bridges are actually MEMS switches and to obtain a stub with a predefined length, corresponding MEMS switch to that length is actuated, forming a capacitive termination to ground. By this way, variable length stubs are obtained.

The MEMS variable impedance matching network is designed to transform any given impedance on the Smith chart to any other required impedance value. Other than variability, the device offers all the other advantages coming with MEMS technology such as low loss, small size and weight, and high linearity.

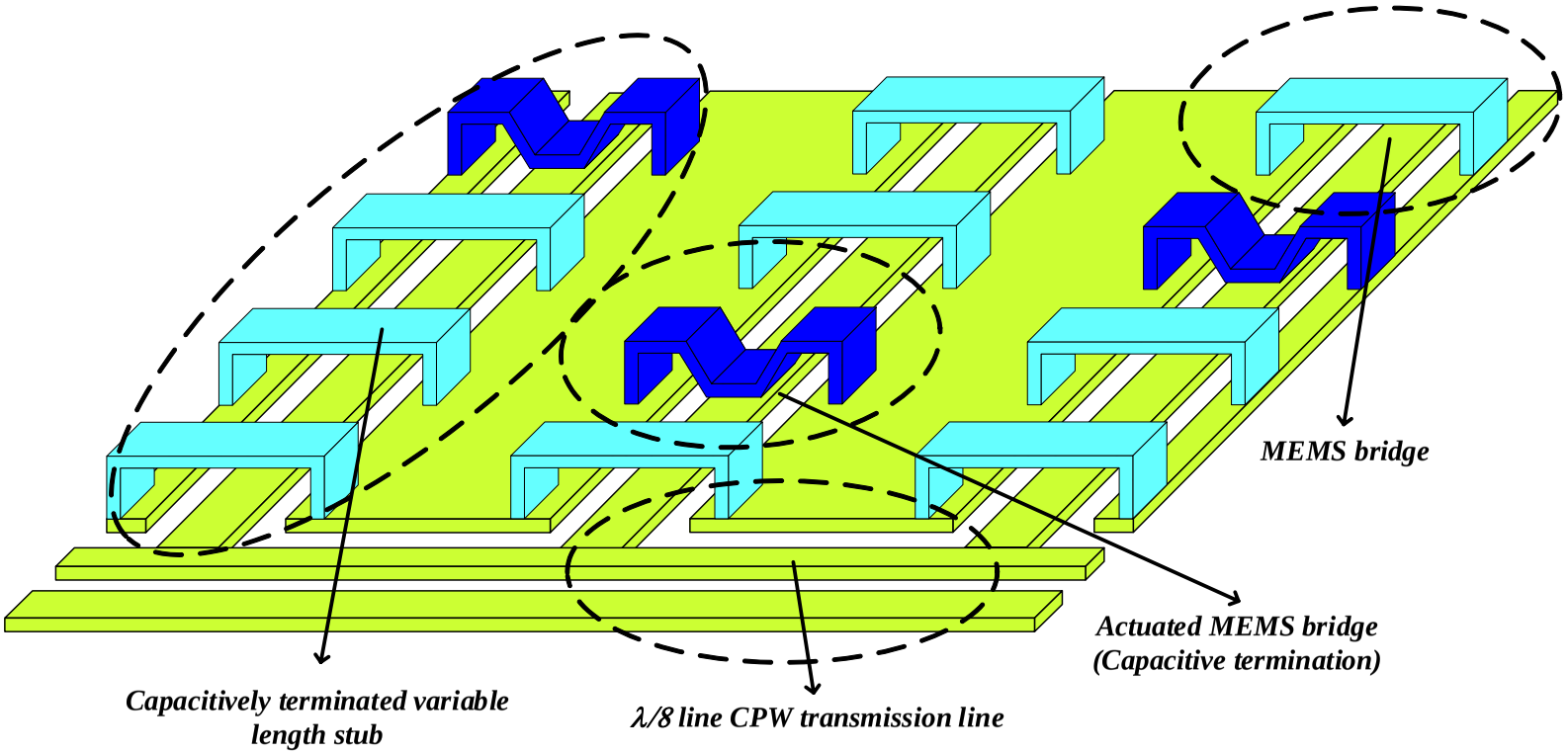

Figure 1.1 3D view of the MEMS variable impedance matching network.

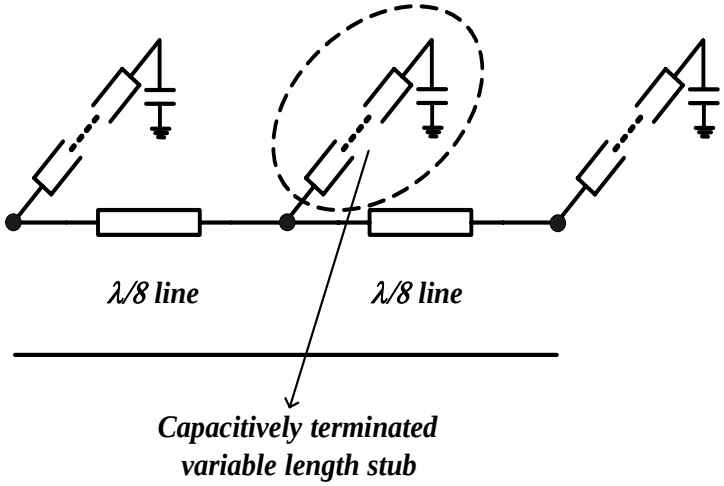

Figure 1.2 The schematic of the variable impedance matching network.

1.4 Research Objectives and Organization of the Thesis

The basic goal of this thesis is to design and fabricate a novel adjustable impedance matching network using RF MEMS technology at the microelectronics facilities of Middle East Technical University. The specific objectives can be summarized as follows:

- Design and fabrication of a shunt capacitive MEMS switch which will be used as a part of MEMS variable stub. The switch should be designed to have a very low insertion loss and high isolation since many of these switches will be cascaded in the final design. It should also be fabricated with high yield and uniformity since a huge number (120) of switches is used in the final impedance matcher design.
- Modeling, design, and fabrication of a variable length stub which will be implemented with MEMS technology. The MEMS switches should be placed over coplanar waveguide (CPW) stub with small electrical length spacing. In this case, the variability of the stub length can be pseudo-continuous with the actuation of each switch at almost every electrical length required. The CPW of the stub should be low loss because it has an

essential electrical length. A new model of the capacitively loaded MEMS lines that is composed of distributed and lumped elements should be developed so that it can be used for the final simulation of the adjustable impedance matcher and for further designs where using EM models are not feasible.

- Modeling, design, and fabrication of MEMS adjustable triple stub impedance matching network. The fabricated device should be able to transform any given impedance value to any other desired impedance value on the Smith chart. The device should have very low insertion loss. The fabrication of the device should be repeatable, have high yield and uniformity.
- The optimization of the domestic process for the fabrication of RF MEMS devices at microelectronics facilities of METU.

The study on RF MEMS technologies at METU was first started on 2000, and the first results were obtained and published in 2002 [56]-[58]. A master thesis was also done containing the details of design and fabrication of RF MEMS switches and phase shifters [59]. This thesis contains the results of accomplishments of METU RF MEMS group up to date.

The thesis is composed of six chapters. After this introduction chapter, chapter 2 explains the theoretical background of stub matching, coplanar waveguides, MEMS switches, and MEMS distributed capacitively loaded lines.

Chapter 3 defines the design criteria applied during the design of MEMS switch, MEMS variable length stub, and MEMS variable impedance matching network. It also describes the new model which is used to characterize the variable length stub and the adjustable impedance matching network. The comparison of electromagnetic (EM) simulations and modeled results are argued as well.

Chapter 4 gives the details of procedures followed throughout the fabrication. The material selected for each layer and the basis of selecting those material are explained. A whole flow of the RF MEMS process is given at the end of the chapter.

Chapter 5 presents the measurement results for the MEMS adjustable impedance matching network. The measurement results are compared with the modeled results, and the possible reasons for the discrepancies are discussed. The setup used for RF measurements are also introduced.

Chapter 6 summarizes the results of this study and suggests the areas for further research.

CHAPTER II

THEORY OF IMPEDANCE MATCHER AND ITS MEMS IMPLEMENTATION

2.1 Stub Matching

A general problem in a microwave system is to carry information or power from a generator to a load by means of a transmission line or a waveguide. In this case, it is preferable to match the generator and the load to transmission line separately. Another method of matching is the matching of the impedance seen at the input port to the source impedance and the matching of the impedance seen at the output port to the load impedance. This increases the power transferred to the load from the source. Also the mismatch at the load-transmission line or waveguide connection decreases the strength of the line upon breakdown. So, the matching problem of the system reduces to two separate matching to a transmission line or a waveguide. A well-known solution to this problem is the so-called *stub matching* where open or short circuited transmission lines are used. The single, double, and triple-stub matching techniques are explained next.

2.1.1 Single-Stub Matching

The idea behind single-stub matching is very simple. Talking in terms of normalized impedances, the idea is to transform the load to an admittance of $1 + jB$, and then cancel the imaginary part with connecting an open or short circuited stub which has an input impedance of $-jB$ at the distance where input impedance is equal to $Y_{in} = 1 + jB$. So, considering a real load admittance, G, the input impedance seen looking to the load side where the stub is connected is $Y_{in} = 1 + jB - jB = 1$, which means matching. The idea can be visualized from Figure 2.1 below.

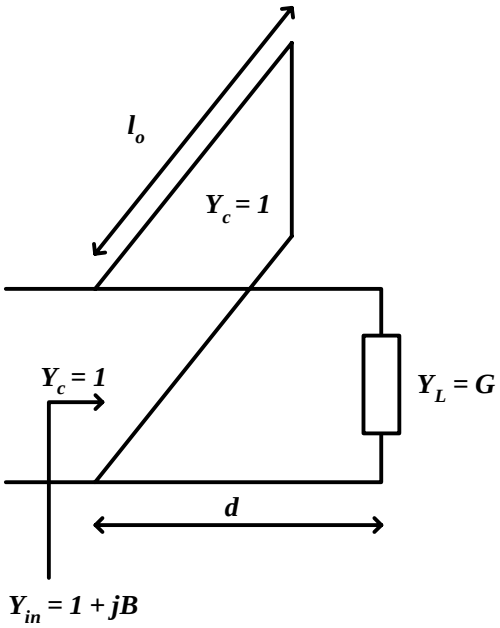

Figure 2.1 Single-stub matching.

To have a complete design, values of l_o and d must be known. These can be found using the basic transmission line theory, and are equal to:

$$d = \frac{\lambda}{4\pi}\cos^{-1}\left(\frac{G-1}{G+1}\right) \qquad \textbf{(2.1)}$$

$$l_o = \frac{\lambda}{2\pi}\tan^{-1}\left(\frac{\sqrt{G}}{1-G}\right) \qquad \textbf{(2.2)}$$

Note that the $d \pm \lambda/2$ are also solutions, but the minimum d should be selected to reduce the frequency instability. A more detailed analysis can be found in [60].

The single-stub matching can also be used for complex loads. Here, the only thing is to do the calculations not at the load point, but at the first minimum from load to the generator. At the minimum point, the input impedance seen towards the load is real; hence the normal solution can be followed. The required d is found by adding the distance found from the solution to the first minimum distance from the load.

2.1.2 Double-Stub Matching

A disadvantage of the single-stub matching is the requirement of a new stub position for every value of the load. To overcome this problem, the distance between the load and the generator is fixed, but in this case, two stubs need to be used, which means a "double-stub" matching.

The double-stub matching consists of two stubs, one at the load and one at the matching point, and a fixed distance between them, as can be seen in Figure 2.2. Here, the load does not have to be connected to at the first stub point, instead, it can be connected to any other point, again inserting a transmission line between

the first stub and the load point. This causes no problem considering a lossless system, because the transmission line only changes the value of the load to be matched at the second stub point. The only exceptional case is the case that the transferred load (the input impedance at the second stub point) drops to the "impossible matching" area, which will be explained later.

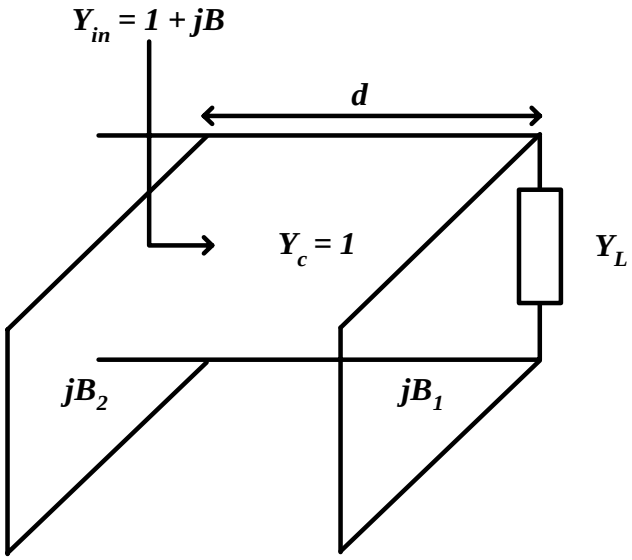

Figure 2.2 Schematic of double-stub matcher.

The solution procedure of double-stub matching becomes clear from the Smith chart in Figure 2.3. As in the single-stub matching case, the idea is to set the input impedance seen at the second stub point to $Y_{in} = 1 + jB$, so that after adding the second stub, it can be set to $Y_{in} = 1$ (from P_3 to P_4), which is the match case (center point). However, since the transmission line between the stubs have a fixed electrical length, the first stub should be arranged so that (from P_1 to P_2) after the transformation, the input impedance should fit onto the $G = 1$ circle (from P_2 to P_3).

Alternatively, there is one more solution to the problem which is to arrange the first stub so that after transforming with the transmission line in between, we arrive to point P_3' on the Smith chart. Of course, the value of the first stub, hence the value of the second stub changes, forming the second set of solution.

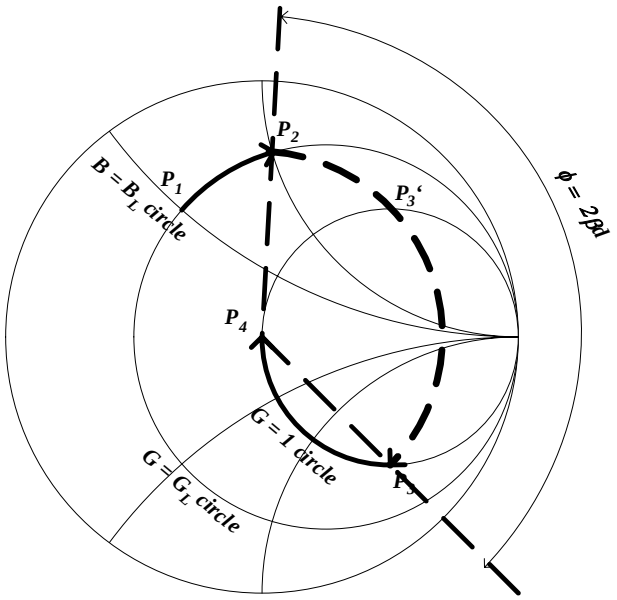

Figure 2.3 Double-stub matching steps shown on the Smith chart [60].

The analytical solution is obtained as follows: After the addition of the first stub, the impedance at the load point is $Y_L' = G_L + jB_L + jB_1$. Using the Telegrapher's equation for the transmission line in between, and equating to $Y_{in} = 1 + jB$, one obtains both stub values by equating real and imaginary parts. The values of the stubs are:

$$B_1 = -B_L + \frac{1 \pm \sqrt{(1+t^2)G_L - G_L^2 t^2}}{t} \qquad \textbf{(2.3)}$$

$$B_2 = \frac{\mp \sqrt{G_L(1+t^2) - G_L^2 t^2} - G_L}{G_L t} \qquad \textbf{(2.4)}$$

where $t = tan\ \beta d$. It should not be forgotten that to obtain matching, the negative signed value of the B_2 must be selected. It is also seen from the equations that there are two sets of solutions. A more detailed solution can be found in [60].

One limiting case for the double-stub matching is that, as mentioned before, it does not allow the matching of the all of the Smith chart. The area that double-stub technique allows is limited by the real part of the load admittance:

$$0 \le G_L \le \frac{1+t^2}{t^2} = \frac{1}{\sin^2 \beta d} \qquad \textbf{(2.5)}$$

This can also be observed from the equations above where the values of G_L, out of the limits given above, result with complex values of stub susceptances. Considering the Smith chart in Figure 2.4, this limitation is expected. Usual method of double stub matching on Smith chart starts with rotating $G = 1$ circle towards load, then, adding the first stub to move to the rotated $G = 1$ circle, and finally rotating the circle back to add the last stub. When this method is applied (considering $d = \lambda/8$), it is seen that for values greater than $G_L = 2$, there is no crossing of the rotated $G = 1$ circle and $G = G_L$ circles, hence no solution exists.

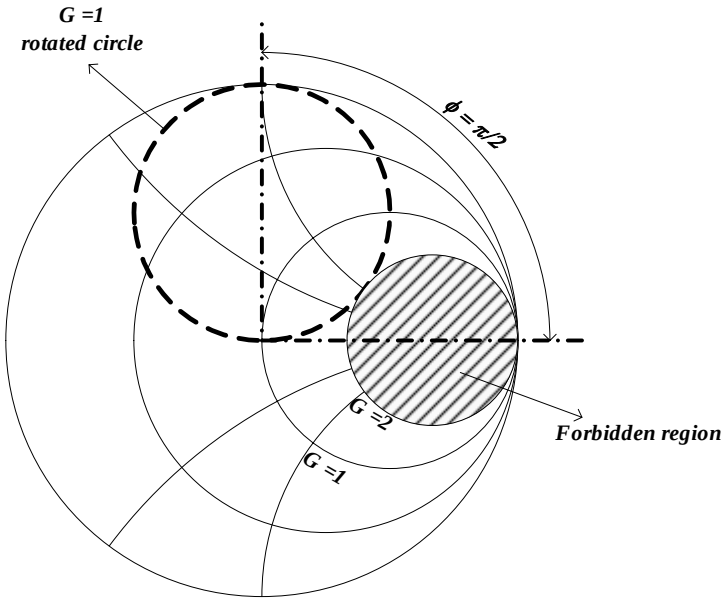

Figure 2.4 The limitations of the double-stub matching (for $d = \lambda/8$) [60].

Although theoretically it seems possible to solve this problem by selecting d near 0 or $\lambda/2$, so that $csc^2 \beta d$ becomes infinite, this is not true in practice. The limitation is the value of the stub susceptances that can be practically obtained. Moreover, the system becomes very sensitive to changes in the frequency with these values of d. Generally, $\lambda/8$ or $3\lambda/8$ spacing are preferred in practice.

2.1.3 Triple-Stub Matching

Not being able to match any given load impedance is an important limitation for double-stub matching. To overcome this problem, a third stub is employed with a second section of transmission line. The idea used here is to carry the load impedance, which falls into the "forbidden region" of double-stub matching, with a third stub and a transmission line segment, and after the conditions of the double-stub matching is satisfied, match the "new" load with the

conventional double-stub matching. The schematic of triple-stub matching can be seen in Figure 2.5.

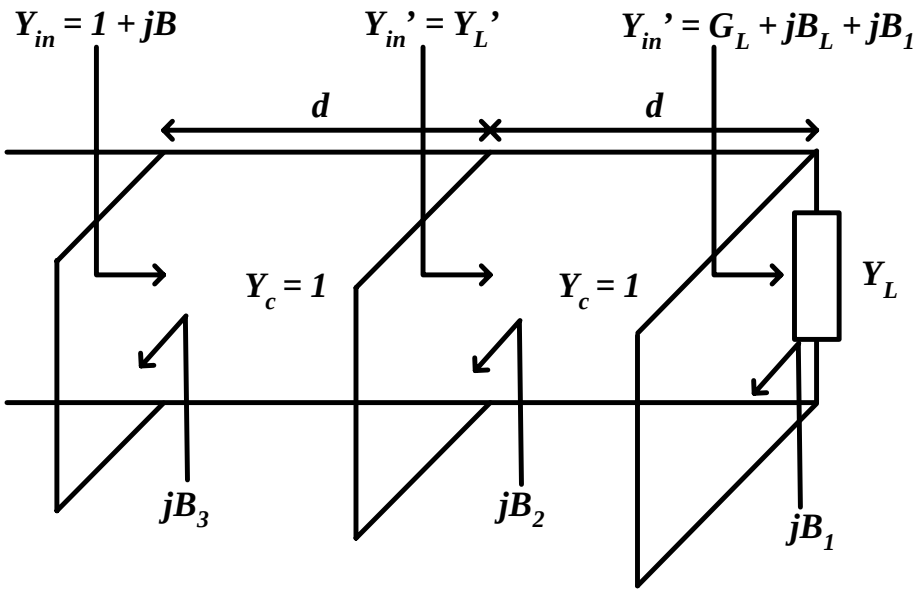

Figure 2.5 Schematic of the triple-stub matching.

Considering the situation in terms of equations:

$$Y_{in}^{''} = G_L + jB_L + jB_1 \qquad \textbf{(2.6)}$$

is the input impedance after the first stub is added. Then, it is transferred into:

$$Y_{in}^{'} = \frac{G_L + jB_L + jB_1 + jt}{1 + jt(G_L + jB_L + jB_1)} = Y_L^{'} \qquad \textbf{(2.7)}$$

by Telegrapher's equation, where $t = tan\beta d$. This is the "new" impedance to be matched by the remaining two stubs. Of course, here, we must have the condition:

$$G_L^{'} < \csc^2 \beta d \qquad \textbf{(2.8)}$$

The problem can be visualized again using the Smith chart. Using the same idea in the double-stub matching problem, the forbidden region is rotated towards load by $2\beta d$, and the amount of the susceptances required to carry the load admittance out of the forbidden region is found. In Figure 2.6 below, if d is equal to $\lambda/8$, the load admittance would be in the forbidden region after transferred by the first transmission line if no susceptance were added at the position of the first stub. However, adding a susceptance of an amount that moves the Y_L point beyond P_1 (for example P_1') or P_2 (for example P_2') will guarantee that the load point remains out of forbidden region at the position of second stub.

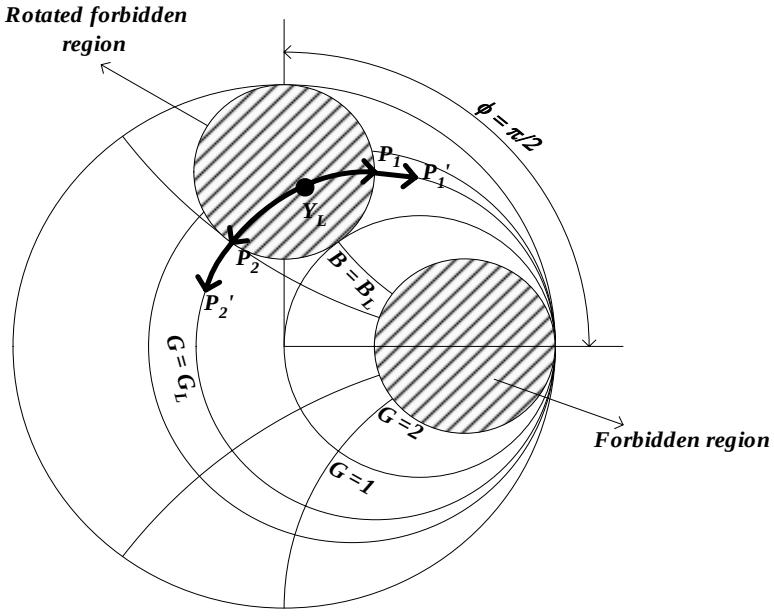

Figure 2.6 The use of third stub to guarantee the matching for $d = \lambda/8$ [60].

The limitations for the susceptances of the first stub can be stated as follows:

$$B_1 < 1 - B_L - \sqrt{G_L - G_L^2} \qquad \text{or} \qquad B_1 > 1 - B_L + \sqrt{G_L - G_L^2} \qquad \textbf{(2.9)}$$

Here, the solution is valid for $G_L < 1$, because for $G_L > 1$, Y_L' automatically stays out of the forbidden region.

2.2 Coplanar Waveguides

Coplanar waveguides (CPW) were first proposed by Wen in 1969 [61]. The structure consists of three conductors, one signal and two grounds, and all lying on the same side of the dielectric substrate; hence, the term "coplanar" arises. Since its first proposal, CPWs were widely accepted and used in both MICs and MMICs. One of the fundamental advantages that CPWs have brought is that they omit the use of vias to make a connection to ground. This reduces the parasitics inserted by the vias, and makes the connection of any series or parallel components easier. CPWs have comparable performance characteristics with microstrip lines. Moreover, the characteristic impedance of the CPW depends only on the dimension ratios, so the structures can be minimized theoretically without limit. The practical limitation is the increasing losses as the field is confined in a smaller area. Another advantage is the reduced crosstalk, since ground planes exist between each two signal lines. The next section explains the conductor backed coplanar waveguide (CBCPW) which is used in the structures of this thesis.

2.2.1 Conductor-Backed Coplanar Waveguides (CBCPW): Basic expressions

The first CPW proposed had an infinitely thick dielectric and infinitely wide ground planes as seen Figure 2.7. However, considering the practical cases, a finite dielectric thickness was used. Moreover, a second metal layer on the backside of the wafer can be coated, forming a CBCPW. With this addition to conventional CPW, the mechanical strength of the thin and fragile substrates and the power carrying capability of the structure are increased. This structure is also advantageous for circuits containing CPW-microstrip transitions.

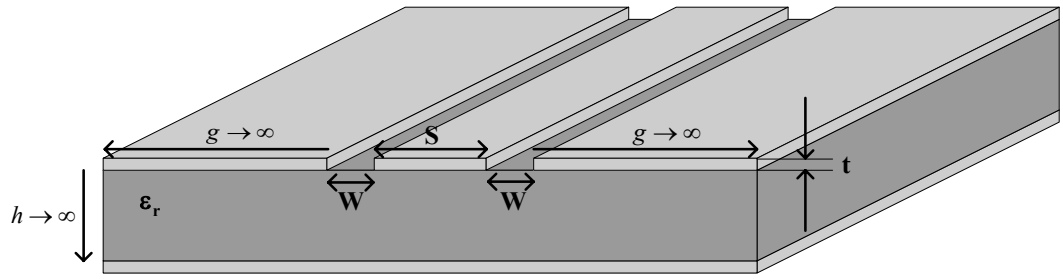

Figure 2.7 Coplanar waveguide structure.

The analysis of the CPWs is based on the quasi-static approach using conformal mapping techniques [62]-[64]. Fullwave analysis is also carried out with many researchers using different methods [65]. The first approach gives one analytical expressions for a faster design. The important parameters for a CBCPW are the characteristic impedance and the effective permittitvity, which are:

$$\varepsilon_{eff} = 1 + q(\varepsilon_r - 1) \qquad \textbf{(2.10)}$$

$$Z_0 = \frac{60\pi}{\sqrt{\varepsilon_{eff}}} \frac{1}{K(k_1)/K'(k_1) + K(k_2)/K'(k_2)} \qquad \textbf{(2.11)}$$

where *K(k) / K'(k)* are the elliptic integrals of first kind and given in [68] as:

$$\frac{K(k)}{K'(k)} = \frac{\pi}{\ln\left[2(1+\sqrt{k'})/(1-\sqrt{k'})\right]} \qquad for\ 0 \le k \le 0.707 \qquad \textbf{(2.12)}$$

$$\frac{K(k)}{K'(k)} = \frac{1}{\pi}\ln\left[2(1+\sqrt{k})/(1-\sqrt{k})\right] \qquad for\ 0.707 \le k \le 1 \qquad \textbf{(2.13)}$$

$$k' = \sqrt{1-k^2} \qquad \textbf{(2.14)}$$

The *k* values for the Z_0 expression *q* in ε_{eff} expression are:

$$k_1 = \frac{S}{S+2W} \qquad k_2 = \frac{\tanh(\pi S/h)}{\tanh(\pi(S+2W)/h)} \qquad \textbf{(2.15)}$$

$$q = \frac{K(k_2)/K'(k_2)}{K(k_1)/K'(k_1) + K(k_2)/K'(k_2)} \qquad \textbf{(2.16)}$$

2.2.2 Dispersion and Effects of Metallization Thickness

The dispersive characteristic of the CPW increases with increasing frequency. The affect of the dispersion may be overlooked from the lower end of

the microwave band to the lower end of the millimeter wave band, but should be considered from that point forward for an accurate design. The frequency dispersion can be observed in the characteristic impedance and especially in the effective permittivity ε_{eff}. There are many result obtained using curve fitting techniques from results of numerical solutions. The criticization of the dispersion effects is beyond the topic of this thesis, but an analytical expression can be found in [66].

The finite thickness of the signal and ground planes rather than infinitesimally thin metals has some affects on the characteristics of the CPW. The increasing thickness of the metallization increases the field concentration in the slots between the signal and the ground lines, increasing the per unit length capacitance, and hence decreasing the effective permittivity and characteristic impedance. Analytical formulas obtained from numerical results can be found in the literature [65].

2.2.3 Losses in CPW

One of the major loss mechanisms in CPWs is the dielectric loss. The closed analytical formulation of the dielectric losses are given in [65] as:

$$\alpha_d = 2.73 \frac{\varepsilon_r}{\sqrt{\varepsilon_{eff}}} \frac{\varepsilon_{eff} - 1}{\varepsilon_r - 1} \frac{\tan\delta}{\lambda_o} \text{ dB / unit length} \qquad \textbf{(2.17)}$$

where λ_o is the free-space wavelength, and $tan\delta$ is the loss tangent of the dielectric.

Another dominant loss mechanism is due to the finite conductivity of the metallization. An expression for the conductor losses in CPW from [65] is:

$$\alpha_c^{cw} = 4.88\times10^{-4} R_s \varepsilon_{eff} Zo \frac{P'}{\pi W}\left(1+\frac{S}{W}\right)\left\{\frac{1+1.25t/\pi S+(1.25/\pi)\ln(4\pi S/t)}{[2+S/W-(1.25t/\pi W)(1+\ln(4\pi S/t))]^2}\right\}$$

(2.18)

where

$$P' = \left[\frac{K(k_1)}{K'(k_1)}\right]^2 P \qquad \text{and} \qquad R_s = \sqrt{\frac{f\pi\mu_0}{\sigma}} \qquad \textbf{(2.19)}$$

$$P = \frac{k_1}{\left(1-\sqrt{1-k_1^{\,2}}\right)\left(1-k_1^{\,2}\right)^{3/4}} \qquad \textit{for } 0 \le k \le 0.707$$

$$P = \frac{1}{(1-k_1)\sqrt{k_1}}\left(\frac{K'(k_1)}{K(k_1)}\right)^2 \qquad \textit{for } 0.707 \le k \le 1 \qquad \textbf{(2.20)}$$

σ is the conductivity, f is the frequency, Z_o is the characteristic impedance of the line, and *S, W*, and *t* are dimensions given in Figure 2.7.

In addition to the dielectric and conductor losses, surfaces waves and radiation are the other loss mechanisms in CPW. Furthermore, parallel-plate waveguide mode occurs in a CBCPW. The reason of occurrence of this mode is that the dominant mode of the CPW travels faster than the parasitic parallel-plate mode, which is always the case for a CPW [67]. The radiation into the substrate is

also the result of the phase velocity difference, and causes losses [65]. Some numerical results can also be found in [65].

2.3 MEMS Shunt Capacitive Switch

MEMS switch is the very basic element underlying all of the RF MEMS structures. First RF MEMS switch was developed in 1991 by Larson et al. [4], but the structure was not mature. Although the device was not very mature, the performance of the device attracted interest of many research groups. Then, in 1996, two very successful devices, a high performance DC contact switch [5] and a high performance capacitive switch [6] were produced, starting the RF MEMS era. Many different switch structures were designed and present since then.

As mentioned before, RF MEMS switch is the key element for most of the RF MEMS structures. A good view of working principals of an RF MEMS switch opens the door to the RF MEMS world. So, understanding the electrical and mechanical characteristics of the MEMS switch is of crucial importance to have successful RF MEMS designs as well as the impedance matcher designed in this thesis. The MEMS switch structure to be used in the work of this thesis is a shunt, capacitive switch which can be seen in Figure 2.8. The next sections describe the theory behind the structure.

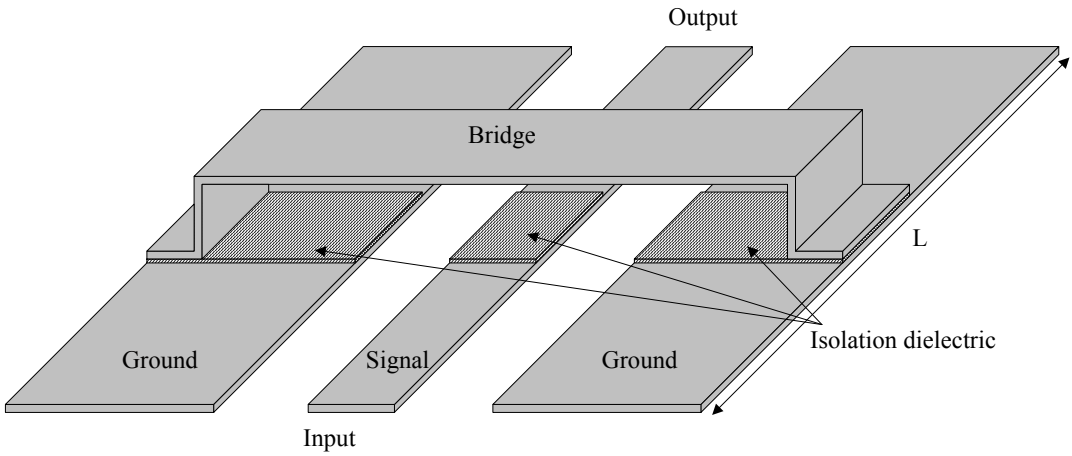

Figure 2.8 Shunt, capacitive, RF MEMS switch [59].

2.3.1 Mechanical Properties

Different MEMS switches in the literature use different types of actuation mechanisms such as electrostatic, thermal, and magnetic actuation [21]. The electrostatic actuation is the most widely used one, and also used in this thesis. So in this section, the electrostatic actuation principles and the related parameters such as spring constant, pull-down and hold-down voltages, and switching time will be explained for the shunt, capacitive MEMS switch.

2.3.1.1 Spring constant

Mechanically, the MEMS bridge is a fixed-fixed beam that is attached to the grounds of the CPW by the anchors. The spring constant of the structure is directly used in the pull-down voltage and switching time calculations, so it is important to understand from what the spring constant is affected.

The spring constant is composed of two components, one due to the stiffness of the material, and one due to the biaxial stress within the beam because

of the fabrication. The first component of the spring constant is dependent on how the force is applied to the structure. There are three common cases for applying the force in MEMS structures: evenly distributed on the entire beam, evenly distributed over a portion of the beam around the center, and evenly distributed near the ends of the beam. The first case can be seen in Figure 2.9 which is the structure used in this thesis. So, the formulas will be given for the first case only and for further details, [21] can be referred.

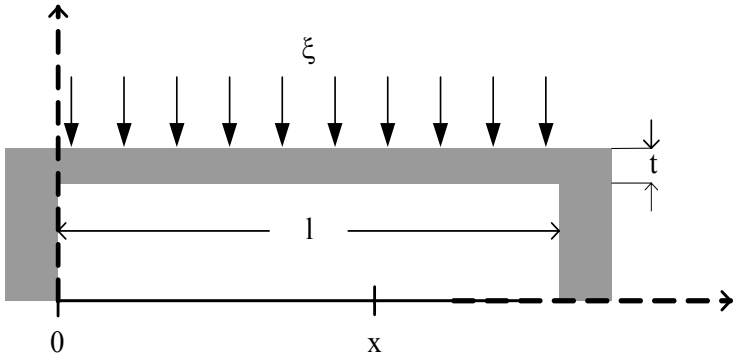

Figure 2.9 The diagram of a fixed-fixed beam with force applied uniformly over the entire beam.

The first component of the spring constant is given by:

$$k' = 32Ew\left(\frac{t}{l}\right)^3 \qquad \textbf{(2.21)}$$

where E is the Young's modulus, w is the width of the beam, t is the thickness, and l is the length. The second component which is due to the tensile residual stress is given by:

$$k'' = 8\sigma(1-\nu)w\left(\frac{t}{l}\right) \qquad \textbf{(2.22)}$$

where σ is the residual stress, ν is the Poisson's ratio. So, the total spring constant in a fixed-fixed beam with uniformly distributed load and in the case of tensile stress is the sum of the two components:

$$k_{total} = k' + k'' = 32Ew\left(\frac{t}{l}\right)^3 + 8\sigma(1-\nu)w\left(\frac{t}{l}\right) \qquad \textbf{(2.23)}$$

In the case of compressive stress, *k''* formulation is not valid. Some amount of residual compressive stress can be withstood in the structures because of the stiffness of the material. However, if the stress increases, the beam starts to buckle.

From the formulation, it can be seen that the material properties, such as Young's modulus and Poisson's ratio, production quality, and the geometry are very important for design phase. The material can be selected to have a high or low spring constant, but the second component of the spring constant may dominate due to the production conditions. The amount of residual stress should be decreased as much as possible to have a consistent design.

Of course, the fixed-fixed beam is not the only structure to implement a MEMS switch. There are many structures such as standard and simple cantilevers to low-*k* bridge designs with many different shapes to reduce or increase the spring constant. Some general structures can be found in [21].

2.3.1.2 Electrostatic Actuation

The actuation principle of the MEMS switch is very simple. It is just as in the case of parallel-plate capacitor where a voltage is applied between its metal plates. Since the charge accumulated on the metal plates cause a force on the other plate, the plates try to pull each other. This force is counteracted by a restoring force caused by the elasticity of the structure. If the voltage is increased, the plates get close to each other, the increasing charge on the plates increases the force and the equilibrium is held by an increase in the restoring force at some point between the plates. However, after the voltage value exceeds some value, the restoring force can not afford the electrostatic force. At this point, the system goes to an unstable state, and the bridge collapses upon the bottom electrode. This is the basic working principle of a MEMS switch in Figure 2.10.

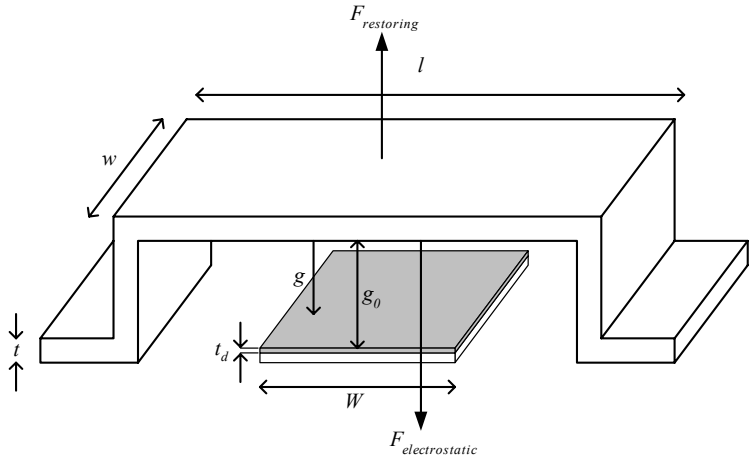

Figure 2.10 The dimensions and the forces on the fixed-fixed beam.

To find the analytical solution for the "pull-down" voltage and height, the electrostatic force, which is obtained by taking the derivative of the electrical

energy of capacitor between the plates, is equated to mechanical restoring force due to this stiffness of the beam. If the equation is solved for the applied voltage, it is obtained as:

$$V = \sqrt{\frac{2k}{\varepsilon_0 W w} g^2 (g_0 - g)} \qquad \textbf{(2.24)}$$

where g is the distance between the plates, k is the spring constant, ε_0 is the permittivity of the air, and the other are the dimensions given in Figure 2.10. If the derivative of (2.24) with respect to position is taken and equated to zero, the unstable point, i.e., the pull-down point is found as $2g_0/3$, and the corresponding pull-down voltage is:

$$V_p = V(2g_0/3) = \sqrt{\frac{8k}{27\varepsilon_0 W w} g_0^3} \qquad \textbf{(2.25)}$$

From (2.25), it can be seen that the pull-down voltage is strongly related with the gap between the plates. It is also related with the spring constant, hence the Young's modulus and the stress of the material.

Although V_p is the amount of voltage required to pull the switch down, it is more than the required voltage to "hold" the switch at the down state. This is because of the thin dielectric layer used for DC-isolation on the top of the bottom layer. Since the dielectric has an ε_r, the electrostatic force between the plates increases with the same proportion, so the required "hold-down" voltage is less than the pull-down voltage. Some formulations for the hold-down voltage can be found in [21].

Another mechanism that affects the actuation characteristics of a MEMS switch is the DC effect of the RF signal going through the switch. This is because the electrostatic force of the switch depends on the square of the voltage over it. Taking square of an RF signal brings a DC component which means that the RF signal over the switch also causes an electrostatic force between the plates. For the current technology, the required amount of power to "self-actuate" the switch may go up to the order of 10 Watts, which is not usually the case. However, the equivalent voltage can be compared with the hold-down voltage. To have an equivalent voltage of 5V, which can be comparable with the hold-down voltage for some capacitive MEMS switches, the required power may be 1.98 W at 10 GHz which is in the range of GSM standard. So, this effect must not be considered as a failure mechanism for a shunt, capacitive, MEMS switch. For a detailed analysis, please refer to [21].

2.3.1.3 Switching Time and Energy

The analyses carried out in the previous sections are static analysis. To be able to find the dynamic parameters such as switching time and energy, one should make a dynamic analysis of the mechanical structure of the MEMS switch. The system is modeled by a mass-spring-damper model and the differential equation to be solved to analyze the system is:

$$m\frac{d^2x}{dt^2} + b\frac{dx}{dt} + kx + k_s x^3 = F_e + F_c \qquad \textbf{(2.26)}$$

In (2.26), x is the displacement of the upper plate, m is the mass, b is the damping coefficient, k and k_s are the spring constants for stiffness of the material and stretching effect respectively. At the RHS of the equation, F_e is the electrostatic force and F_c is the force due to attractive van der Waals and repulsive

nuclear contact forces [21]. The mass and the spring constant of the system are clear to be understood, and the damping coefficient of the system comes from squeezing the gaseous between the plates. The other related parameters, the resonant frequency and the quality factor of the mechanical system, are:

$$\omega_o = \sqrt{\frac{k}{m}} \qquad \textbf{(2.27)}$$

$$Q = \frac{\sqrt{E\rho}t^2}{\mu\left(\frac{wl}{2}\right)^2} g_0^3 \qquad \textbf{(2.28)}$$

where μ is the viscosity of the gaseous in the environment ($\mu = 1.845 \times 10^{-5}$ kg/m·s for air), and ρ is the density of the bridge.

(2.26) can be solved with different voltage excitations to investigate pull-down, release, power handling, intermodulation, and source noise effects. A detailed work can be found in [21]. To find an approximation for the switching time of the system, the following formulation can be used [21]:

$$t_s \approx \frac{9V_p^2}{4QV_s^2\omega_0} \quad \text{and} \quad V_s >> V_p \qquad \textbf{(2.29)}$$

where V_p is the pull-down voltage, and V_s is the applied voltage. Other approximate formulas can be driven using (2.26). Here, the system is assumed damping limited and Q is assumed less than 0.5. For the release time, it is also possible to use the same equation with only the difference that electrostatic force does not exist.

The energy required to actuate a MEMS switch has different components. These are the mechanical spring energy, kinetic energy, electrical energy, and energy lost in damping. The required amount of energy is about 1-10 nJ [21].

2.3.2 Electromagnetic Model

The physical description of the MEMS switch was given in section 2.3.1, and can be seen in Figure 2.8 and Figure 2.10. Basically, the structure is composed of two metals layers and a dielectric layer between them to provide DC isolation. The first (upper) metal layer is a fixed-fixed beam (bridge), so it can be moved in a direction perpendicular to first metal layer. The first metal layer is used to form the transmission line on which the switch will be connected. In this case, the transmission line is chosen as a CPW whereas it might have been a microstrip.

Thinking RF vice, the structure is actually a variable capacitor between the bridge and the center conductor of the CPW. When no voltage is applied between the bridge and the first metal layer, the switch is in the ON (UP) state. In this state, the capacitance is very small, and ideally, switch is expected to have zero insertion loss. But actually, since there exists a real capacitance in the order of fF, there is a coupled path from the center conductor to ground, and thus there is a very small amount loss (-0.04 to -0.4 dB [21]). When the switch is electrostatically actuated, the bridge falls upon the first metal layer, forming the OFF (DOWN) state of the switch. The capacitance increases very much because of the decreasing height between the metal layers and the increasing permittivity of the material lying between the metal layers (since the bridge touches to dielectric layer, no air region remains between the metal layers). The increasing capacitance decreases the impedance between the signal and the ground of the CPW, and ideally forms a short circuit. This means that the bridge acts as a

parallel, reflective switch. For a perfect switch, the isolation is expected to be infinite at DOWN state. But due to the capacitive coupling and the losses, the isolation decreases, and can be greater than -20 dB at 50 GHz [21], which is acceptable anyway. The shunt, capacitive, MEMS switch is suitable for high frequencies such as 5-50 GHz.

2.3.2.1 Circuit Model

The MEMS capacitive shunt switch can be modeled by two sections of transmission lines on both sides, and impedance composed of a capacitance, an inductance, and a resistance. The model can be seen in Figure 2.11. The variable capacitance stands for the capacitance between the bridge and the signal line of the CPW for up and down states. The resistance is used to model the losses coming from the bridge. The inductance is found by the model fitting techniques and computed at the down state.

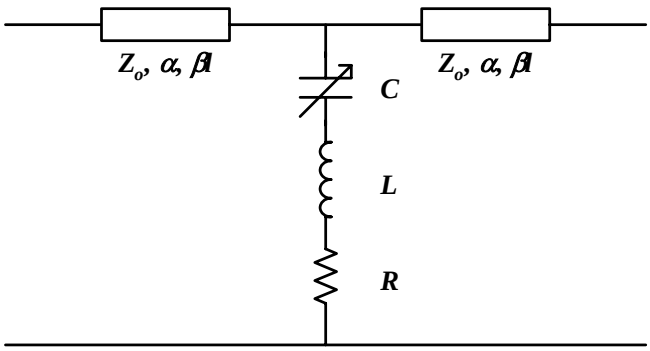

Figure 2.11 The equivalent circuit for the MEMS shunt switches [21].

The impedance of the bridge is given by (2.30) and the RF resonant frequency is given by (2.31).

$$Z_B = R + j\omega L + \frac{1}{j\omega C} \quad \textbf{(2.30)}$$

$$f_o = \frac{1}{2\pi\sqrt{LC}} \quad \textbf{(2.31)}$$

The bridge impedance can be modeled with only a capacitance for frequencies much less than f_o, so the inductance is not effective. Since the up-state capacitance, C_u, is in the order of fF, the operation frequencies are much below the resonant frequency for the up-state. This means that the inductor is not effective in the up-state. However, for the down-state, the down-state capacitance, C_d, becomes very large, pulling the resonant frequency in the operation band. So, for the down-state, the inductance can be used to increase the isolation to very high values at the desired frequency by moving the resonant point.

The capacitance values both at up and down states are very important. The ratio of capacitances can be used as a figure of merit, since it directly affects the isolation. The up-state capacitance is expected to be found by the parallel plate formulation which is:

$$C_{pp} = \frac{\varepsilon_o w W}{g + \frac{t_d}{\varepsilon_r}} \quad \textbf{(2.32)}$$

However, the up-state capacitance found by numerical solvers is about 20-60% more than the values calculated using (2.32) [21]. This effect is due to fringe fields. The down-state capacitance can be found by using the parallel plate

formula and by neglecting the fringe fields. The formula for the down state is given by:

$$C_d = \frac{\varepsilon_o \varepsilon_r w W}{t_d} \qquad \textbf{(2.33)}$$

Since the capacitance ratio C_d/C_u is important, and C_u can not be changed much, the attempts are generally to increase C_d. The methods applied are to decrease t_d, to use high-permittivity materials as dielectric, and to reduce the surface roughness of the dielectric layer so that less spacing is left between the bridge and the dielectric layer. These will be again investigated in the design section.

2.3.2.2 S-Parameters

The S-parameter behavior of the shunt, capacitive MEMS switch is important to characterize the switch. Although, the model seems simple, it is not easy to extract the parameters. So at this point, it is useful to derive the S-parameters of the model given above.

The derivation of S-parameters is easy if the transmission lines at both sides have characteristic impedances which are equal to the reference impedance, 50Ω. This is the general case for most of the switches used in the literature. Although it is not the case of this thesis, the formulations and comments are given next. The reflection coefficient of the switch for this case is:

$$S_{11} = \frac{-j\omega C_u Z_o}{2 + j\omega C_u Z_o} \qquad \textbf{(2.34)}$$

The effects of L and R are neglected in this case. If $S_{11} < -10\ dB$ and $\omega C_u Z_o << 2$, which is the required situation for a successful switch design, the expression reduces to:

$$\left|S_{11}\right|^2 \cong \frac{\omega^2 C_u^2 Z_o^2}{4} \qquad \textbf{(2.35)}$$

One of the important parameters in down-state of the bridge is S_{21}. In the down-state for $f > f_o$, the inductance has an unavoidable effect on the S_{21} response. So, S_{21} shall be given considering the frequency range, which is:

$$S_{21} = \frac{1}{1 + j\omega C_d Z_o / 2} \cong \frac{2}{j\omega C_d Z_o} \qquad for\ f << f_o \qquad \textbf{(2.36)}$$

$$S_{21} = \frac{2R // Z_o}{R // Z_0 + Z_o} \cong \frac{2R}{Z_o} \qquad for\ f = f_o \qquad \textbf{(2.37)}$$

$$S_{21} = \frac{2j\omega L}{Z_o + 2j\omega L} \cong \frac{2j\omega L}{Z_o} \qquad for\ f >> f_o \qquad \textbf{(2.38)}$$

The assumption made for (2.36) is the same as assumption made for (2.34). The assumption made for (2.37) is $R << Z_o$, since R is in the order of 0.1-1Ω and Z_o is 50Ω. The assumption for (2.38) is that the impedance of the inductor becomes too small compared to Z_o which is expected for even f = 1000GHz and L in the order of pH. As can be seen from the above equations, it is possible to extract R of the bridge at resonant frequency and L of the bridge for $f >> f_o$.

If the characteristic impedances of the lines at both sides are different from 50Ω, then the formulations given above are not valid. The derivation of the port parameters for this case is a little more tedious. The easiest method to find the S-parameters of this case is to use the *ABCD* parameters of the two-port device. The *ABCD* matrix of the whole device is given as:

$$\begin{bmatrix} A & B \\ C & D \end{bmatrix} = \begin{bmatrix} \cos\beta l & jZ_o \sin\beta l \\ \frac{j}{Z_o}\sin\beta l & \cos\beta l \end{bmatrix} \begin{bmatrix} 1 & 0 \\ Y_s & 1 \end{bmatrix} \begin{bmatrix} \cos\beta l & jZ_o \sin\beta l \\ \frac{j}{Z_o}\sin\beta l & \cos\beta l \end{bmatrix} \quad \textbf{(2.39)}$$

where Y_s is the shunt admittance at the center of the switch. After the *ABCD* matrix is found, it is easy to obtain to the S-parameters. S_{11} and S_{21} are given for this case as:

$$S_{11} = \frac{A + \frac{B}{Z_o} - CZ_o - D}{A + \frac{B}{Z_o} + CZ_o + D} \quad \textbf{(2.40)}$$

$$S_{21} = \frac{2}{A + \frac{B}{Z_o} + CZ_o + D} \quad \textbf{(2.41)}$$

During the modeling of the devices in this thesis, both of the models given above may not be able to fit the simulated S-parameters considering the MEMS bridge with a single capacitor or shunt impedance. This may be due to the small electrical length between the MEMS bridges or the relatively high MEMS bridge height. For this purpose, another model is developed for the case of this thesis and a more detailed explanation will be made in the design chapter.

2.3.2.3 Loss

The power loss of the bridge can be found using the S-matrix parameters of a lossless system. Since the squares of the S_{11} and S_{21} should add up to one in a lossless system, the loss for the MEMS switch is:

$$Loss = 1 - |S_{11}|^2 - |S_{21}|^2 \qquad \textbf{(2.42)}$$

The loss comes from two components. First one is the loss due to the CPW and it can be computed using (2.18). The other component is due to the currents on the bridge. The loss due to the bridge is calculated via dividing the power loss on the bridge, which is $I_B^2 R$, by power incident on the bridge, which is $|V^+|^2/Z_o$. The loss when the switch is in the up-state is found as:

$$Loss_u = \omega^2 C_u^2 R Z_o \qquad \textbf{(2.43)}$$

for $S_{11} << -10dB$ and $Z_B << Z_o$ The loss for the down-state is given by:

$$Loss_d = 4R / Z_o \qquad \textbf{(2.44)}$$

for $S_{21} << -10dB$ and $Z_B >> Z_o$. Generally for a capacitive, shunt MEMS switch, the up-state loss is dominated by the loss of the transmission line, while the down-state loss is dominated by the loss due to R in Z_B.

2.4 Capacitively-Loaded Distributed Transmission Lines

Using distributed transmission lines is common solution to obtain wide-band structures. The idea beyond the distributed structures is to load the transmission line periodically with lumped elements. With these periodically added elements, the structure preserves its distributed behavior, but line characteristic properties change. The changes in the transmission line parameters are the results of the general behavior of periodically loaded structures, which are stopband-passband characteristics and the change in the phase velocity of the wave traveling in the structure [60]. The stopband-passband characteristics of the periodically loaded structures are used in filter implementations whereas its ability to support slow waves is used in traveling-wave tubes and phase shifters. Another advantage of the distributed structures is that the parasitics in the added lumped elements such as transistors is distributed over length. As a result of this, the effects of parasitics reduced significantly, and the band limitations coming from these parasitics are prevented extensively.

2.4.1 Analysis of Capacitively Loaded MEMS CPW

The periodic structures are composed of unit sections throughout the structure. So, to analyze the structure, one should first analyze the unit section. The unit section for the MEMS variable impedance matching network is a shunt susceptance, which is the loading capacitor made of a MEMS bridge, and two sections of transmission lines on both sides of the susceptance. The general unit section and cascade connected unit sections can be seen in Figure 2.12.

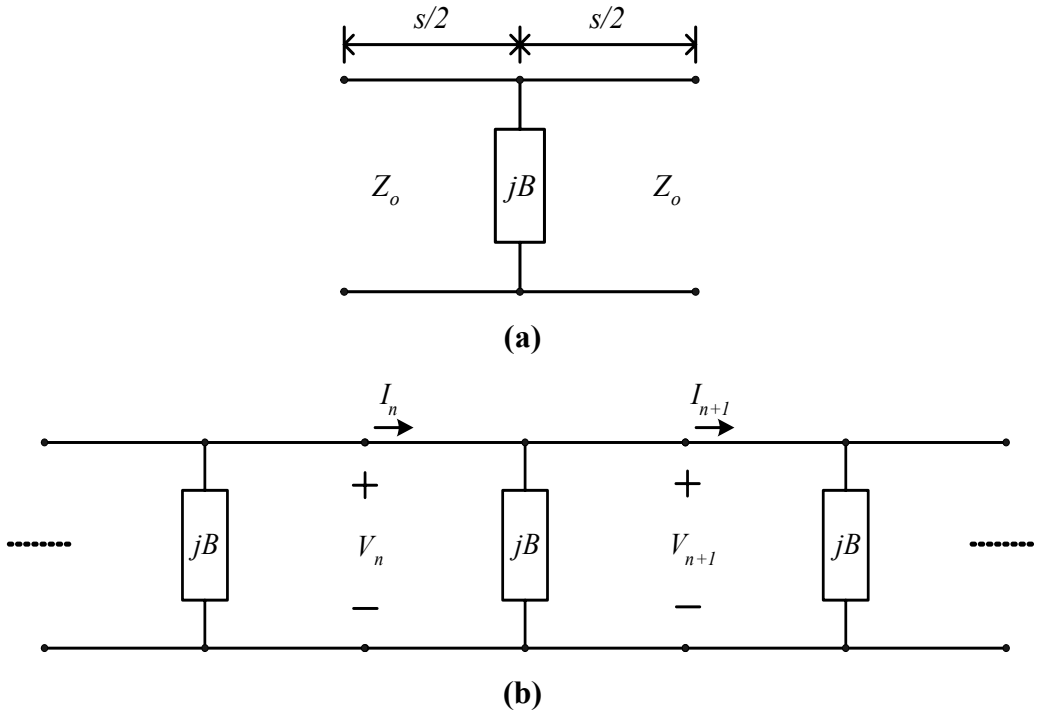

Figure 2.12 **(a)** The general unit section for a capacitively loaded line. **(b)** Cascade connection of unit sections.

The first step of the analysis is to find the *ABCD* parameters of the structure. The *ABCD* matrix for the unit section is the product of the *ABCD* matrices of the t-line sections and the susceptance *B*, relating the voltage and current of one section to the voltage and current of the next section, which is:

$$\begin{bmatrix} V_n \\ I_n \end{bmatrix} = \begin{bmatrix} \cos\frac{\theta}{2} & j\sin\frac{\theta}{2} \\ j\sin\frac{\theta}{2} & \cos\frac{\theta}{2} \end{bmatrix} \begin{bmatrix} 1 & 0 \\ jB & 1 \end{bmatrix} \begin{bmatrix} \cos\frac{\theta}{2} & j\sin\frac{\theta}{2} \\ j\sin\frac{\theta}{2} & \cos\frac{\theta}{2} \end{bmatrix} \begin{bmatrix} V_{n+1} \\ I_{n+1} \end{bmatrix} \qquad \textbf{(2.45)}$$

where θ is the electrical length corresponding to d. Also for the voltages and the currents in the structure the equation below must be valid:

$$V_{n+1} = e^{-\gamma d} V_n$$
$$I_{n+1} = e^{-\gamma d} I_n \qquad \textbf{(2.46)}$$

if it supports a propagating wave with propagation constant γ. Solving these two sets of equation simultaneously, and assuming a "low" frequency, one gets the propagation constant and the characteristic impedance of the loaded line as [60]:

$$\beta = \omega \sqrt{L_t \left(C_t + \frac{C_b}{s} \right)} \qquad \textbf{(2.47)}$$

$$Z = \sqrt{\frac{sL_t}{sC_t + C_b}} \qquad \textbf{(2.48)}$$

Here L_t and C_t are per unit length inductance and the capacitance of the unloaded transmission line, and C_b is the capacitance inserted by the MEMS bridge. The per unit length inductance and the capacitance of the unloaded transmission line are given in [69] by:

$$C_t = \sqrt{\frac{\varepsilon_{eff}}{cZ_o}} \quad \text{and} \quad L_t = Z_o^2 C_t \qquad (2.49)$$

The details of the above analysis and a wave analysis of the structure can be found in [60]. Waves propagating in periodic structures are also called Bloch

waves as an analogy to the electron waves propagating through a crystal lattice in a solid.

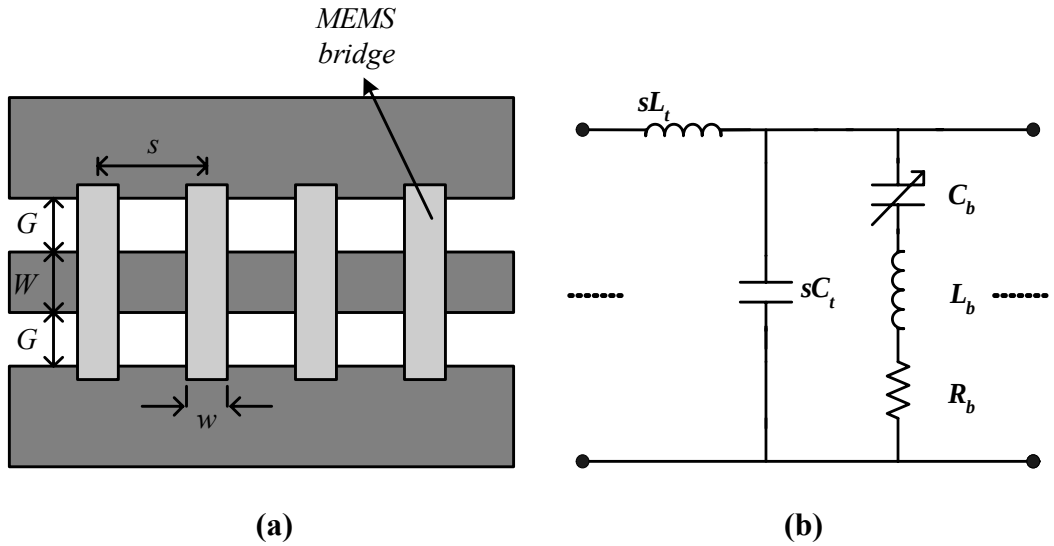

Figure 2.13 **(a)** MEMS capacitively loaded CPW line top view **(b)** its lumped element unit section [21].

The MEMS implementation and its lumped element model can be seen in Figure 2.13. Here, for this structure, it was reported in [70] that the structure is band limited with a frequency less than the resonant frequency of the unit section. At this frequency, the loaded impedance of the structure goes to zero which results no power transfer to the structure. This frequency is called the *Bragg* frequency of the structure. The "low" frequency definition is now clear in the above discussion and stands for the frequencies much less than the Bragg frequency. In this case, equation (2.48) should be modified including the effect of the Bragg frequency as follows [21]:

$$Z = \sqrt{\frac{sL_t}{sC_t + C_b}} \sqrt{1 - \left(\frac{\omega}{\omega_B}\right)^2} \quad \text{where} \quad \omega_B = \frac{2}{\sqrt{sL_t(sC_t + C_b)}} \qquad \textbf{(2.50)}$$

The above result could also be obtained using the Bloch wave analysis [60].

It was mentioned above that the capacitively loaded line is a slow-wave structure. For the sake of completeness, the time delay per unit section is given by [21] as:

$$\tau = \sqrt{sL_t(sC_t + C_b)} \left(1 + \frac{\omega^2}{6\omega_B^2} + \ldots\right) \qquad \textbf{(2.51)}$$

For frequencies much less than the Bragg frequency, the expression reduces to:

$$\tau = \sqrt{sL_t(sC_t + C_b)} = \frac{2}{\omega_B} = \frac{s}{v_p} = \frac{s}{c/\sqrt{\varepsilon_{eff}}} \qquad \textbf{(2.52)}$$

resulting with an expression for the effective dielectric constant of the loaded line:

$$\sqrt{\varepsilon_{eff}} = \frac{c\sqrt{sL_t(sC_t + C_b)}}{s} = \frac{2c}{s\omega_B} \qquad \textbf{(2.53)}$$

For the above analysis, the MEMS bridge is modeled as a shunt capacitance only, but it is not the case. It is reported in [21] the bridge inductance has a considerable effect on the Bragg frequency, so it shall be included in the calculations.

2.4.2 Loss of the Capacitively Loaded MEMS CPW

The loss of a transmission line is modeled with a resistance per unit length connected in parallel to the per unit length inductance and a conductance per unit length connected to the per unit length capacitance of the lumped element model. Here, the resistance stands for the conductor losses and the conductance stands for the dielectric losses. The attenuation constant is given by:

$$\alpha = \frac{R_t}{2Z} + \frac{G_t Z}{2} \qquad \textbf{(2.54)}$$

In our case, the unloaded CPW is loaded with capacitors, because of this, the current distribution on the line changes, changing the losses. The amount of change can be seen from (2.54). Since the line characteristic impedance decreases with the loading, the conductor losses increase and the dielectric losses decreases with the ratio of the unloaded to loaded impedance ratio. For the CPW built on low-loss substrates, the conductor losses dominate the dielectric losses, so it can be said that the overall loss coming from the line increases.

Additional to the increasing loss due to the change in the impedance, the MEMS bridge also adds to the loss due to the serial resistance, R_b, in the MEMS bridge model. The attenuation constant due to MEMS bridge losses is given in [70] as:

$$\alpha_b = \frac{R_b Z \omega^2 C_b^2}{2} \quad for \quad (\omega C_b R_b)^2 << 1 \qquad \textbf{(2.55)}$$

where Z is the characteristic impedance of the loaded line.

Although the conductive losses increase in the loaded CPWs, the radiation losses decrease in the structure. This can be explained as follows: the radiation losses occur due to greater phase velocity in the structure than the dielectric. But this is not the case for the loaded line, because periodic structures are slow-wave structures, so the phase velocity of the wave is less than the phase velocity of the wave in the dielectric. As a result, radiation loss does not occur. The only point of interest is to select suitable input and output port dimensions so that radiation loss is minimized at the ports.

CHAPTER III

DESIGN OF MEMS IMPEDANCE MATCHER

This chapter explains the details of the design of a MEMS impedance matcher. The design uses the idea of triple-stub matching, but the idea is greatly expanded by making an adjustable impedance matcher. Theoretically, the device can provide matching to any point of the entire Smith chart. The variability of the device comes from its adjustable stubs. The stubs are composed of CPW and periodically placed MEMS bridges upon the CPW which capacitively load the transmission line. Actually, each bridge is a shunt capacitive MEMS switch. When the MEMS switch at a position is closed, it creates a virtual short circuit to ground, reflecting the whole incident signal coming onto it, and forming a short-circuited stub with variable physical and electrical length.

Other than the adjustability property of the MEMS impedance matcher, it offers very low loss, near-zero power consumption, ultra high linearity, and very high isolation at switch points like the other RF MEMS devices. But to have successful design one should certainly pay attention to every step of design. A good design should consider the origins of the losses in the CPW, mechanical and electrical characteristics of a MEMS switch such as isolation, insertion loss, actuation voltage, and switching time. The discontinuities coming from the

junctions should be considered for the whole device to prevent radiation losses. And of course, the limitations and the material properties to be used in the implementation of the structure must be investigated deeply.

The above mentioned criteria will be examined part by part. The first part explains the details of CPW design for the structure implementation. Mechanical and electromagnetic design of the MEMS switches will be explained in the next subsection. The third subsection is devoted to the variable length MEMS stub design. And the last subsection gives the details of the whole structure.

3.1 CPW Design

The CPW lines used in the structure are conductor-backed structure which was explained in Section 2.2.1 in detail. The center frequency of the CPW is 10GHz which is the center frequency of the MEMS impedance matcher. The lines are designed to have characteristic impedances greater than 50Ω, because when the MEMS capacitive bridges are placed, the characteristic impedances will drop to 50Ω.

The CPW is built on Corning 7740 glass (Pyrex) with a 500μm thickness. It has a relative permittivity of 4.6 and a dielectric loss tangent of 0.005 at 1 MHz [71]. The metallization for the signal and ground lines are made of electroplated copper. Electroplated copper is preferred for the front-side because of its ease of thick coating and high conductivity. The backside coating is used to prevent the structure from unwanted coupling and increase the mechanical strength of the fragile glass substrate. It is also required for transition to microstrip devices on the same mask set. The backside coating is made of sputtered copper. The total slot width, $S+2W$, is selected to be 240μm for the stubs and it is selected as 160μm for

the unloaded lines. These widths are much less than the guided wavelength, which is about λ_g = 1.79 cm, preventing the CPW to support multimodes. These lengths are also required for the probe pitch spacing of the microwave probes during measurements. The ground planes of the structure are not infinite, but they are about two times the total slot width, *S+2W*, and this amount ground planes at both sides makes little changes from infinite ground plane width case [63]. The CBCPW structure with the dimensions can be seen in Figure 3.1.

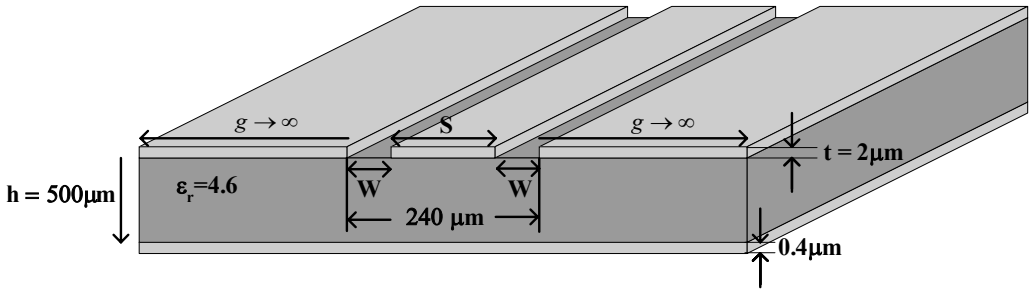

Figure 3.1 CBCPW structure with dimensions.

There are four different sets of dimensions of CPW for four different cases. Three of them are for the capacitively loaded line structures with different bridge spacings and one of them is the unloaded 50Ω line which is used for connecting the stubs. The center conductor, the slot widths, and the characteristic impedances for these four lines are given in Table 3.1.

The conductor, dielectric, and radiation losses per cm are calculated for four types of lines. The conductor losses are calculated using (2.18) and the formula given in [72]. The dielectric losses are calculated using (2.17). The radiation losses are calculated using the formula given in [73]-[74]. The losses are given in Table 3.2.

Table 3.1 The dimensions and the characteristic impedances of the CPWs used in the impedance matchers.

Name	W (μm)	S (μm)	Z_0 (Ω)
200μm unit section	74	83	89.97
260μm unit section	88	76	83.39
420μm unit section	116	62	72.49
Unloaded line	120	20	52.85

Table 3.2 Losses for the CPW lines. All are in dB/cm.

Name	α_c	α_c	α_d	α_{rad}
200μm unit section	0.285	0.318	0.006	0.0016
260μm unit section	0.282	0.333	0.006	0.0017
420μm unit section	0.293	0.395	0.006	0.0018
Unloaded 50Ω line	0.644	1.321	0.006	8.769×10^{-4}

In the formulas, the line thickness, t, is taken as 2μm. R_s in the conductor loss calculations is 0.028 and is calculated using σ = 5×10^7 S/m and at f = 10GHz. The dielectric loss tangent for the dielectric loss calculations is $tan\ \delta = 0.005$. Considering the attenuations calculated, an increase is observed in the conductor losses when the center conductor width is increased. This is expected since the total slot width is constant and resistive areas are increased with increasing the center conductor width. It is also reported in [21] that the second formula for the conductor losses underestimates the loss by a factor of 1.6 to 1.8. One final comment is that although present, the radiation losses are small, and can be neglected.

The designed lines were simulated using Ansoft HFSS electromagnetic simulator. The simulator program uses the FEM method for electromagnetic simulations. The material parameters and the dimension are taken as explained above. The dispersion of relative permittivity due to frequency is not included in the simulations. The simulation results can be seen in Figure 3.2 below.

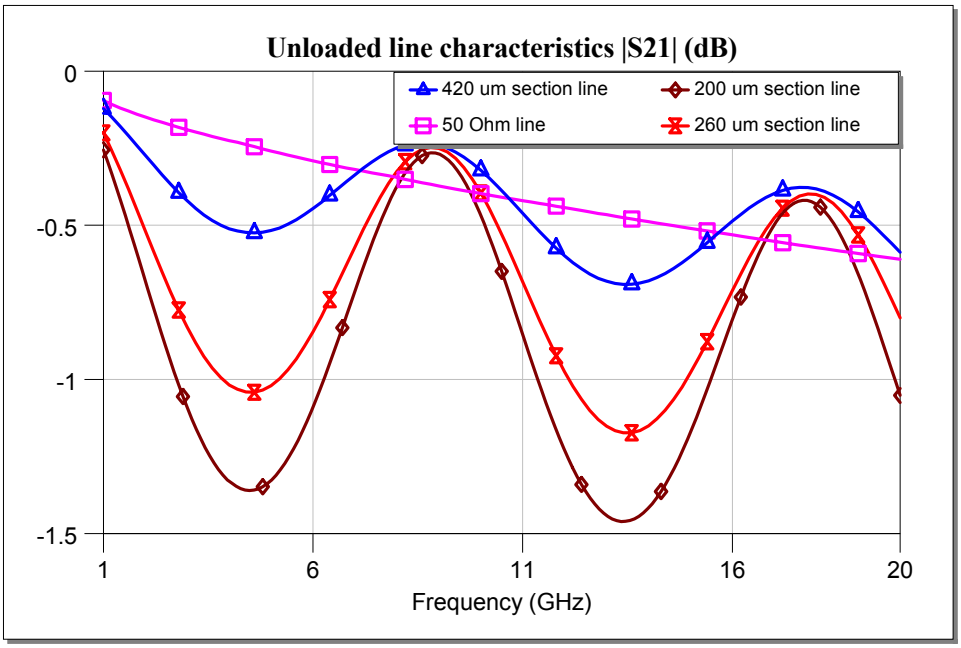

(a) Simulated $|S_{21}|$ for unloaded line.

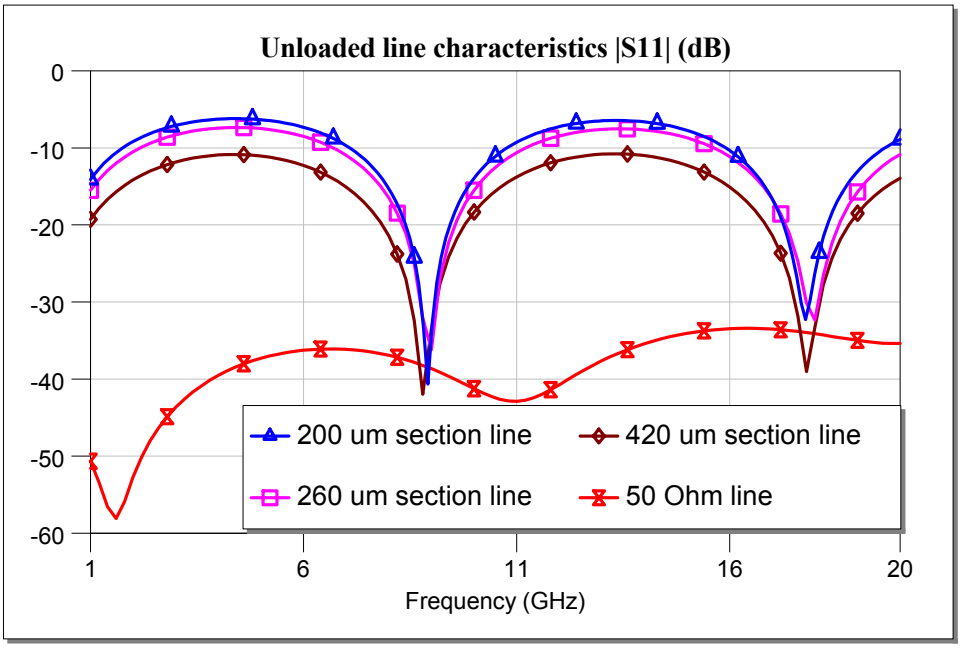

(b) Simulated $|S_{11}|$ for unloaded line.

Figure 3.2 (a)-(b) HFSS simulation results for the unloaded CPW designs.

One point that must be mentioned here is that the initial designs were made for a relative permittivity of 5.75 according the database of the simulator programs. However, the actual substrates obtained have a relative permittivity of 4.6. This is the reason of discrepancies in characteristic impedance values of the lines in Table 3.1.

3.2 Shunt, Capacitive MEMS Switch Design

As explained before, the variability of the MEMS impedance matcher comes from its variable length stubs. The stubs are actually cascade connected shunt, capacitive MEMS switches as unit sections. So in this case, the performance of a discrete MEMS switch determines the performance of the whole structure.

The design of a MEMS switch has two parts which are mechanical and electromagnetic design phases. The mechanical design of the switch determines the parameters such as spring constant, mechanical resonance frequency, quality factor, actuation voltage, switching time, and power consumption. The electromagnetic design phase determines parameters such as insertion loss, isolation, return loss, and bandwidth. But two phases of the design should be made synchronously, because most of the parameters are coupled to each other. For example, the bridge height of the MEMS switch strongly affects the actuation voltage whereas it is also the main parameter of the isolation and return loss. This is why these structures are called electromechanical systems.

It should not be forgotten that the MEMS switches in this thesis work are not designed to maximize any specific parameter. This aim is parallel with the aim of this thesis which is to demonstrate the idea of MEMS variable impedance matcher.

The first part of this section explains the mechanical design of the MEMS switch while the second part examines the electromagnetic design.

3.2.1 Mechanical Design Phase

The mechanical structure of the MEMS switch in this work is a clamped-clamped beam. The structure can be seen in Figure 3.3. It is composed of two metal layers, and an isolation layer to prevent DC shorting. The base metal layer is made of electroplated copper and has a thickness of 2 μm. The total length of the structure is 640 μm, and the spacing between two ground planes of CPW on both sides is 240 μm. These two lengths do not change for any switches. But the center conductor width of the CPW, *W,* change for the three types of switches.

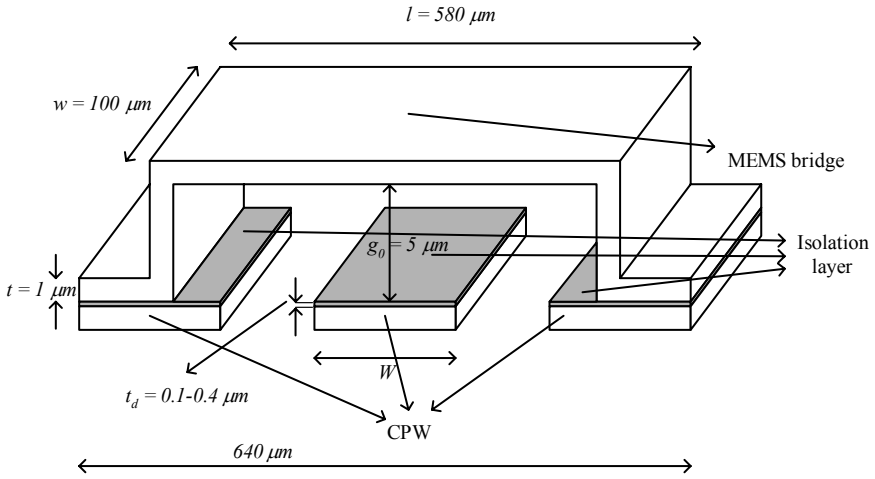

Figure 3.3 Mechanical structure of the shunt, capacitive MEMS switch.

The mechanical behavior of the switch is mostly related with the bridge, which is the second metal layer. This layer is made of electroplated nickel. The bridge dimensions for the switches in this thesis are the same and can be seen in the figure above. The spring constant for these dimension are calculated using (2.21) and (2.22). During the calculation of the first component, the Young's modulus is taken as E = 200 GPa [75]. The spring constant due to this component

is found as k' = 3.28 N/m. The second component of the spring constant is found as k'' = 28.55 N/m, making a total spring constant k_{total} = 31.83 N/m. The Poisson's ratio and the residual stress are taken as 0.31 and 30 MPa respectively [75], [21]. Seeing the two values, it is observed that the second component, which is due to the residual stress of Ni, dominates. Although all the material parameters are dependent on deposition conditions, the residual stress is a hard one to guess, and can vary widely. It was mentioned in [21] that the residual stress lies between 20-150 MPa. This seriously affects the spring constant and hence the actuation voltage. The actuation voltage for the above values is found as V_p = 134V using (2.25) for W = 74 μm, the first switch. The change of actuation voltage due to residual stress can be seen in Figure 3.4. The actuation voltage changes very rapidly due to the residual stress as expected.

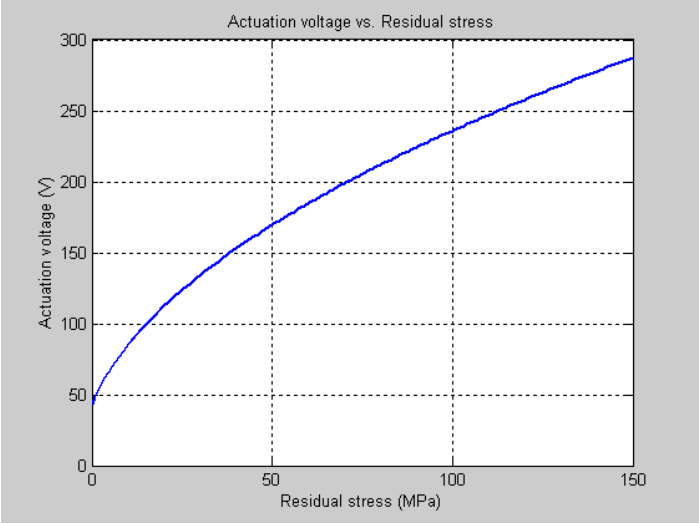

Figure 3.4 Change in the actuation voltage due to residual stress for W = 74 μm.

The measured actuation voltage is 130V. This result can be expected considering two cases; first the thickness of the MEMS bridge may vary because of electroplating setup. The thickness has a strong affect on actuation voltage. For example if the thickness is 2μm instead of 1μm, the actuation voltage rises about 130V from 100V in no residual stress case. The second case is the increase in the residual stress, affects of which can directly be seen in Figure 3.4.

Although the required actuation voltage is 130V, the amount of dissipated power is very low. This is because the power is dissipated only during the switching between states. Also since no DC currents are drawn, the required voltage can obtained with a DC-DC upconverter easily. Including the drive circuit, the switch dissipates about 0.1mW [21]. Another fact is that the switch is not sensitive to applied DC voltage changes. The switch shows hysteresis behavior, so that even the voltage values changes significantly from the applied values, the switch operation is not affected.

The mechanical quality factor of the MEMS switch is found using (2.27) as 0.34, and the switching time is found using (2.28) as 12.6 μs for an applied voltage, V_s, of 150 V. The mechanical resonant frequency of the switch is calculated as about 42 kHz [21].

3.2.2 Electromagnetic Design Phase

The important design parameters for a MEMS switch are isolation, insertion loss, return loss, bandwidth, switching time, power handling capability, and its lifetime. The shunt, capacitive MEMS switch design used in this thesis is a reflective type switch. It can be modeled a variable capacitance (for most of the cases), implemented by a MEMS bridge, between the signal and ground lines of a CPW. When the bridge is up, the capacitance, hence the coupling, between the

signal and ground is very low, letting most of the signal to pass to the output port. So, it should ideally have 0 dB insertion loss and -∞ dB return loss at up state. When the switch is actuated, the bridge comes very close to the signal line, just separated by a dielectric coating of thickness 0.1-0.3 μm, so the capacitance is increased very much. This situation results with a virtual short circuit to the ground, and the switch is closed. So at this state, the switch should ideally have -∞ dB isolation. The lower limit, which is about 5 GHz, for the band of operation is the impedance to the ground at the down state, which increases while the frequency decreases. But, this limit can be pulled down to 2 GHz using high dielectric constant materials [21]. The upper limit for the frequency of operation may be the increasing bridge parasitics in the down state. The switching time is a matter of mechanical design, and will not be mentioned here. The power handling capability of the MEMS switches is a wide subject, and is a recent topic of research. The failure mechanisms due to increasing temperature and current density such as self-actuation start at power levels of 100 mW. The details of the subject is out of the scope of this thesis, but the reader is advised to read [21] for a wide range criticization.

For most of the cases, MEMS switches can be modeled by a variable capacitor. The capacitance is in the order of fF for the up (on) state of the switch and a few pF for the down (off) state. The choice of capacitance values is very important for the performance of the design, because it directly determines the reflection at the on state, and hence it affects the loss at this state. The down state capacitance determines the isolation of the switch which is another important parameter of the switch.

The up-state capacitance has two components which are the parallel plate capacitance and the fringe field capacitance. The fringe field capacitance is about 20-60% of the parallel plate capacitance [21]. It depends mostly on the bridge

height and the center conductor width of the CPW. The total up-state capacitance of the structure is found by electrostatic FEM solver, Coventorware. It is seen that the fringe capacitance is about 40% of the parallel plate capacitance. For the down state case, the separation between the plates become very small, so the capacitance due to fringe fields can be neglected. The capacitance values for up and down states and the dimensions can be seen in Table 3.3. Here, the up state parallel plate capacitance is calculated using (2.31) and down state capacitance is calculated using (2.32).

Table 3.3 Up and down state capacitance values for MEMS switches.

Dimensions W × w (in Figure 3.3)	**$C_{uptotal}$ (fF)**	**$C_{up\text{-}pplate}$ (fF)**	**C_{fringe}/C_{pplate}**	**C_{down} (pF)**
74μm × 100μm for 200μm unit section	18.428	13.098	0.406	1.528
88μm × 100μm for 260μm unit section	21.386	15.576	0.373	1.817
116μm × 100μm for 420μm unit section	26.853	20.532	0.307	2.395

After the capacitances have been determined, the S-parameters are also ready, because these values are mostly the determiners for the S-parameters. Using the formulation in Section 2.3.2.2, it is easy to obtain the frequency characteristics of the S-parameters. However, these calculations must also be verified with electromagnetic simulators. For this purpose, Ansoft High Frequency Structure Simulator (HFSS) v8.5 is used.

Considering the simulation results, it is observed that the model with two transmission lines and a capacitor (or RLC circuit) can not be used to fit the simulated S-parameter data [21]. This is because the dimensions of the capacitor become too large to be considered as a lumped circuit element, and it is not feasible for modeling the complex field behavior at the MEMS bridge-CPW line transitions for the frequency band of interest (1-20 GHz). So, a new model should be used to fit the simulated data which can be seen in Figure 3.5.

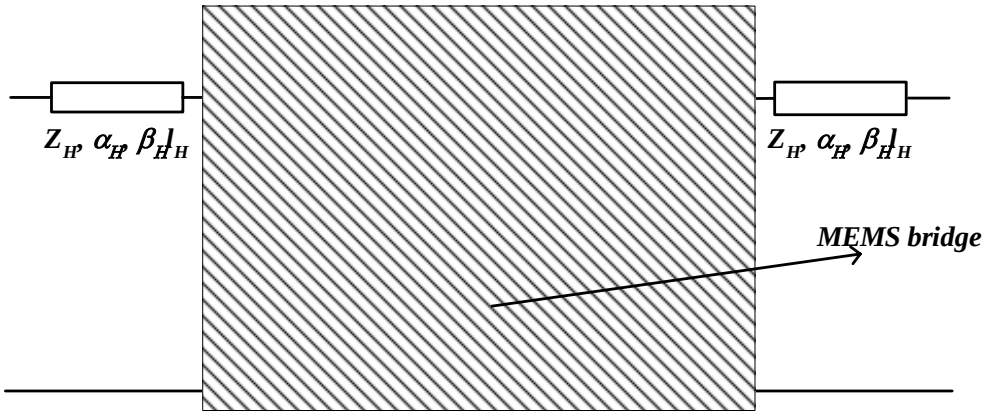

Figure 3.5 The fitted MEMS switch model.

In this new model, the MEMS bridge is modeled with a low impedance transmission line, and two series inductors with two parallel capacitors at both sides. The use of a low impedance line is understood better if the field distribution of a conductor backed CPW with a top cover is considered (Figure 3.6). As can be seen from the figure, the electric field is mainly coupled from the signal line of the CPW to its grounds. However, some parts of the field are also ended at the back conductor and the top cover. If the MEMS bridge is considered as a top cover, most of the field is expected to confine between the signal line and the top cover. This is because the distance between the signal line and the MEMS bridge (5μm)

is very small compared to distance to the CPW ground lines (~70μm) or to the back conductor (500μm). In this case, the CPW converges to a microstrip line where the ground of the microstrip is the MEMS bridge. The air gap between CPW layer and the MEMS bridge behaves as the dielectric layer of the microstrip line. The subject will be investigated further in Section 3.3.

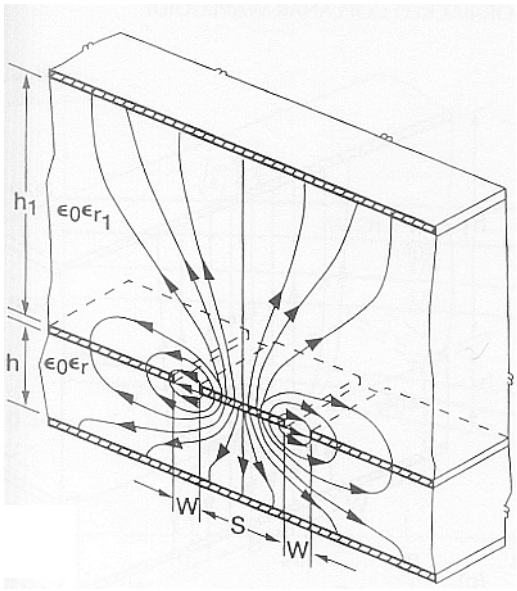

Figure 3.6 Field distribution of a CBCPW with a top cover [76].

Here, two sections of transmission lines, high and low impedance lines, on the MEMS switch model show different characteristics. High impedance line is a standard CPW which shows quasi-TEM behavior. In this line section, the field is mostly confined between the signal line and the planar ground in air and dielectric sections. This section of the line has a characteristic impedance about 70 Ω. However, when the field passes to the low impedance line, they mostly couple to the MEMS bridge, which is much more closer than both planar grounds and the back conductor ground. The characteristic impedance of this section abruptly

drops to 15 Ω levels, forming a sharp discontinuity. At the connection point of the two line sections, other circuit components are necessary to fit to the simulated structure. Capacitors are used to model the fringe fields occurring due to sharp endings of the lines. Inductors are used to model the change in the electrical length of the structure. This change may be due to sharp change of field behavior at the connection points.

To verify the model, the three switch structures with different signal line widths, *W,* are simulated using HFSS and compared with the results of the new model and the model only with a capacitor. The results can be seen in Figure 3.7.

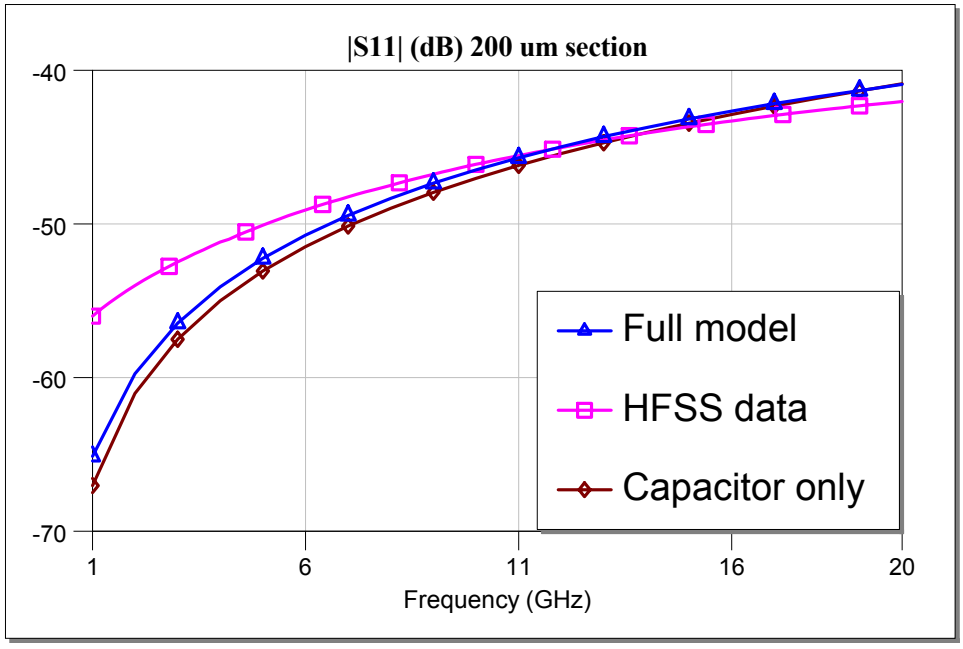

(a) Magnitude of S_{11} for the 200µm switch.

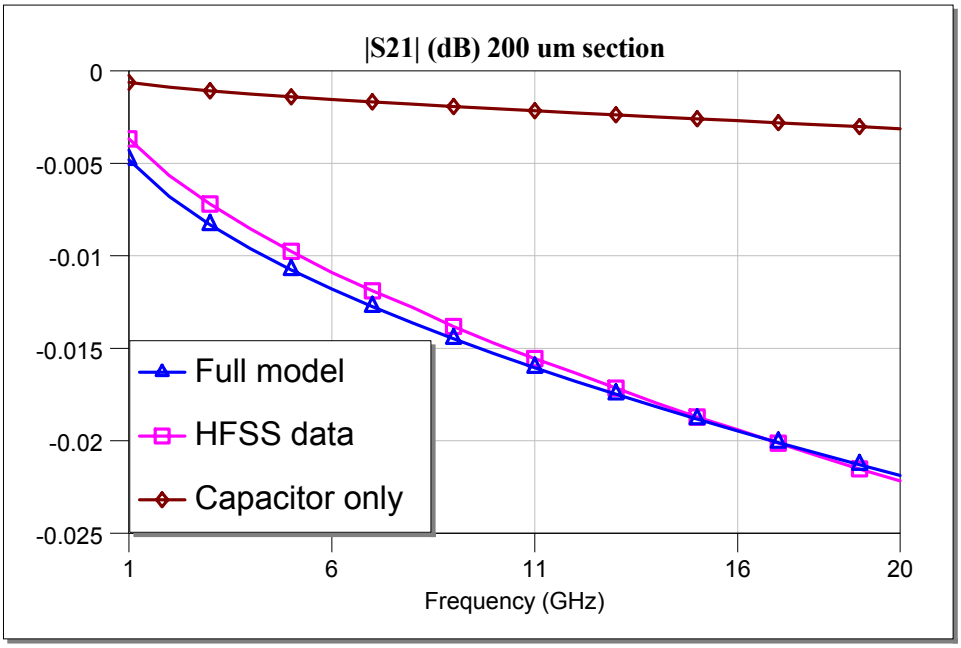

(b) Magnitude of S_{21} for the 200µm switch.

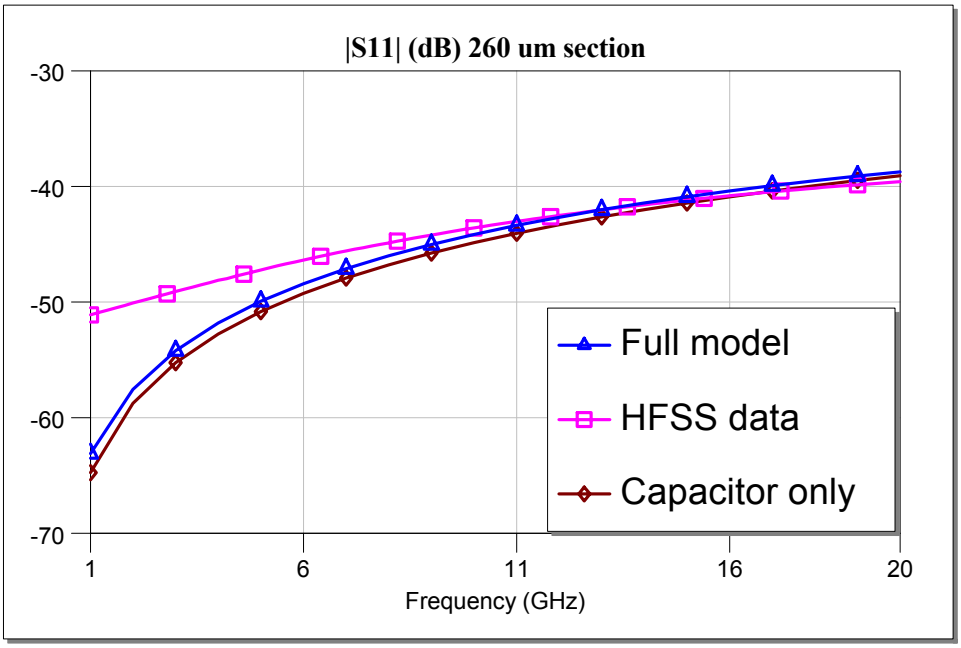

(c) Magnitude of S_{11} for the 260µm switch.

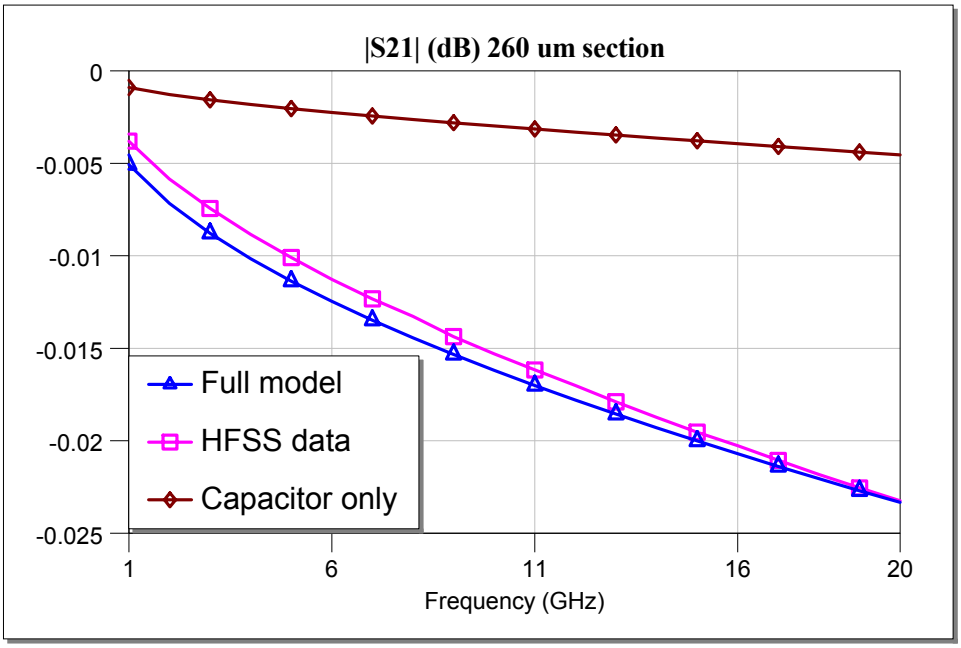

(d) Magnitude of S_{21} for the 260µm switch.

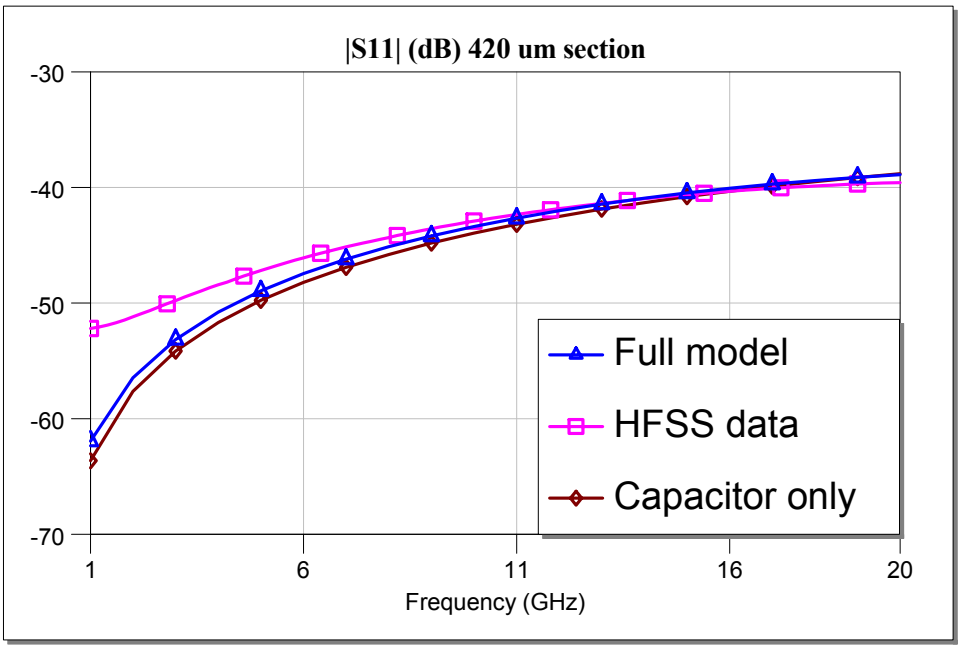

(e) Magnitude of S_{11} for the 420µm switch.

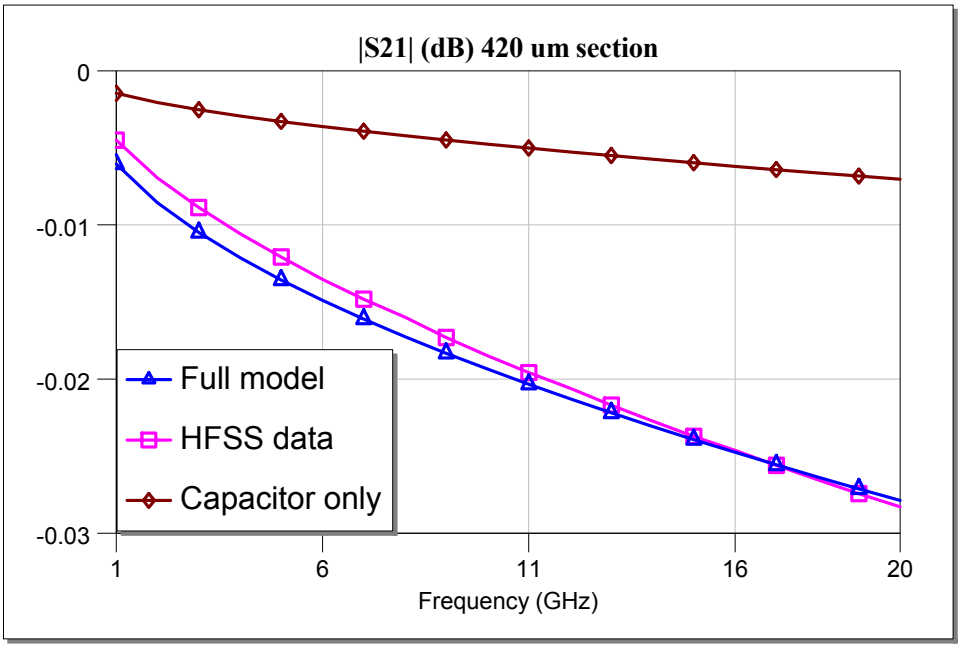

(f) Magnitude of S_{21} for the 420µm switch.

Figure 3.7 (a) to (f) S-parameters of the switches with total lengths 200µm, 260µm, 420µm.

The following values used in the schematic of Figure 3.5 are given in Table 3.4.

Table 3.4 (a) to (c) The values of the new MEMS switch model used in fitting.

(a) High impedance line calculated values.

Name	Z_H (Ω)	l_H (µm)	$\varepsilon_{eff,\,H}$	α_H (dB/m)
200µm switch	88.87	50	2.782	24.69
260µm switch	82.46	80	2.781	24.32
420µm switch	71.78	160	2.779	24.63

(Table 3.4 continued)(b) Low impedance line calculated values.

Name	Z_L (Ω)	l_L (μm)	$\varepsilon_{eff, L}$	α_L (dB/m)
200μm switch	21.88	100	1.133	111.64
260μm switch	18.92	100	1.135	112.54
420μm switch	14.91	100	1.137	113.87

(c) L, C, attenuation constants, and the up-state capacitance of capacitance only model.

Name	C (fF)	L (pH)	α_H (dB/m)	α_L (dB/m)	C_{up} (fF)
200μm switch	3.27	11.25	16.7	97.5	16.4
260μm switch	3.52	10.52	15.7	87.5	14.9
420μm switch	4.22	9.9	13.4	80	22.35

Table 3.4 (a) and Table 3.4 (b) are the calculated values using closed form formulas given in Sections 2.2 and 2.3. Table 3.4 (c) are the values that are used to fit the simulated S-parameters data to the model. The C_{up} values are the values of the model with only a capacitance as a MEMS bridge. As seen in Figure 3.7, the model mostly fits both S_{11} and S_{21}. The capacitance only model also fits the S_{11} characteristics, but it is far away from fitting S_{21} characteristics. These results show that the capacitor only model ([21]) does not actually hold for our case. The extra inductors and capacitor used at the junction in the new model have better performance in terms fitting the simulated results. This case will be further explained in Section 3.3.

Another important fact to mention at this point is the accuracy of the electromagnetic simulations. It is observed during the simulations that increasing the number of meshes in the FEM solver directly affects the shape of the S_{11} characteristics, especially at the lower end of the band. This is an expected result,

because at the lower end of the band, the values become very small, so they are seriously affected by numerical errors. The accuracy of these simulations is limited by the accuracy of the program.

3.3 Variable Length MEMS Stub Design

After the unit section of the variable stub has been modeled, the next step to the variable MEMS impedance matcher is to make a variable length short circuited stub. For this purpose, you need a transmission line on which you can place a short circuit at a determined point. This is obtained by connecting the MEMS capacitive shunt switches as serial elements. When the switches are in the up state, the signal flows through the switches with a small amount of insertion loss. Since the stub should have a short circuited end, the switch at the required length of stub is actuated, forming a capacitive short circuit to ground.

Here, the performance of the stub is measured with the input impedance seen into the one port stub. The reason for this is that the triple stub matching solution requires some predefined amount of susceptances added by the stubs as explained in Section 2.1. However, this is not possible since the transmission lines used have some insertion loss, adding a real part to the admittance seen into the device. The real part added by the stub, of course, disturbs the solution for the matcher, and a new solution should be found considering the losses of the CPWs used. The end capacitance, which is the actuated MEMS switch at the end point of the stub, is also different then a real short circuit. It changes the electrical length of the stub and must be considered in the calculations.

Considering the facts mentioned above, the first step of the design phase is to make EM simulations of the MEMS stub. HFSS v8.5 program is again used for this purpose. The program uses FEM method to simulate the structures. The

model created to simulate an 8-bridge stub can be seen in Figure 3.8 as an example. Here, first seven bridges are in the up state, where the 8th bridge is actuated and it is in the down state.

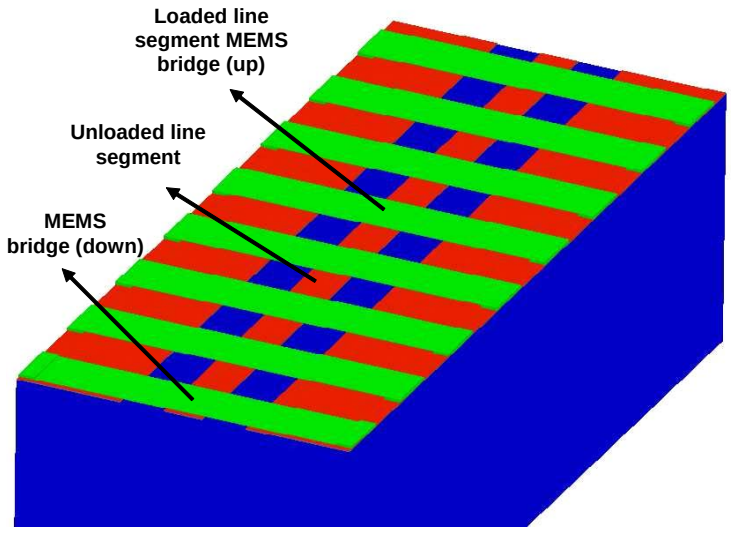

Figure 3.8 The HFSS model for an 8-bridge stub.

From the simulation results, it is possible to obtain S-parameters of the structures, port impedances, and the field distributions. The field distributions are important to understand the behavior of the structure. It was stated in the previous subsection that the field is mostly expected to confine between the MEMS bridge and the signal line of the CPW when it is passing through the MEMS bridge. This can be observed in the electric field distribution in Figure 3.9. The field changes direction in a very short length which may be the reason for the capacitive behavior at these points. Another interesting behavior is observed in the z-component of the electric field. In CPW structure, the z-component of the field is estimated to be very small, so that the structure is named as a quasi-TEM structure. However, when it is loaded with air bridges, which is our case, this field behavior changes drastically because of the close spacing in between the MEMS

bridges. In other words, the field distribution is affected by the MEMS bridges and the spacing between the bridges is not enough for the fields to reach to steady state (to unloaded state). This is most probably the reason of the change in electrical length for which inductors are used as a model. The z-component of the electric field can be seen in Figure 3.9.

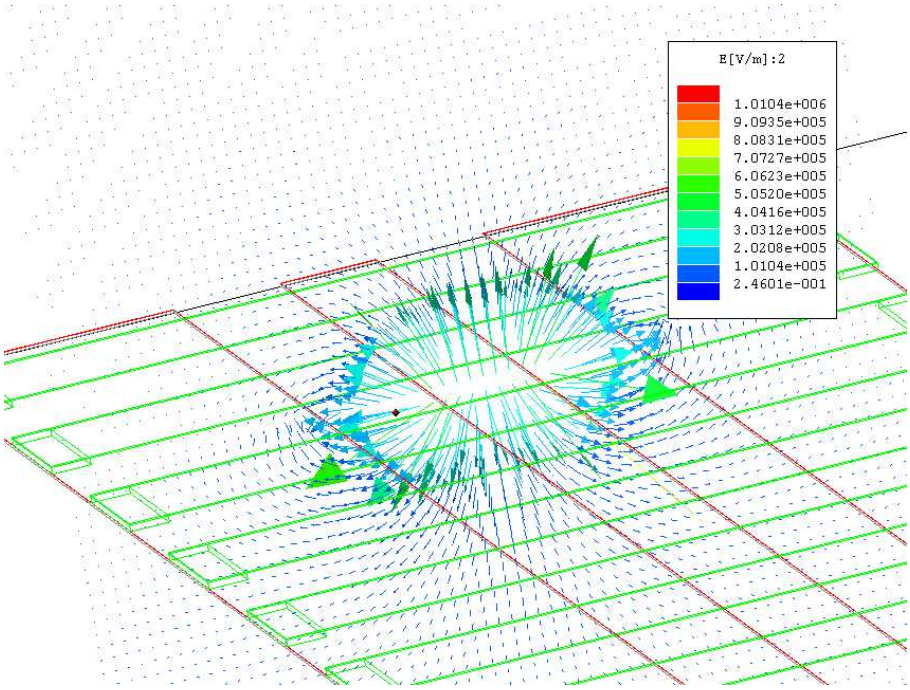

(a) The transversal electric field distribution in the unloaded section of the stub.

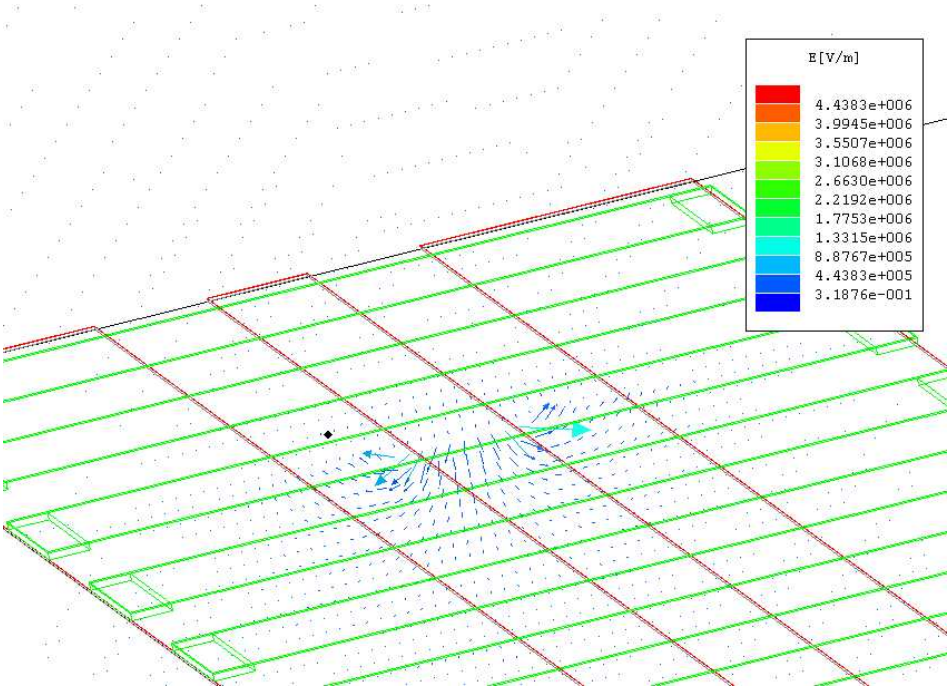

(b) The transversal electric field distribution in the loaded section of the stub.

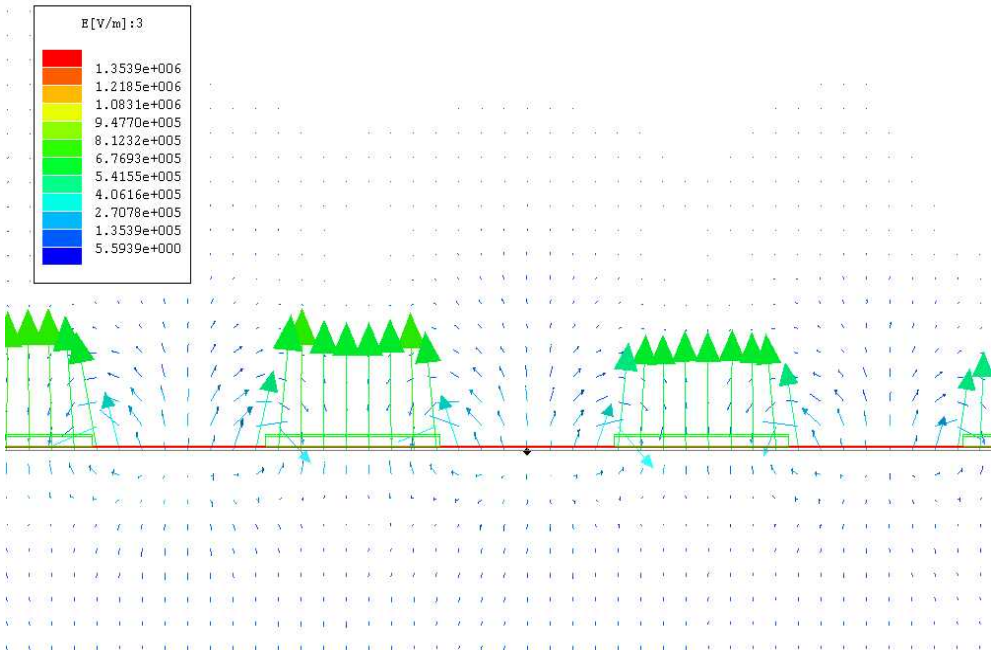

(c) The longitudinal field distribution through the stub.

Figure 3.9 (a) to (c) The field distribution of the simulated MEMS variable length stub.

The EM simulations are made for all three types of stubs in which the interbridge spacings are 100µ, 160µ, and 320µ. But for the 100µ case only, the simulations are swept from 2 bridge case to 16 bridge case with an increase of 2 in the bridge number. The simulations for stubs with more number of bridges are not possible because of the simulator program limitations, because, the mesh size, thus the memory usage, in the EM model increases to unaffordable values.

After the simulations are completed, the next step is to compare the simulation results with the proposed schematic model. The unit section of the model was given in Figure 3.5. The schematic for the stub is obtained cascading a number of unit sections and connecting a capacitance for the final switch. The model for a 4-bridge stub can be seen in Figure 3.10.

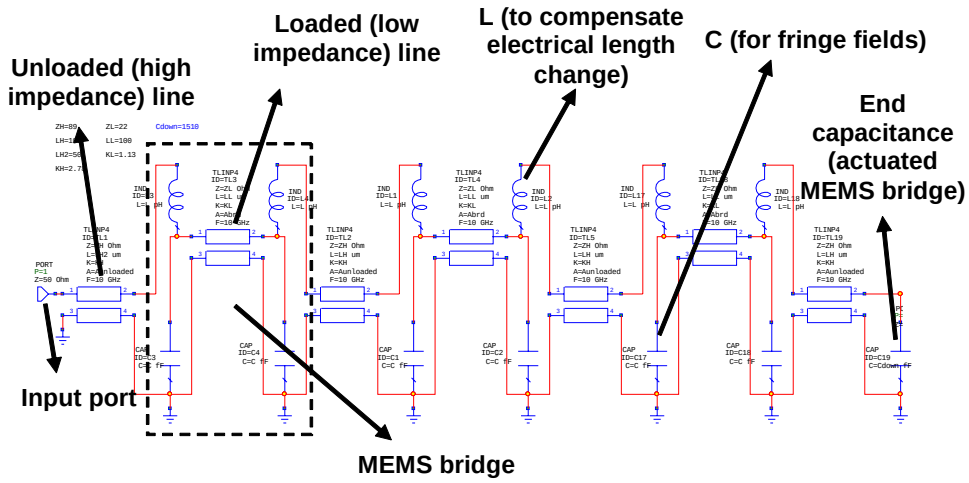

Figure 3.10 Schematic model for a 4 bridge MEMS variable stub.

Using the above model, the simulation results are compared with the EM simulation results. The variables *L, C,* α_L, and α_H of model in Figure 3.5 are tuned

to fit the real and imaginary parts of Z_{11} of the one port stub obtained from the simulation results. This is done for all stubs with 2 to 16 bridges and with bridge spacings of 100μm. The model is also checked for 10-bridge stubs with 160μm and 320μm bridge spacings. The obtained results can be seen in Figure 3.11. *As can be seen from the results, the characteristics almost exactly fit in most of the cases*. The only differences are seen in the real parts of 2-8 bridge cases. In these cases even, the characteristic shapes are the same. For the first two cases, the reason may the numerical errors inserted by the HFSS solver. This suspicion arises from the oscillations occurring in the bottom border of the line. Another observation made from the imaginary parts of the graphs is that they all start with a negative value of around -100Ω, which is also an expected result of capacitive termination at the end of the stub.

The other model given in Figure 2.11 in Section 3.2.2, which was composed of equally spaced capacitances over the transmission line, also seems to fit the simulation results, *however, the values of the elements are far away from the physical values.* The equivalent line length becomes significantly larger to fit the imaginary part of Z_{11} and the resistance R in Figure 2.11 becomes to large to fit the real part of Z_{11}, which is hard to explain with the transmission line-capacitance model. The physical values and fitted values can be seen in Table 3.6.

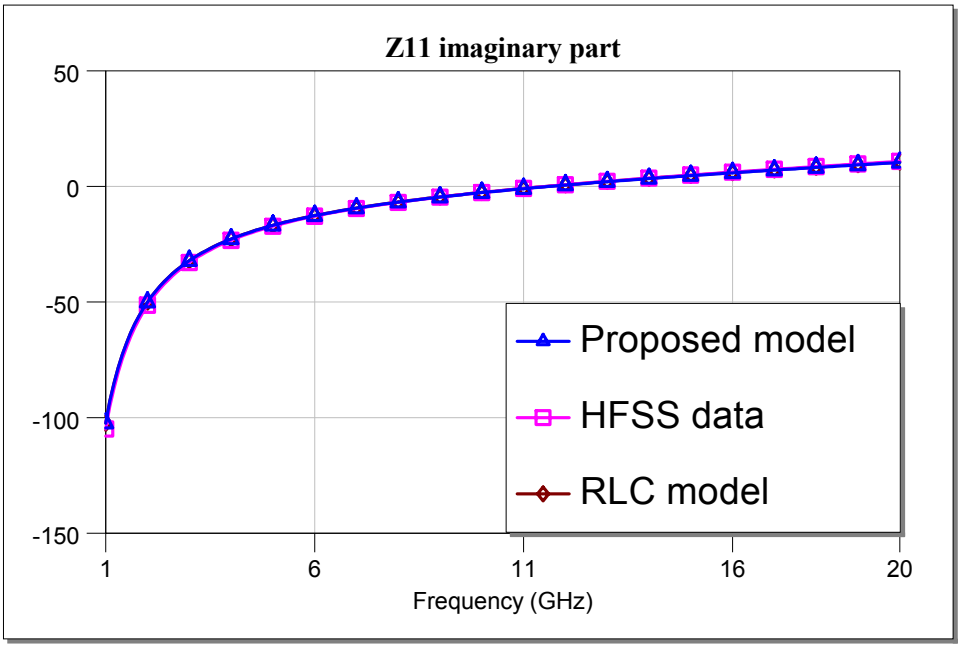

(a) Imaginary part of Z_{11} for a 2 bridge stub (100µm spacing).

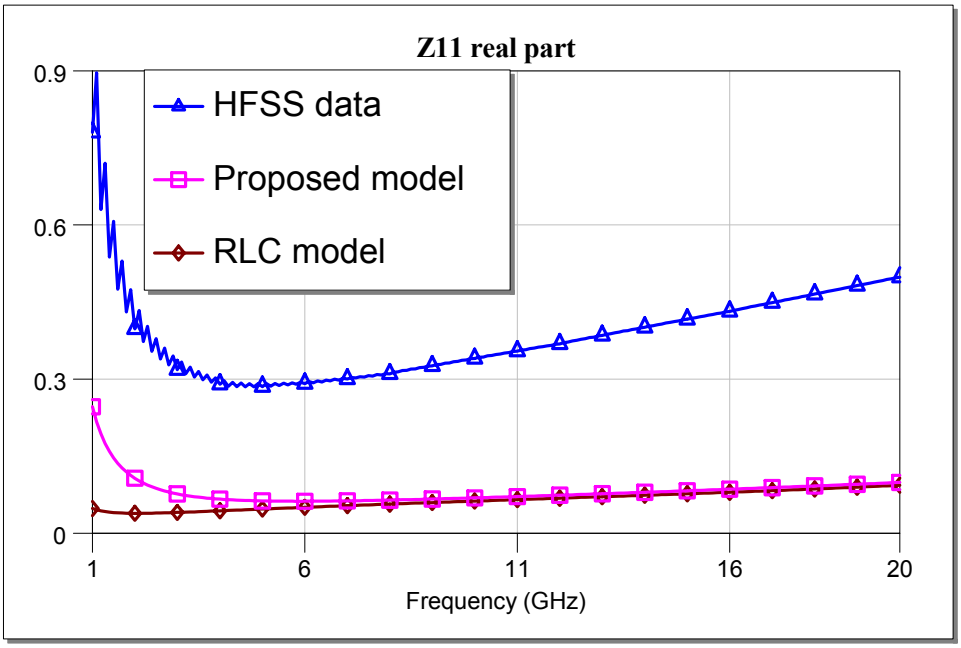

(b) Real part of Z_{11} for a 2 bridge stub (100µm spacing).

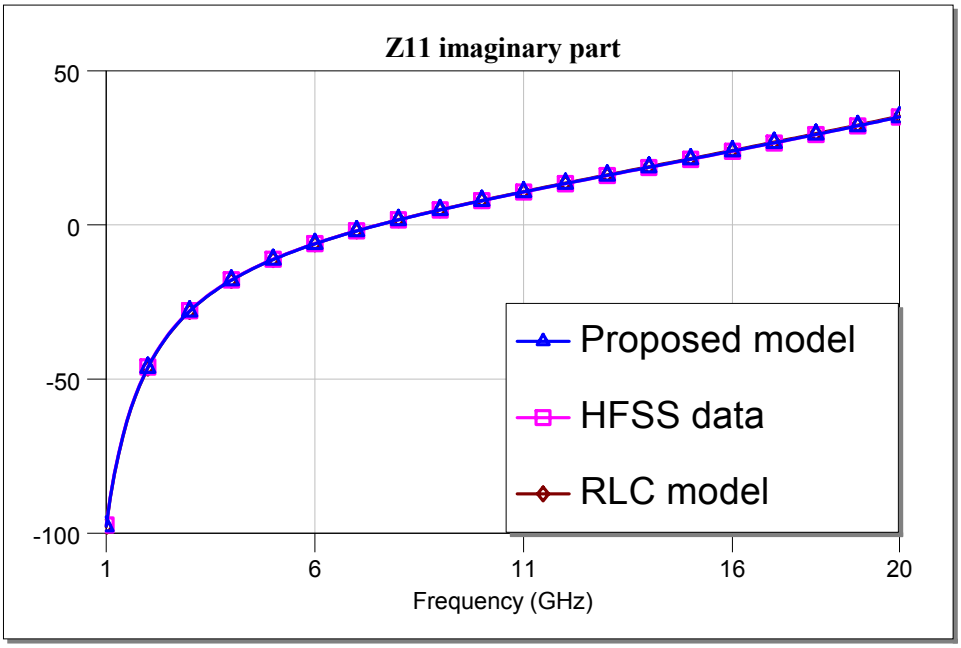

(c) Imaginary part of Z_{11} for a 4 bridge stub (100µm spacing).

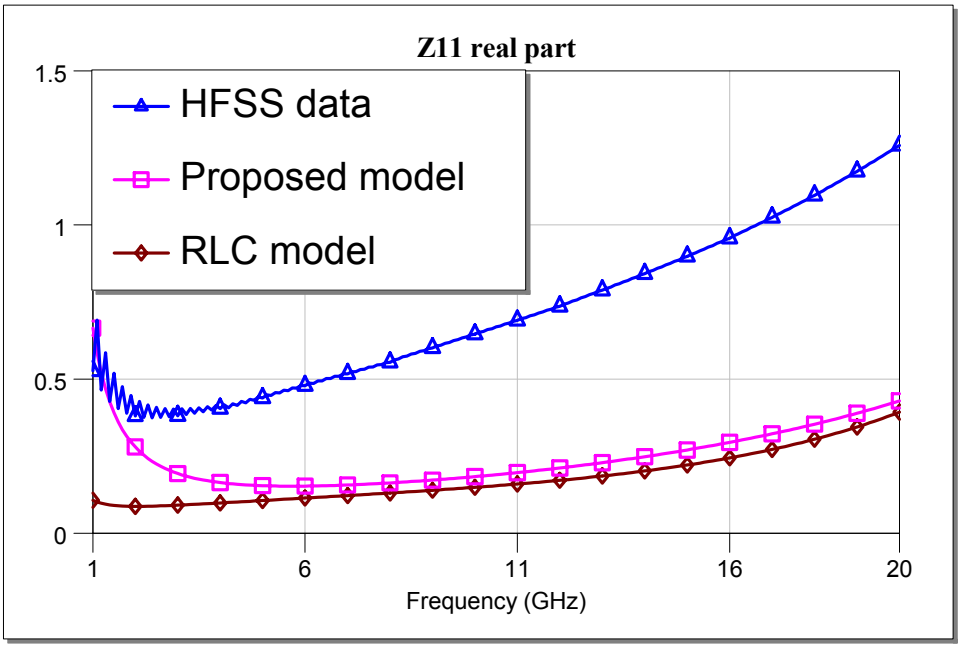

(d) Real part of Z_{11} for a 4 bridge stub (100µm spacing).

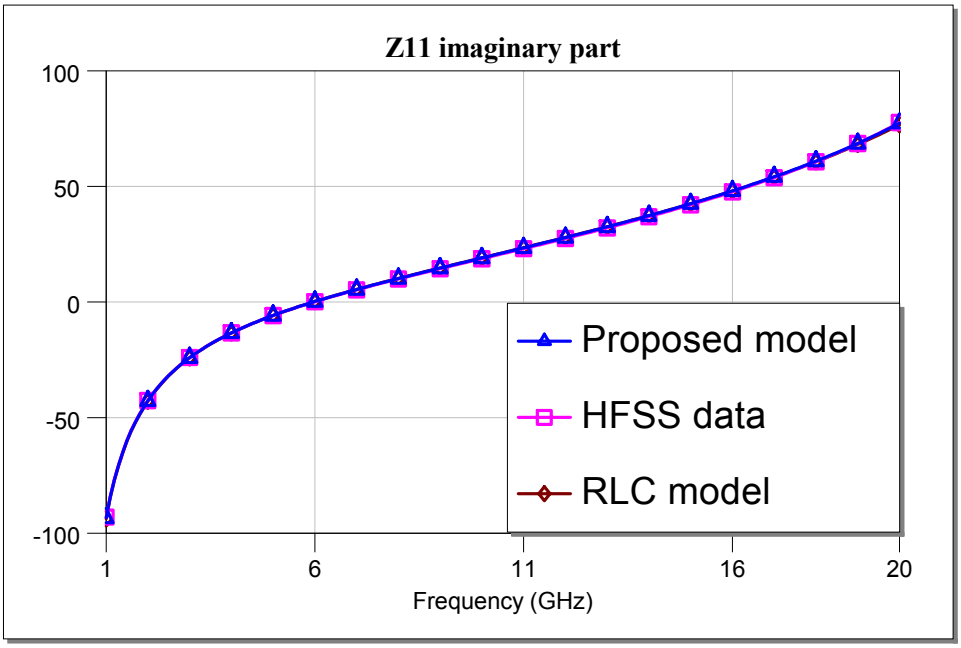

(e) Imaginary part of Z_{11} for a 6 bridge stub (100µm spacing).

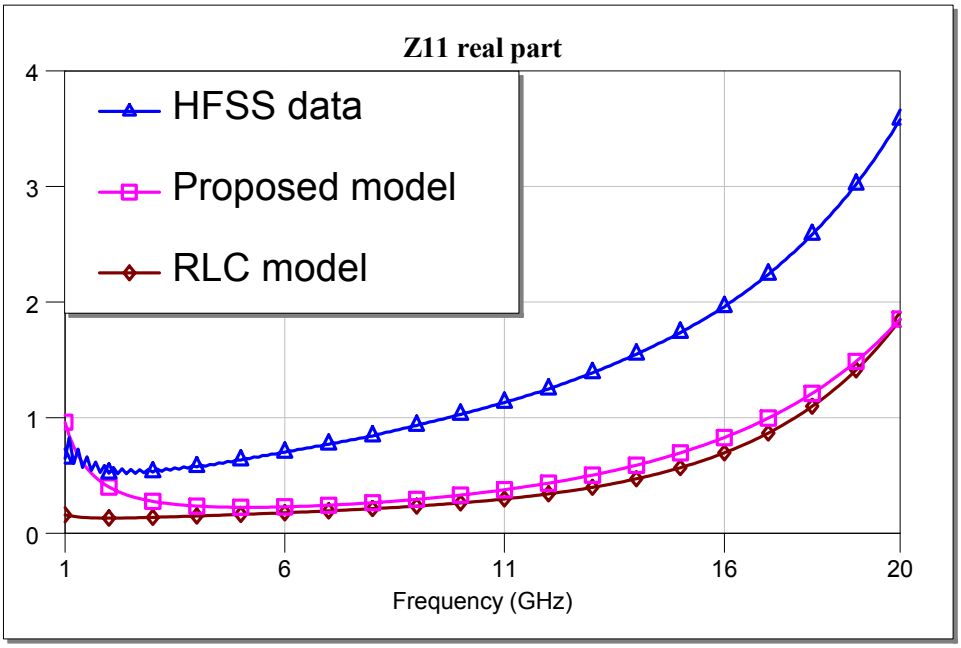

(f) Real part of Z_{11} for a 6 bridge stub (100µm spacing).

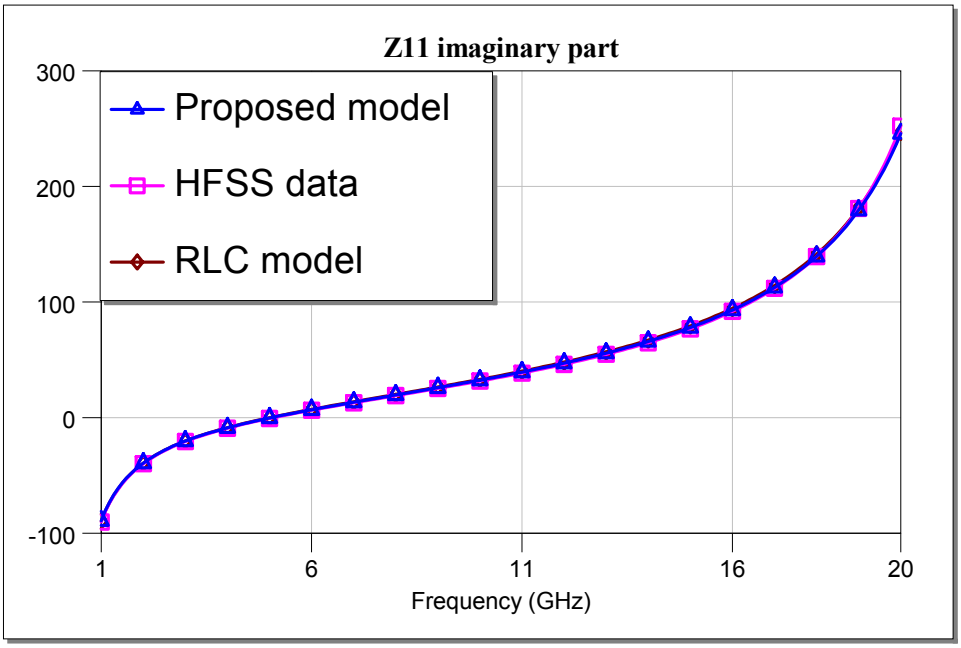

(g) Imaginary part of Z_{11} for an 8 bridge stub (100µm spacing).

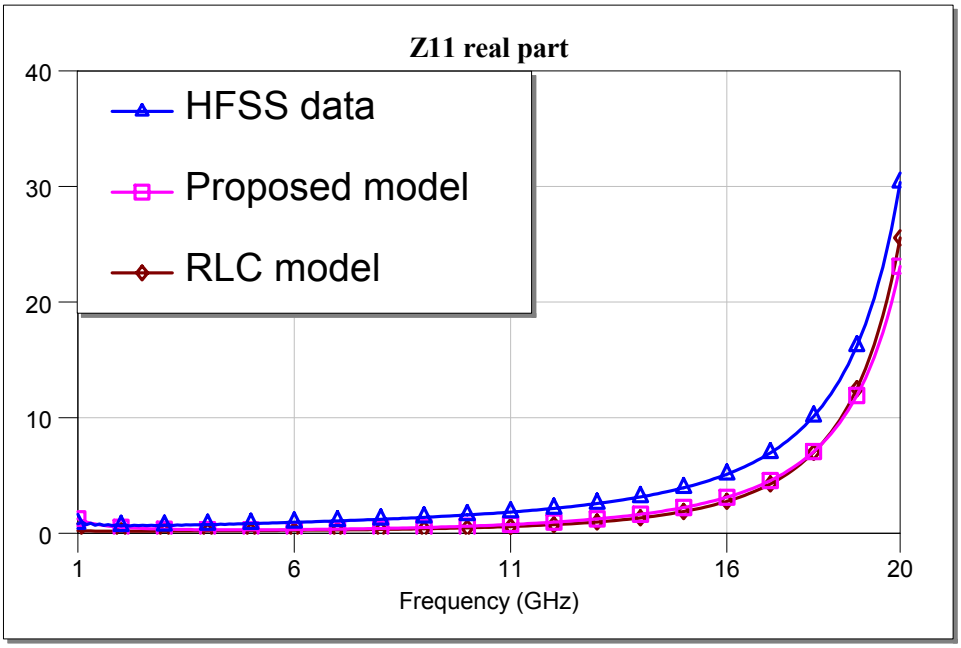

(h) Real part of Z_{11} for an 8 bridge stub (100µm spacing).

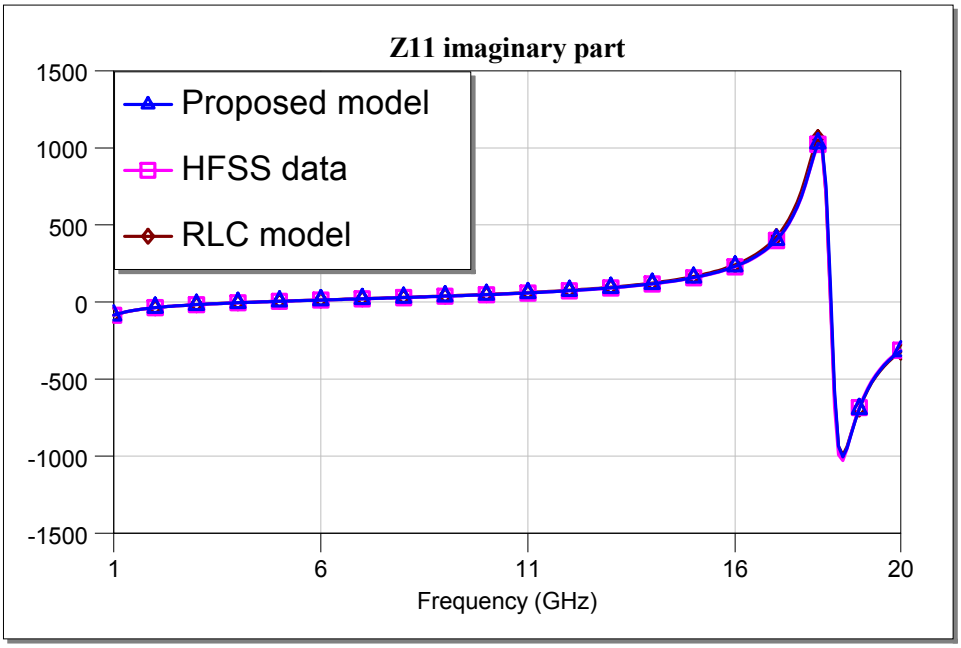

(i) Imaginary part of Z_{11} for a 10 bridge stub (100µm spacing).

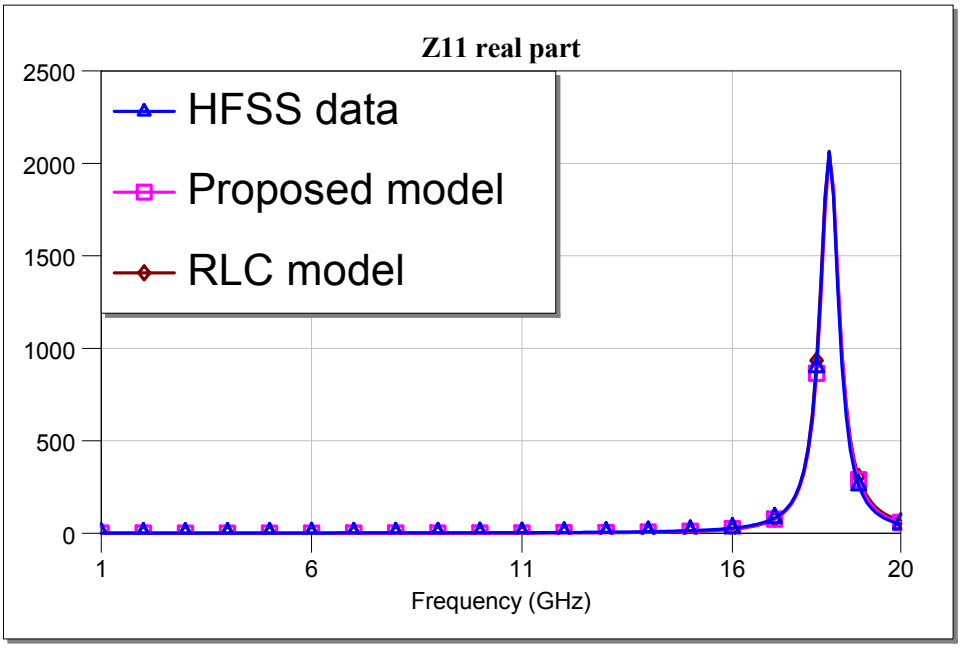

(j) Real part of Z_{11} for a 10 bridge stub (100µm spacing).

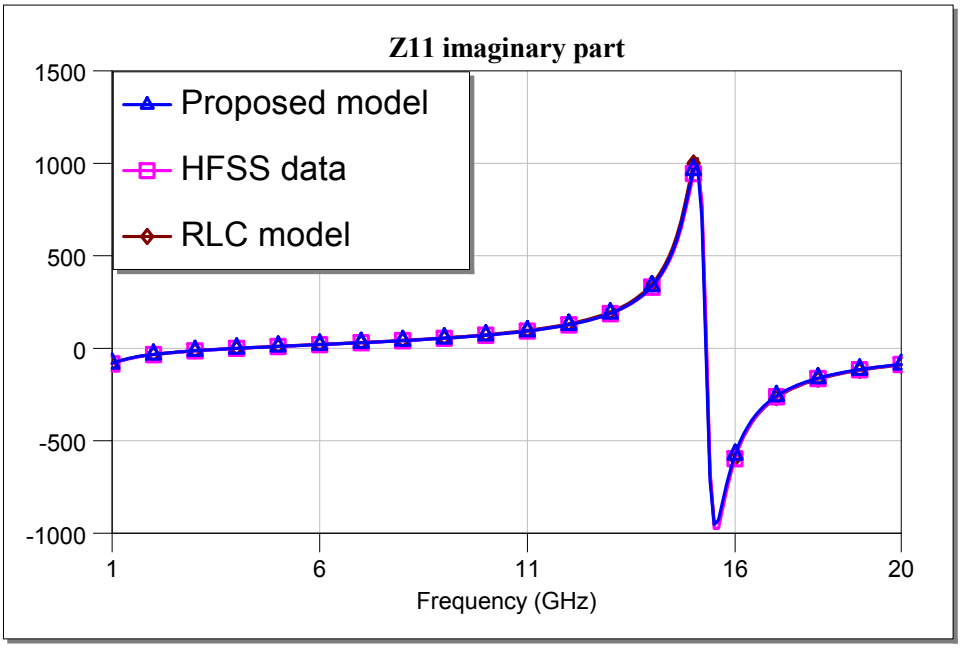

(k) Imaginary part of Z_{11} for a 12 bridge stub (100µm spacing).

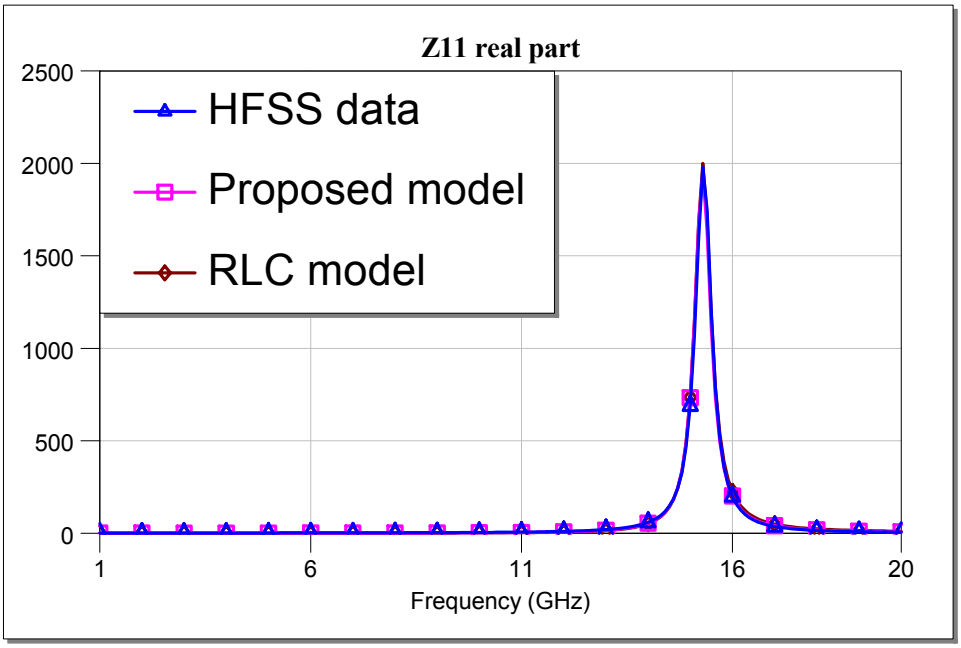

(l) Real part of Z_{11} for a 12 bridge stub (100µm spacing).

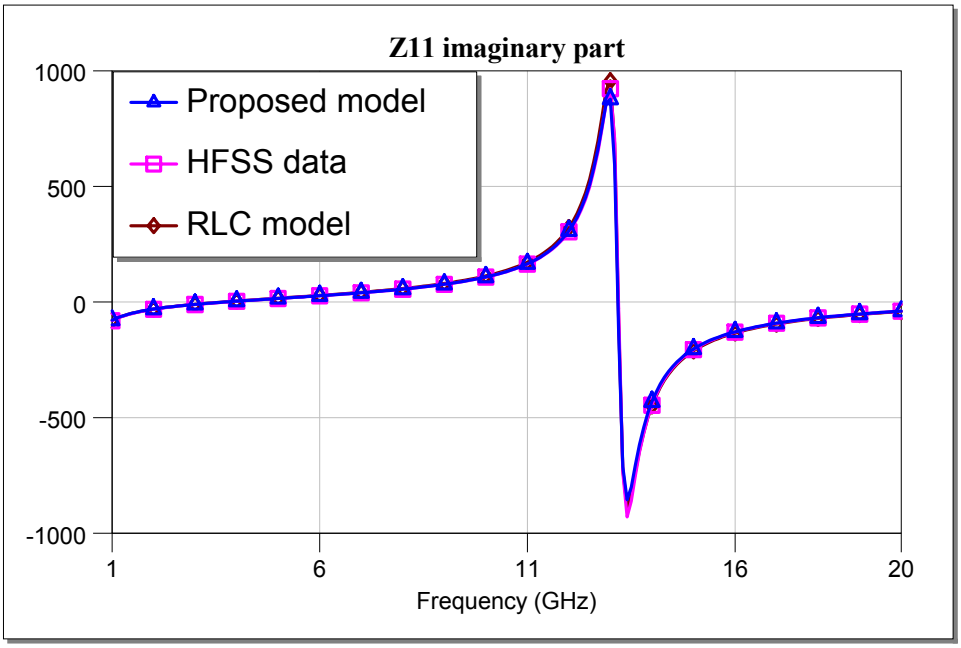

(m) Imaginary part of Z_{11} for a 14 bridge stub (100µm spacing).

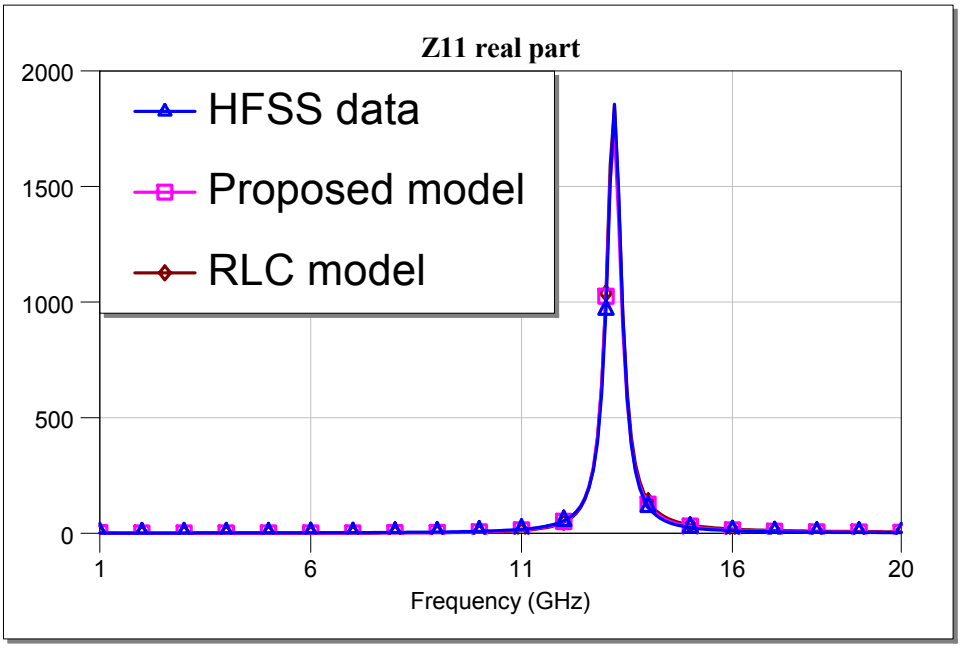

(n) Real part of Z_{11} for a 14 bridge stub (100µm spacing).

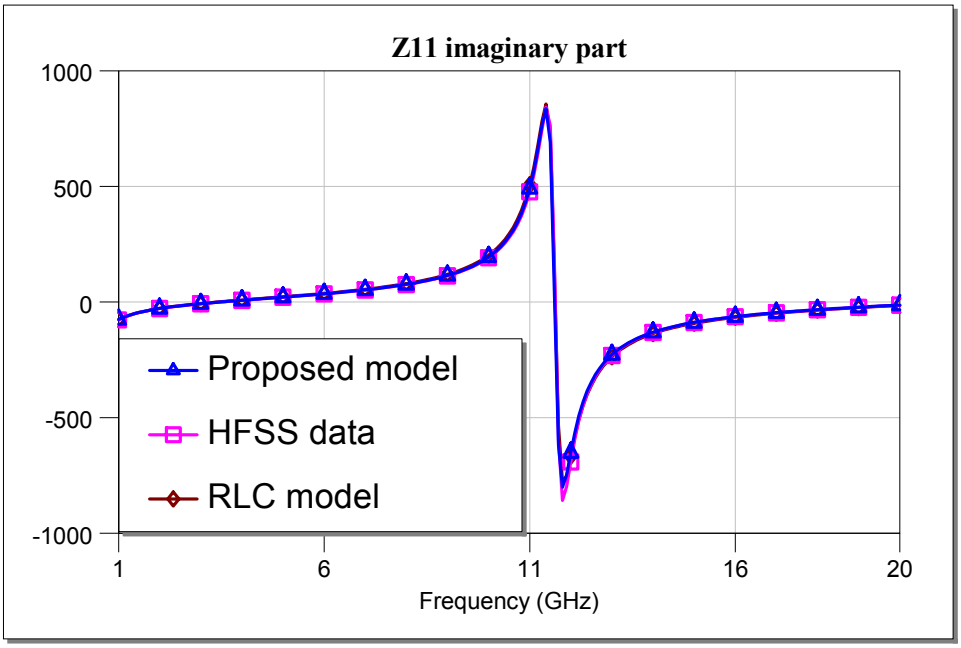

(o) Imaginary part of Z_{11} for a 16 bridge stub (100µm spacing).

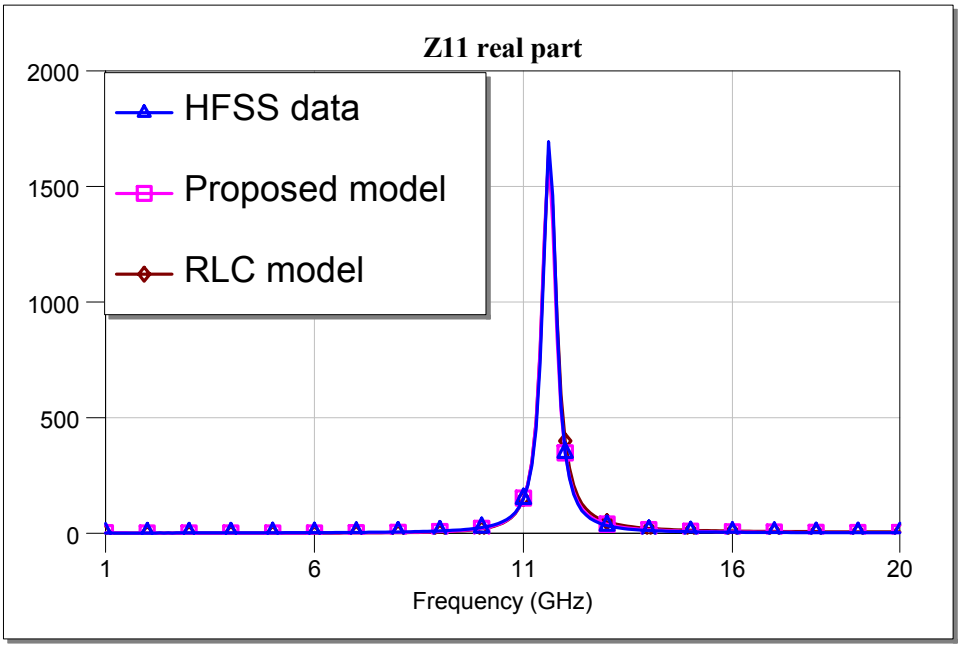

(p) Real part of Z_{11} for a 16 bridge stub (100µm spacing).

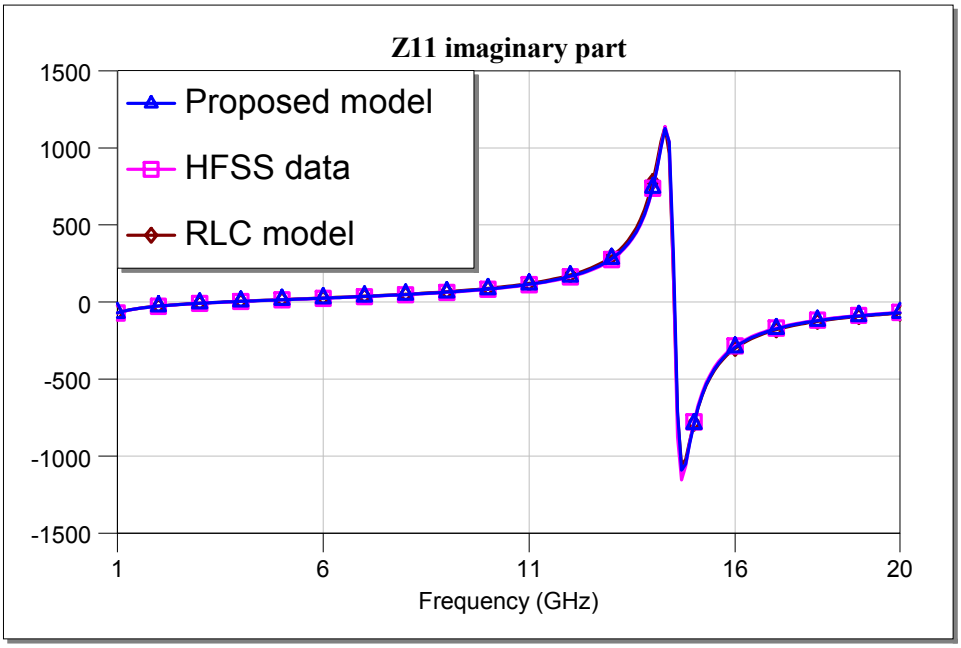

(q) Imaginary part of Z_{11} for a 10 bridge stub (160µm spacing).

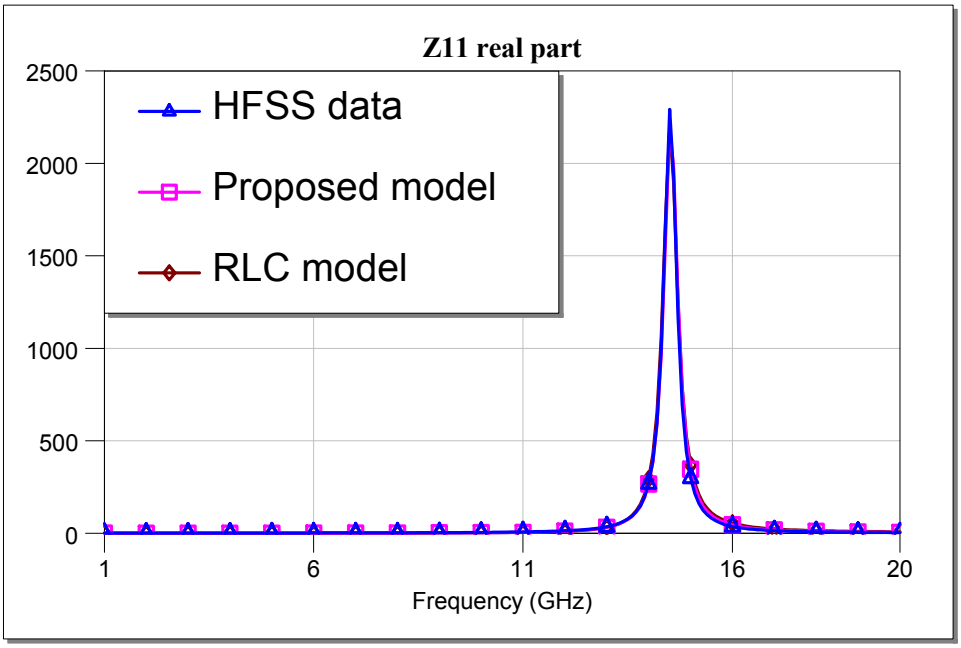

(r) Real part of Z_{11} for a 10 bridge stub (160µm spacing).

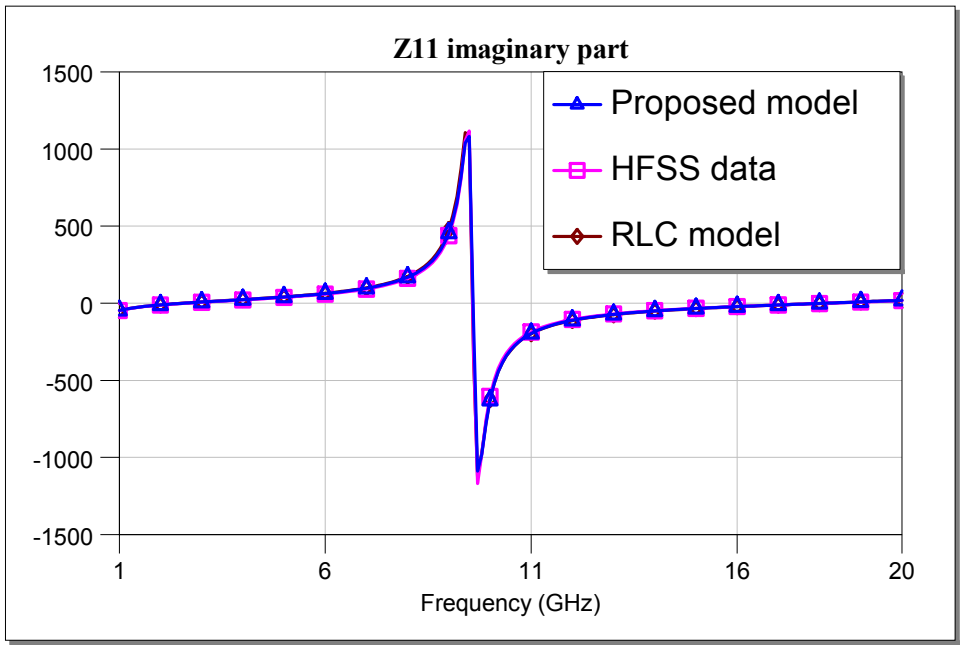

(s) Imaginary part of Z_{11} for a 10 bridge stub (320µm spacing).

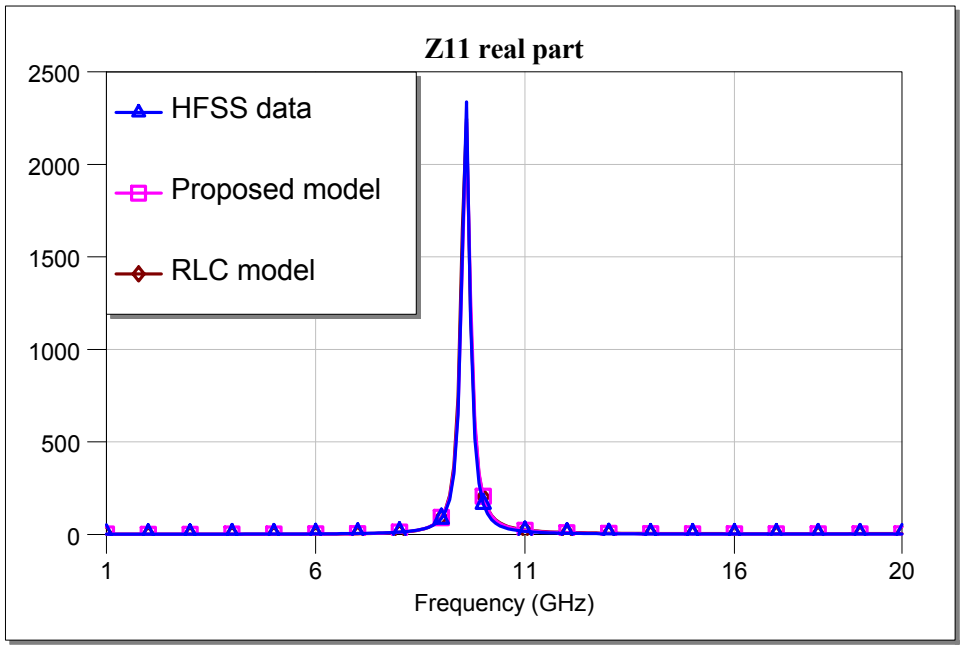

(t) Real part of Z_{11} for a 10 bridge stub (320µm spacing).

Figure 3.11 (a) to (t) Imaginary and real parts of Z_{11} obtained from HFSS EM simulations and the proposed model.

The values of circuit elements of the proposed model in Figure 3.5 and Figure 3.10 that is used to fit the HFSS simulation results can be seen in Table 3.5. C_{END} is the value of the capacitance that is used to model the actuated MEMS bridge. The fitted values are very close to the calculated values in Table 3.3. The loss values, α_H and α_L, are also close to the calculated values in Table 3.4.

Table 3.5 The schematic element values of the proposed model that is used to fit the simulation results.

# of bridges	Bridge Spacing (µm)	C_{END} (pF)	α_H (dB/m)	α_L (dB/m)	C (fF)	L (pH)
2	100	1.51	24	112	3.27	21.65
4	100	1.51	24	112	3.27	15.35
6	100	1.51	24	112	3.27	14.75
8	100	1.51	24	112	3.27	14.75
10	100	1.51	24	112	3.27	13.9
12	100	1.51	24	109	3.27	13.7
14	100	1.51	24	109	3.27	13.5
16	100	1.51	24	109	3.27	13.4
10	160	1.788	24	95	3.3	13.9
10	320	2.4	24	80	3.6	14.3

On the other hand, the element values used for the transmission line-capacitance model in Figure 2.11 are much different than the physical design values. These values can be seen in Table 3.6. *Here, the bridge spacing needs to be extended to more than its physical value. The resistance that is used as a part of the MEMS bridge also has values about 20-30Ω, which makes no physical sense. It seems that the bridge inductance has also negligible affect on curve*

fitting. This means that even both of the models can fit the curves, it is more convenient to use the first model with which we can physically explain the reasons of the components used in the model.

Table 3.6 The element values for the transmission line-capacitor model that is used to fit the simulation results.

# of bridges	Bridge Spacing (μm)	Fitted Bridge Spacing (μm)	α_H (dB/m)	R (Ω)	C (fF)	L (pH)
2	100	169	24	22	16.4	0
4	100	169	24	22	16.4	0
6	100	169	24	22	16.4	0
8	100	173	24	22	16.4	0
10	100	173	24	22	16.4	0
12	100	173	24	27	16.4	0
14	100	173	24	33	16.4	0
16	100	173	24	43	16.4	0
10	160	239	24	26	18	0
10	320	408	24	29	22.4	0

It was pointed out before that the input impedance of the stub was the determiner for the triple stub matcher. Then, it is necessary at this point to give the input impedance of a stub with bridge numbers from 1 to 40. The reader might remember that the HFSS simulations were made for stubs with even number of bridges from 2 to 16 bridges. Nevertheless, since the model was fitted with the simulated cases accurately, the fitted model is used to find the input impedances for the cases that EM simulation was impracticable. In fact, this is the reason for developing a schematic, short hand model which allows to designer to predict the

device behavior without long EM simulations. The results can be seen in Table 3.7.

Table 3.7 The input impedance values of the variable length stub with different switch positions actuated.

Actuated switch position	Input impedance (Ω)	Actuated switch position	Input impedance (Ω)
1	0.011-j8.94	21	45.8-j233
2	0.061-j3.58	22	24.4-j161
3	0.109+j1.7	23	15.6-j121
4	0.16+j6.94	24	11.2-j94.6
5	0.221+j12.4	25	8.64-j76.3
6	0.298+j18.1	26	7.02-j62.4
7	0.399+j24.1	27	5.93-j51.3
8	0.539+j30.8	28	5.17-j42.1
9	0.738+j38.2	29	4.63-j34.2
10	1.03+j46.7	30	4.24-j27.3
11	1.47+j56.8	31	3.96-j21
12	2.17+j69.3	32	3.78-j15.1
13	3.33+j85.3	33	3.67-j9.59
14	5.42+j107	34	3.63-j4.25
15	9.63+j139	35	3.66+j0.997
16	19.7+j193	36	3.75+j6.26
17	52.6+j301	37	3.93+j11.6
18	271+j609	38	4.21+j17.3
19	1030-j697	39	4.6+j23.2
20	128-j400	40	5.16+j29.7

3.4 MEMS Triple Stub Matcher

Once the variable length stub is designed, the design of the variable MEMS triple stub matcher is almost finished. This is because the variable triple stub matcher consists of tree variable stubs and two transmission lines of length $\lambda/8$ connecting the stubs. Since the transmission lines (CPW in our case) have fixed length, their design is only limited to tune their impedances to be 50Ω and minimize their loss. However, at the connection point of the connecting CPWs and the stubs, which are also built upon CPWs, T-junctions occur.

T-junction is discontinuity for CPW and its characteristic shifts compared to an ordinary connection of three ports. The reason of this shift in the characteristic is the excess amount of current accumulating on the edges of the ground and signal lines of the incoming CPWs [77]. Fringe fields also exist in the junction area disturbing the junction characteristics [78]. There are known solutions to reduce the effects inserted by a T-junction some of which are using air bridges at each port or elevating the junction area and coating the area underneath the junction with a high dielectric constant material [76].

Any solutions mentioned above were not applied to the T-junctions in the triple stub matcher of this thesis. But instead, its EM simulations were made and the results were fitted to the model given in [76]. This is necessary to be able to guess the change in the device characteristics. The schematic of the model used for the T-junction can be seen in Figure 3.12. Here, the inductances are used to model the excess currents occurring at each port, and the capacitance is used to model the fringe fields.

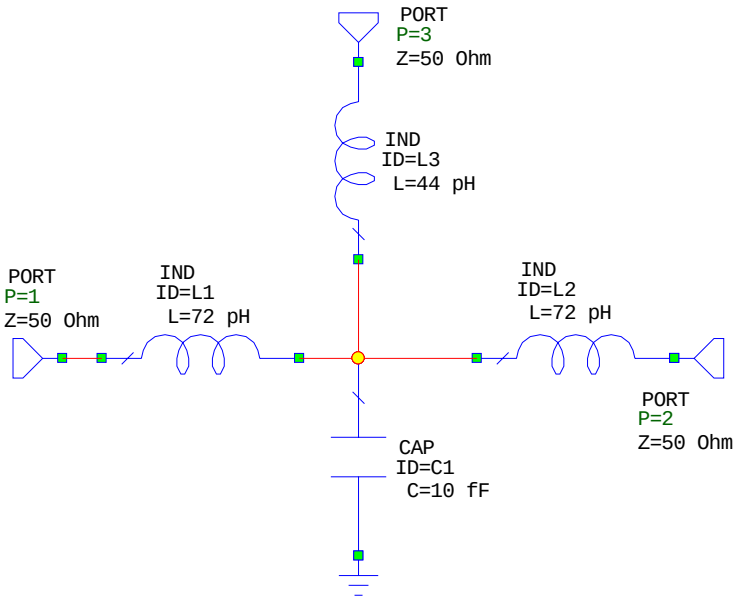

Figure 3.12 The model used to fit the T-junction.

The inductance and capacitance values used in the model are used to fit the model behavior with the simulated HFSS EM simulations. The simulated and modeled characteristics can be seen in Figure 3.13. From the figures, it is observed that the proposed model fits very well with the EM simulation results.

After the T-junction model is verified, the next and the final step in the design is to bring all the parts together and make final simulations. To do this, first, analytical solution is found using the formulas given in Section 2.1.2 and 2.1.3. What actually done here is to apply the double stub-matching to the load seen into the point where 2nd stub is connected (please refer to Figure 2.5). This is because the 3rd stub and the transmission line between 2nd and 3rd stubs are only used to transfer the load to another value, to prevent the forbidden region limitations of the double-stub matching. In other words, a bridge is selected from the 3rd stub and the double-stub matching is applied to transform the load to the a desired value at the input port.

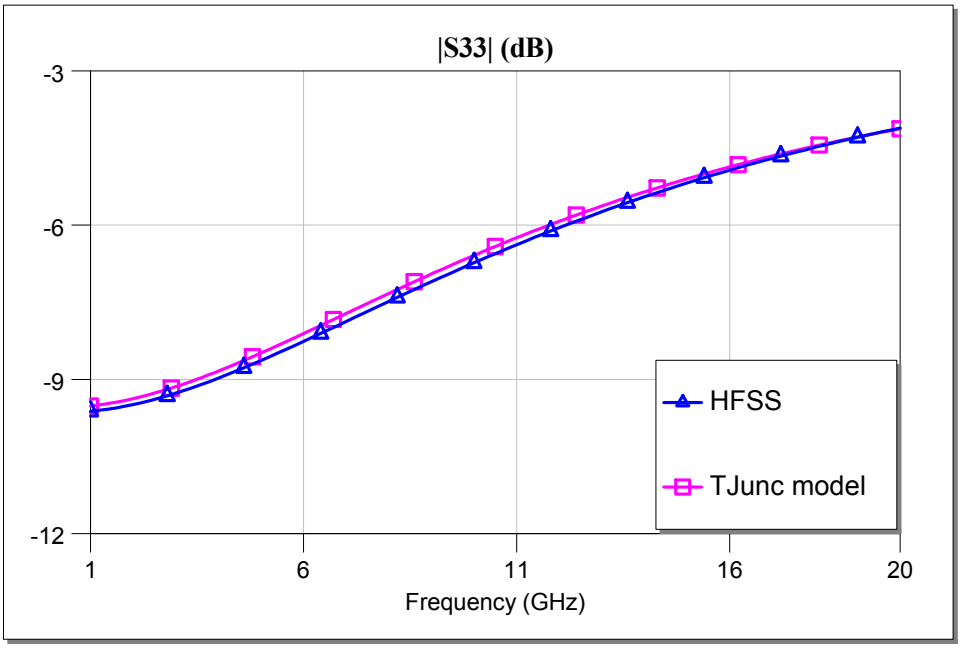

(a) Comparison of $|S_{33}|$ for the simulated T-junction and proposed model.

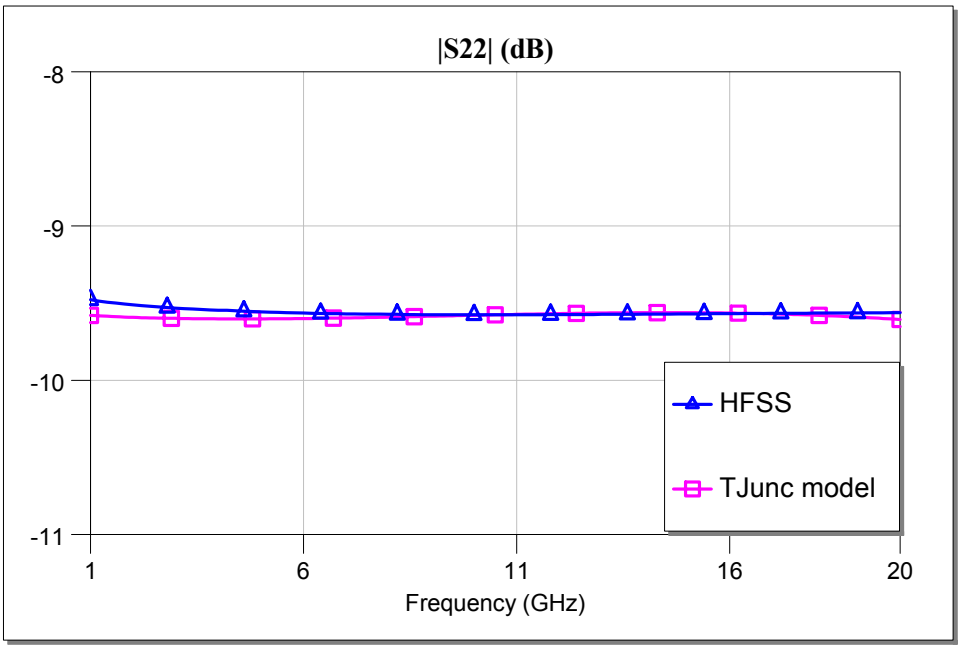

(b) Comparison of $|S_{22}|$ for the simulated T-junction and proposed model.

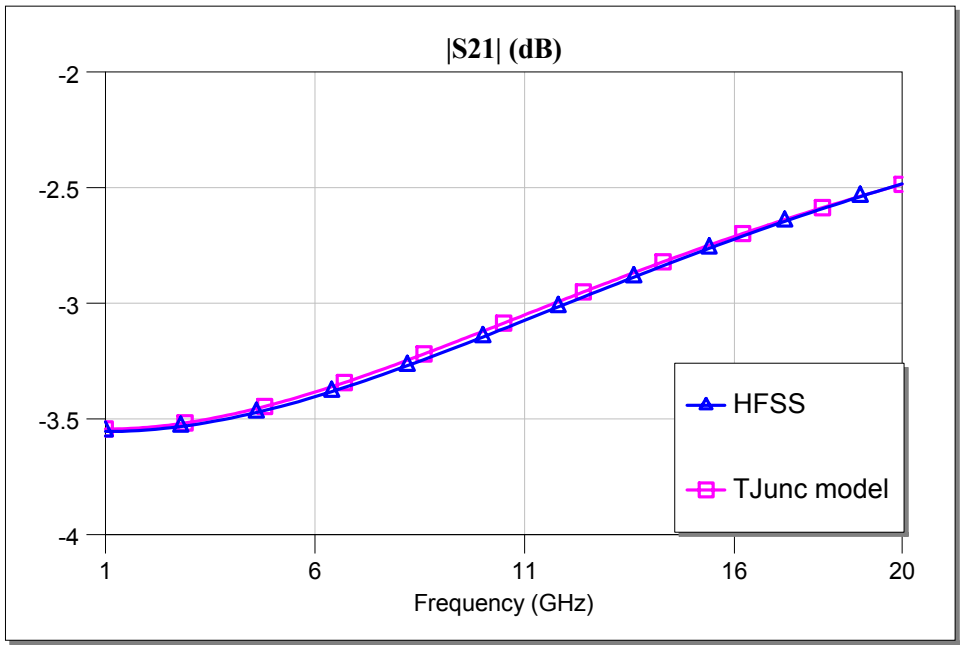

(c) Comparison of $|S_{21}|$ for the simulated T-junction and proposed model.

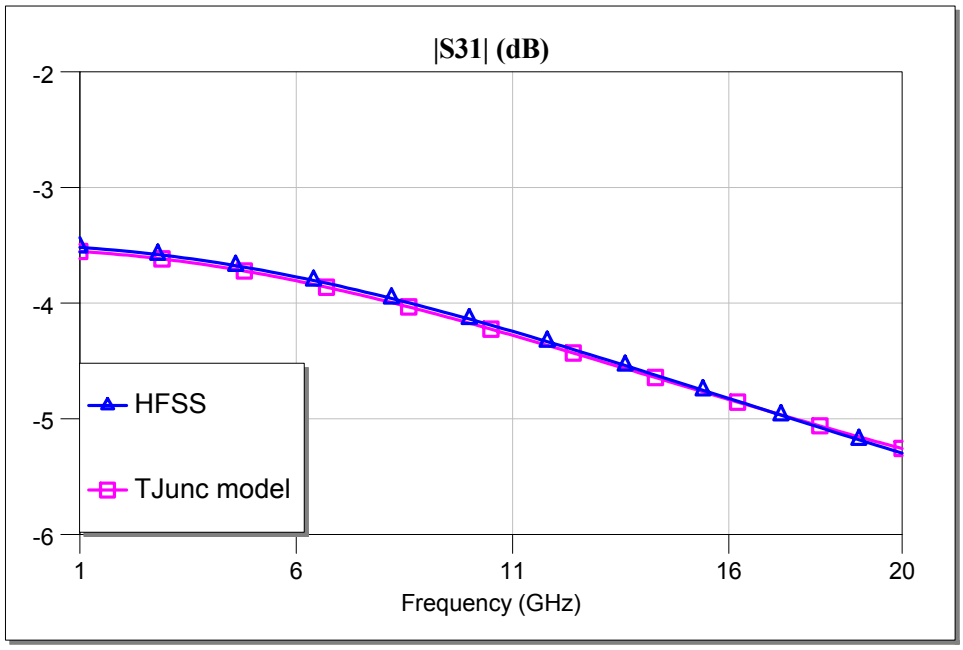

(d) Comparison of $|S_{31}|$ for the simulated T-junction and proposed model.

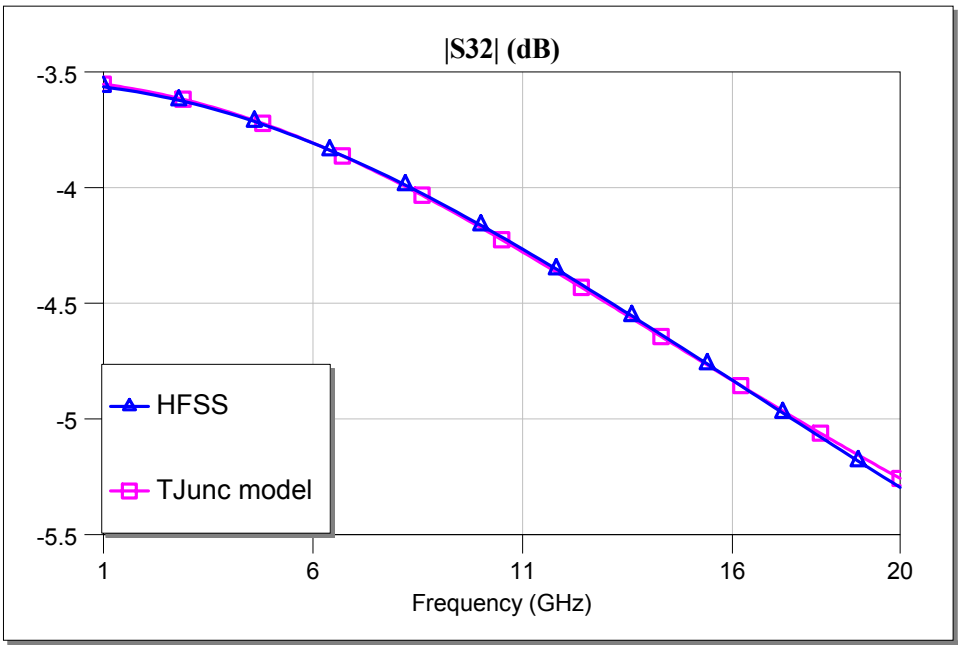

(e) Comparison of $|S_{32}|$ for the simulated T-junction and proposed model.

Figure 3.13 (a) to (e) S-parameters of the EM simulated and modeled T-junction.

It was mentioned before that the stubs should have only an imaginary part for an ideal solution and the modeled stubs have real parts that are large enough to affect the whole device characteristics. The analytical solution including the effects of all the losses, and hence, real parts is possible, but not feasible even with the mathematical solvers such as Matlab or Mathematica. So, two methods are used in this problem. First, the ideal double stub matching solution is applied. Since the device has three stubs, the third stub is only used to convert the given load another load value. Every switch on the third stub is closed, forming a different load for the remaining two stubs. Then, the required susceptances values are found by the double stub matching solution, and the bridge number that gives the closest susceptance value is selected. Since the double stub matching has two sets of solutions, and there are 40 bridges on the third stub, the first method was

expected to have 80 sets of solutions. However, since the non-idealities such as losses and affects of T-junctions were not included; the number of solutions with input reflection less than 20dB for the ideal double stub matching reduces to about 10 for a given load.

As the second method, all possible switch combinations are searched to find any possible switch combination with a lower input reflection using Matlab. Since each stub has 40 bridges, we had totally 64000 combinations. With this method, generally, approximately 10 solutions found which give an input reflection less than 30dB. The computer calculation just ends in less than a few seconds, so the second method is more feasible for the research purposes. To compare the results of two methods, their solutions are applied to a sample case. The program used for simulations is Microwave Office and the circuit used for simulations is in Figure 3.14 below.

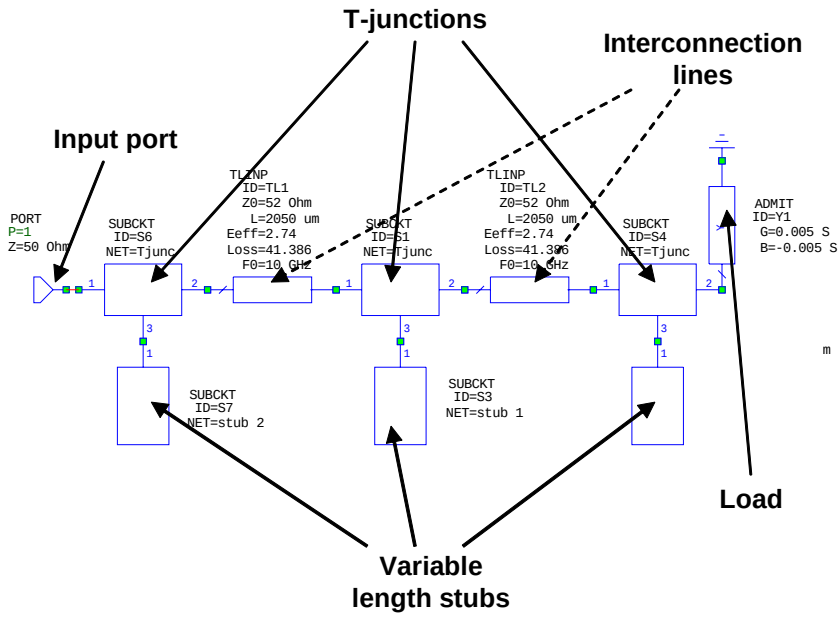

Figure 3.14 The Microwave Office circuit used for final simulations.

The variable stubs in the figure insert the input impedance of the variable length stub which was given is Table 3.7 to the circuit. The T-junctions have the schematic and element values given in Figure 3.12. Interconnection lines have a physical length of 2050μm and a characteristic impedance of 52Ω. Actually, they were designed to be a 50Ω line with *λ/8* electrical length at 10GHz for a dielectric constant of 5.75, but since the true dielectric constant is 4.6, some shifts arise in the characteristic impedance and the electrical length of those lines. Fortunately, the whole device performance is almost independent of the characteristic impedance and the electrical length of the interconnection lines. This is another advantage of variability of the MEMS impedance matcher. The comparison of two methods can be seen in Figure 3.15 where the device matches 100+j100Ω to 50Ω. The input reflections for the first and second methods are -23dB and -38 dB respectively. It is also clear that even though both methods work, the method of searching all possible solutions gives more accurate results.

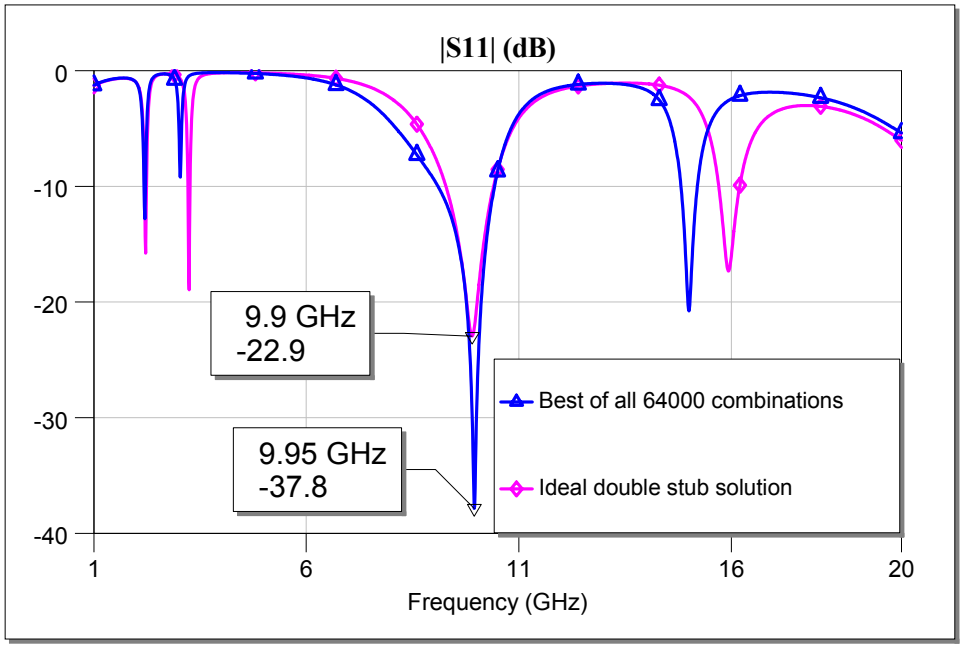

Figure 3.15 The comparison of solutions selected from ideal set and all combinations.

To check the device performance for other types of impedance transformations, the device is simulated to transform some other impedance values to other desired values. In Figure 3.16, the device was set to match 50Ω to j25Ω, and it successfully matches to 0.4 + j24.9Ω. Another example is in the same figure, where the device is set to match j200Ω to 15Ω, and matches to 0.02+j15.2Ω.

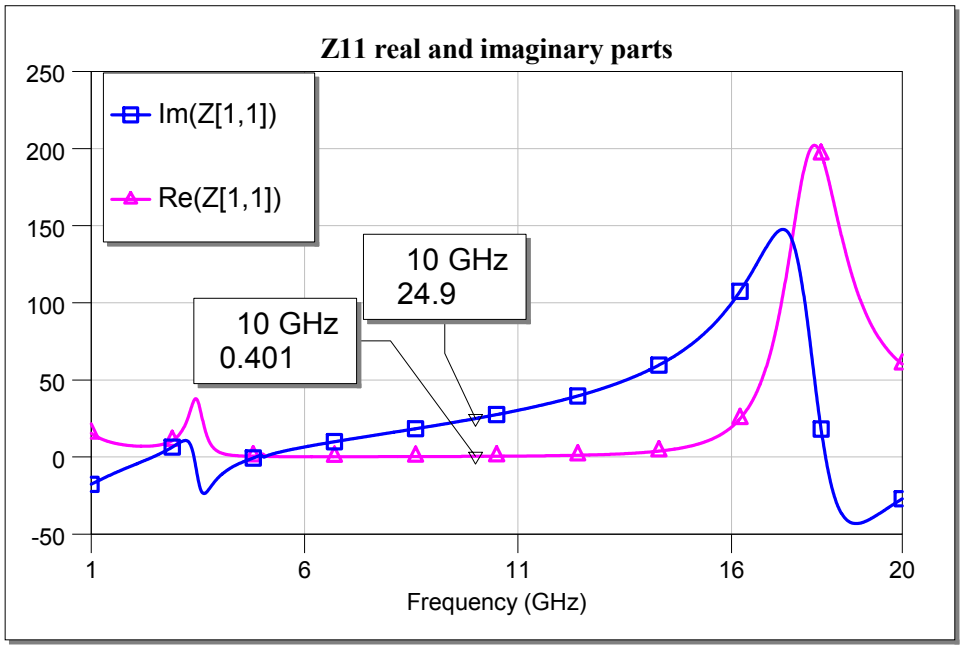

(a) The matcher was set to match 50Ω to j25Ω.

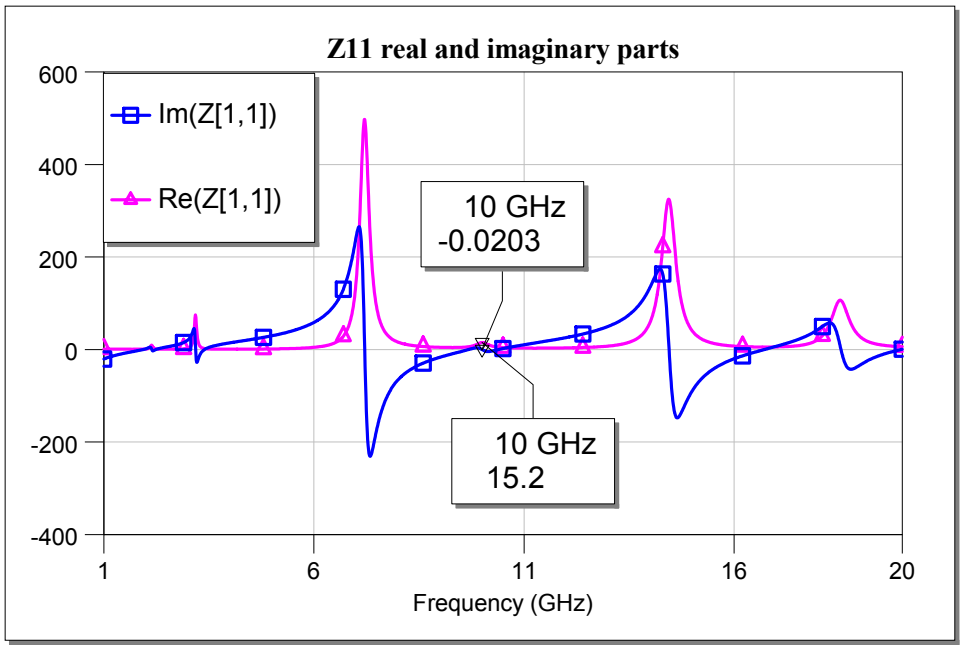

(b) The matcher was set to match j200Ω to 15Ω.

Figure 3.16 (a) to (b) Real and imaginary parts of input impedance seen into the matcher when it is set to transform different impedances to desired values.

3.5 Conclusion

As a conclusion, it seen from the simulation results, which consider all the possible nonidealities, the variable triple stub matcher is able to transform any given load to any desired load. For most of the cases, there exists many more than one solution to the given problem. The adjustability property of the device extends the device application widely. A direct application area is the multiple-frequency systems. Although fixed length transmission lines are used in the device which means a very narrow band of operation, the device can be set to work in a very wide band with its adjustability property. The device is also independent of the end capacitance of the stub, which is the MEMS switch down state capacitance, removing an important disadvantage of production

nonidealities. The device is expected to work for frequencies greater than 10GHz since the electrical lengths can smaller for these frequencies. The limitation here is the cut-off frequency of the MEMS switches which is greater than 40GHz. The bottom limit for the operation frequency is expected about 1GHz range where the MEMS switch capacitance drops significantly. The device is also a candidate for any multi-frequency or reconfigurable system with its wide range of impedance transforming capability.

CHAPTER IV

FABRICATION OF THE MEMS IMPEDANCE MATCHER

This chapter gives the details of the fabrication of the adjustable MEMS impedance matcher. The MEMS impedance matcher is fabricated using surface micromachining technology which is based upon thin film techniques. There are metal and dielectric layers deposited using methods such as sputtering, evaporation, and electroplating. These layers are patterned using methods such as wet, dry, reactive ion etching (RIE), and lift-off.

The fabrication procedure has three steps; mask design, process development, and fabrication. The mask design is the first step to transform the designs into real structures. The masks are used to build the moulds which are used to pattern the material underneath using the lithography technique. The masks are drawn in the computer environment using Cadence program. After the masks are drawn, they are produced in the mask production facilities.

The process optimization is the next step towards the fabrication of the MEMS impedance matcher. The processing work and the fabrication of the

devices designed during the study of this thesis were done in the microelectronic facilities of Middle East Technical University. The process optimization step requires the deposition of each layer in the predefined thickness without any difference drawn from the mask. The material properties such as conductivity and residual stress should also be adjusted by tuning the deposition conditions. Since each layer requires different physical and chemical conditions for deposition, the processing of each material must be altered such that material deposited in a layer must not be affected or be spoilt during the deposition of coming layers. After the optimization of deposition of each layer is completed, the whole device is fabricated with predefined conditions of processing, and the fabrication is completed.

This chapter gives the whole details about the fabrication of the MEMS impedance matcher. The first subsection gives information about the masks. The second subsection explains the properties of the materials and their deposition techniques. And the final subsection describes the whole process flow for the device production.

4.1 Mask Drawing

It is important to visualize the device structure to be able to understand the mask design. In Figure 4.1, the general device structure of the MEMS impedance matcher can be seen. In the figure, there are three layers and a substrate. The first metallization is the layer used for all CPW lines and DC routings which are needed for the actuation of the MEMS bridges. The second metallization is the layer that is used for building the suspended MEMS bridges. To prevent DC shorting between the first and the second metallization layers, an isolation layer is used.

To pattern three layers of the structure during the fabrication phase, four mask layers are needed. First mask layer is used to pattern the first metallization layer which is made of Titanium-Copper-Gold. The second mask layer defines which parts of the silicon nitrate will be opened during patterning. This is required for having DC contacts for testing. The third mask selects again the opening areas where the second metallization will contact to the first metallization upon the dielectric layer. This mask, in other words, is used to open the places for mechanical contacts, anchors, of the MEMS bridges. And the final mask layer defines the places where MEMS bridges will lie.

The mask drawings used for the production of the MEMS impedance matcher and MEMS variable length stubs can be seen in Figure 4.2. There are three stubs as the name triple stub matcher requires. There are 40 MEMS bridges on every stub with 100μm spacing and 100μm width, meaning that 40 different discrete stub length positions for each stub. To total die size is 8950 x 5720μm^2. The feature size of the masks is 1μm.

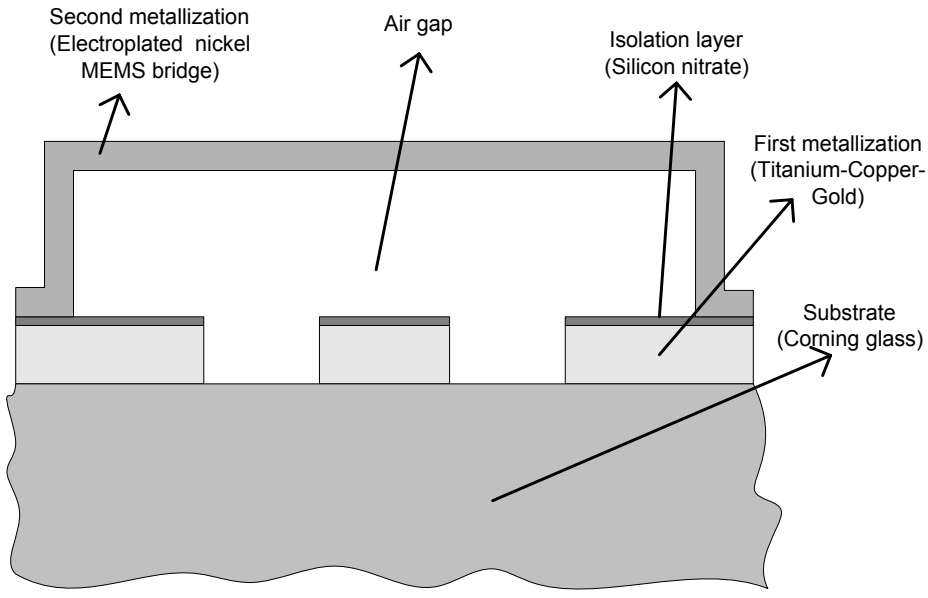

Figure 4.1 General device structure of the MEMS impedance matcher.

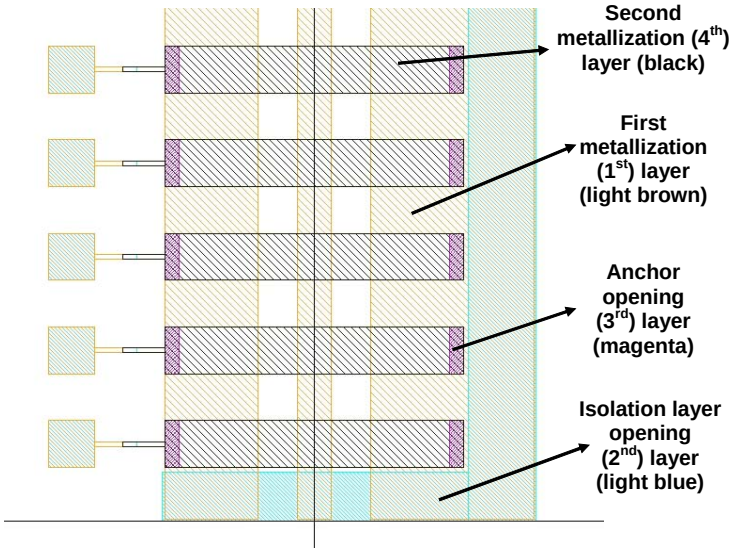

(a) A closer view of the masks drawn.

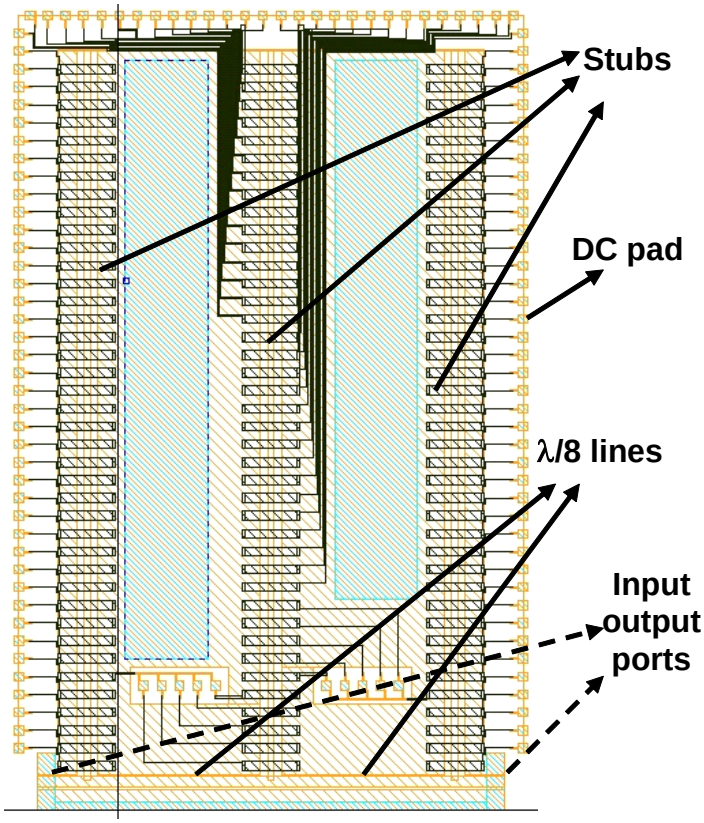

(b) Whole layout of the MEMS impedance matcher.

Figure 4.2 (a) to (b) Masks drawn for the production of the MEMS variable length stub.

4.2 Materials Used and Their Deposition Techniques

Selection of the materials for a MEMS process has crucial importance. Selecting the material with the highest conductivity or lowest stress may not give the best performance for the whole device. The reason for this is that deposition and patterning of some materials is somewhat "harder" than the others. They may require very high temperatures to be deposited or very powerful acids to be patterned, and this situation may damage the other layers, resulting with unhealthy devices. So, feasibility of the materials selected should be considered as much as the material properties.

Considering material performance and deposition conditions, the following materials are selected for the 4 layers of the process (3 layers explained before, and the sacrificial layer which will be explained) with the following criteria:

- Substrate: Pyrex 7740 corning glass is selected as the substrate material. The main reason for selecting this material is its low cost, which is about 25$ per wafer. It is not actually designed for high frequency applications because it has a dielectric loss tangent of 0.005. This value is not accepted as a "low amount of loss". The wafer has a thickness of 500μm preventing it to be very fragile. It has a dielectric constant of 4.6.
- First metallization: Since the device is designed to work at high frequencies about 10GHz, the conductivity and the thickness of the first metallization layer become more important. Copper is selected for its high conductivity (5.7×10^7 S/m). Copper is deposited using the electroplating technique to obtain a thickness about 2μm. This thickness is required for two reasons; first, the conductivity of electroplate copper is less than bulk copper, and second, the devices are electrically too long so they suffer

from the losses. These two facts increase the loss of the device; hence 2μm can decrease the loss level to acceptable values such as 0.75dB/cm (measured unloaded line loss). A seed layer is required for electroplating which is also selected as copper and has a thickness of 0.3μm. Thicknesses less than this value cause nonuniformity in the current distribution and this ends up with nonuniformity in the electroplated copper thickness. In addition to that, the seed copper layer does not adhere to glass, so an additional adhesion layer, Titanium, is used to improve copper adhesion to glass. This additional layer has a thickness of 100-200Å. The adhesion layer, Titanium, and the seed layer, Copper, are deposited using the sputtering technique at 150°C. Finally, a cover layer is used to prevent oxidation of the first metallization layer, and to protect the underlying electroplated Copper layer during the etching of adhesion and seed layers. This layer is Gold with a thickness of 0.3μm, deposited with evaporation technique, and patterned with lift-off technique. The process flow for the first metallization can be seen in Figure 4.3.

- Isolation layer: Application of DC voltage between the first and the second metallization layers is required to actuate the MEMS bridges on the stubs. Isolation layer is used to prevent DC shorting of first and second metallization layers when voltage is applied. For the isolation layer, the important parameters are its dielectric constant, thickness, breakdown voltage, and roughness of the surface. The dielectric constant and the thickness directly determine the down state capacitance of MEMS bridges, so they are vital parameters of the design. The breakdown voltage is also dependent upon the thickness and the thickness must be adjusted so that the layer should not go into breakdown when the actuation voltage is applied to switches. Another important parameter is the surface roughness of the layer. It was reported in [21] that the down state capacitance of the bridges reduce to 50% of its value if surface roughness exceeds 100Å. For this layer, silicon nitrate is (Si_3N_4) is selected. It has strong endurance to

many chemicals. Its physical strength is also advantage, because MEMS bridges distort the isolation layer after actuated several times, and this causes the devices become damaged. It has a relative dielectric constant of 7. It is deposited with a thickness ranging in 0.1-0.3μm.

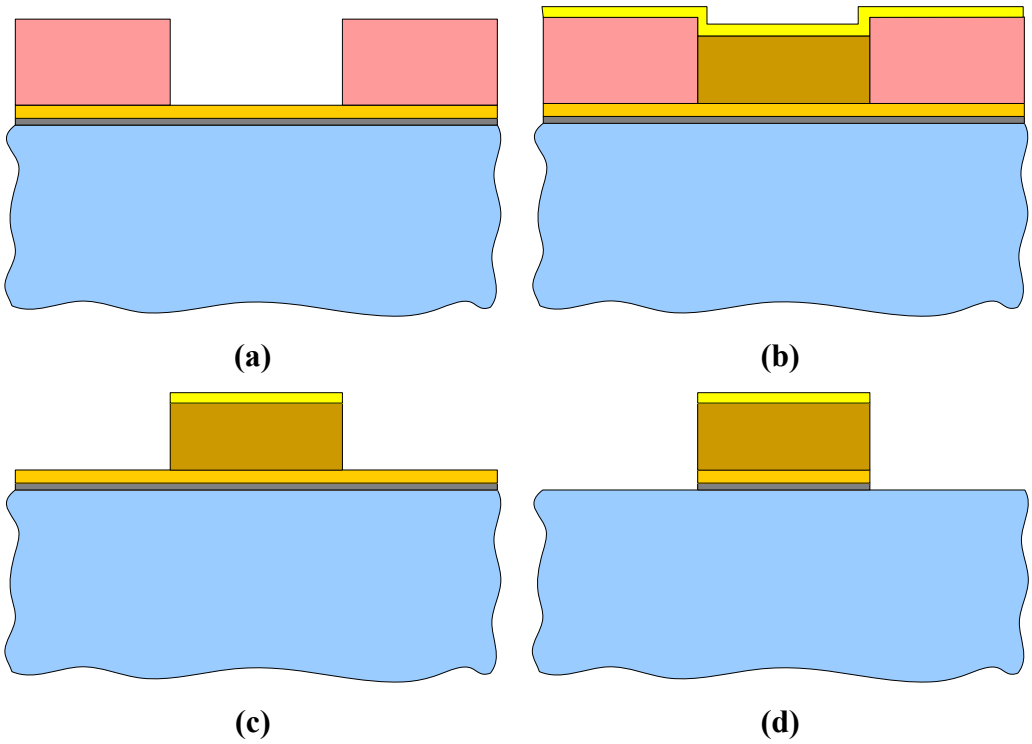

Figure 4.3 Process flow for the first metallization **(a)** Adhesion layer Ti (gray) and seed layer Cu (light brown) are coated, and photoresist is coated and patterned for electroplating (pink). **(b)** Cu is electroplated for first metallization (dark brown), and Au coated as the cover layer (yellow). **(c)** Au is patterned using lift-off technique. **(d)** Ti and seed Cu layers are etched. Cover Au layer protects the electroplated Cu underneath during the etching.

- Sacrificial layer: Sacrificial layer is a temporary layer of the process. The second metallization, which is used for the MEMS bridges and will be finally suspended, is built upon the sacrificial layer. The thickness of the photoresist determines the separation between the first and the second metal layers. This is the most important design parameter, since it directly determines on and off state capacitance and the actuation voltage. Shipley Microposit S1828 photoresist is used for the sacrificial layer. Generally, it is the most difficult part of the whole fabrication process to remove the sacrificial layer, because the structures are very fragile and they can be pealed off easy while the sacrificial layer is removed. Since the photoresist is easily removed with acetone, it is a good choice for the sacrificial layer. But it has an important disadvantage which is the temperature dependency of the photoresist. The hardbake temperature of the photoresist is 120°C and it is very hard to remove it when it stays some time in an environment with temperature around 100°C. Sticktion is a serious problem during the release, i.e., the removal of the sacrificial layer. The reason for the sticktion is that the liquid (acetone or water) comes into the place of photoresist, and the second metallization layer collapses over the first metallization layer while the liquid evaporates. If this is the case, it is not possible to level the second metallization layer again, and therefore the devices will not operate. To avoid this problem, the sacrificial layer is either removed with plasma asher or critical point drying is used. In the critical point drying step, CO_2 is inserted in a closed environment while the liquid is evaporated, preventing the second metal layer to stick upon the first metal layer.
- Second metallization: The second metallization layer is used to build the top of the MEMS bridges. Nickel is selected for this layer, and electroplating method is used. This is because a layer thickness of 1μm is required for the design. As in the Copper electroplating case, a seed layer

is required. Because of this, another Ti(adhesion of Cu)/Cu(seed for electroplating) layer is sputtered after the sacrificial layer is deposited. The important parameters are again conductivity, thickness, and stress of the material. Conductivity of the material is important since it again directly affects the losses inserted by the MEMS bridge. The thickness of the layer again changes the loss inserted by the MEMS bridge, and the actuation voltage of the MEMS switch is very strongly dependent upon it. The stress is again another parameter affecting the mechanical characteristic of the device. It is a determiner of the spring constant, and hence the actuation voltage of the MEMS bridge. The residual component of the stress is very important also for the reason that the MEMS bridge must be as flat as possible. The residual stress occurring during the deposition of the electroplated Ni results with buckling of the MEMS bridges, and the device ends up with a lower performance. The residual stress of the material is related with the deposition temperature and the current density of the electroplating.

4.3 Process Flow

The steps followed during the fabrication of the MEMS impedance matcher can be seen in Figure 4.4 below. In Figure 4.4 (a), sputtered Ti and Cu layers are coated. Cu layer is the seed required used for electroplating and Ti layer is the adhesion layer between Cu and the glass substrate. The mold layer for electroplating is S1813 photoresist is coated and patterned afterwards. In Figure 4.4 (b), Cu is coated using the electroplating technique and after that Au layer that prevents oxidation is coated. In Figure 4.4 (c), the S1813 photoresist is removed in acetone, also removing Au layer over it. This removal technique of Au is called lift-off. In Figure 4.4 (d), sputtered Cu and Ti layers are etched using wet etching using different etchants. During this step, Au layer acts as a protecting layer of

electroplated Cu layer. In Figure 4.4 (e), Si_3N_4 layer is coated as the isolation layer using plasma enhanced chemical vapor deposition technique (PECVD). Also, S1813 photoresist is coated and patterning for the patterning operation of Si_3N_4. Then in Figure 4.4 (f), Si_3N_4 is patterned using the reactive ion etching (RIE) technique. S1813 photoresist is removed with acetone after Si_3N_4 is removed. In Figure 4.4 (g), S1828 photoresist, the sacrificial layer, is coated and patterned to be able to build suspended structures. Again, sputtered Ti and Cu are needed here as the adhesion and seed layers of the second electroplating process. In Figure 4.4 (h), S1813 is coated and patterned as the mold layer for Ni electroplating process. Then, Ni is electroplated to the areas which are left open by the S1813 mold layer. And in Figure 4.4 (i), S1813 mold layer is removed with acetone first. Then, sputtered Ti and Cu are etched as in the first metallization layer process. After this etching, the samples are diced, and finally the sacrificial layer S1828 is removed using acetone or photoresist stripper. The structures must be put into IPA after acetone and released using the critical point drying. In this technique, CO_2 is put slowly instead of IPA which was in the place of S1828 photoresist in a closed environment. By this way, sticktion of the structures is prevented and the structures are left suspended in the air.

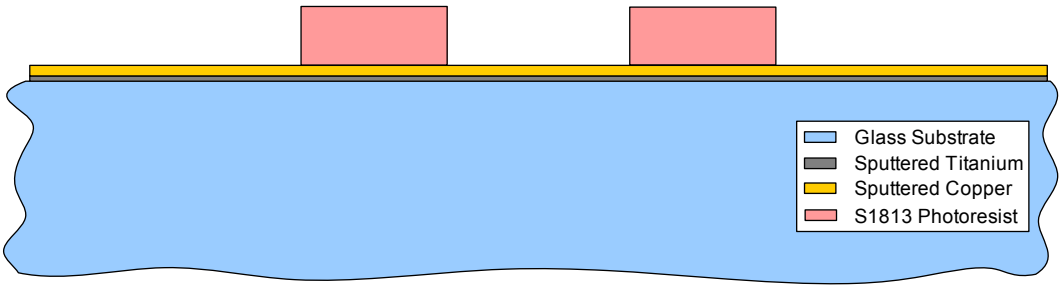

(a) Photoresist coated over sputtered Ti/Cu.

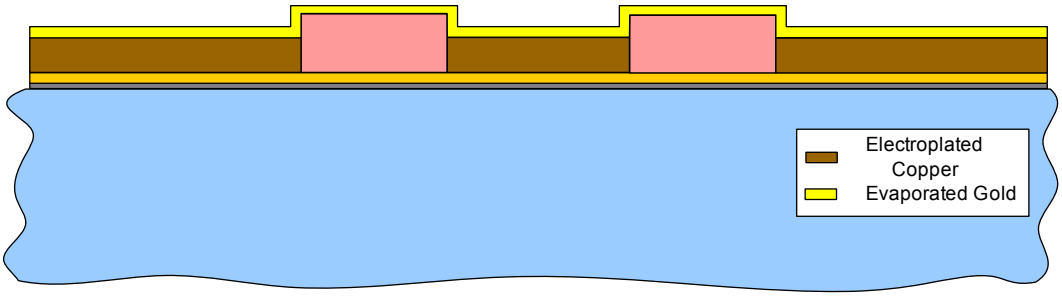

(b) Cu is electroplated and Au is evaporated.

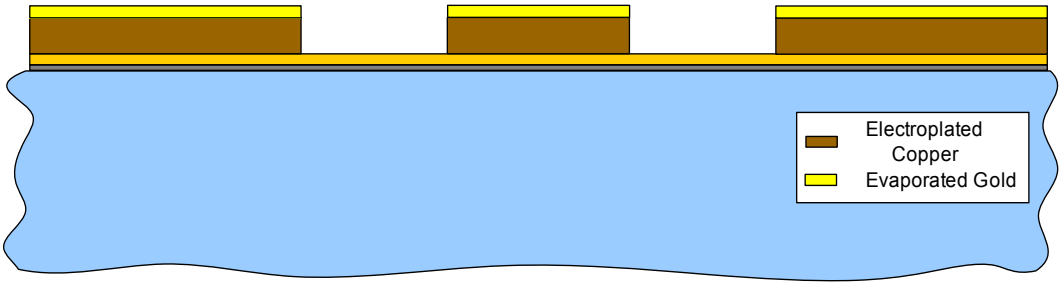

(c) Au is removed with lift-off.

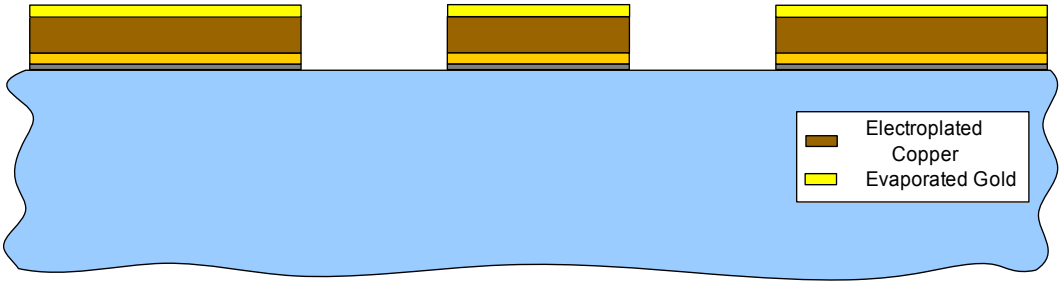

(d) Seed Ti/Cu is etched.

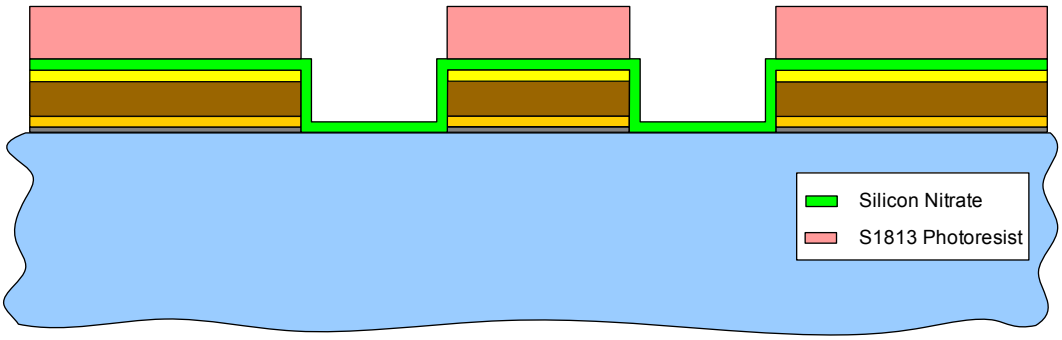

(e) Silicon nitride is coated, and photoresist is coated for patterning.

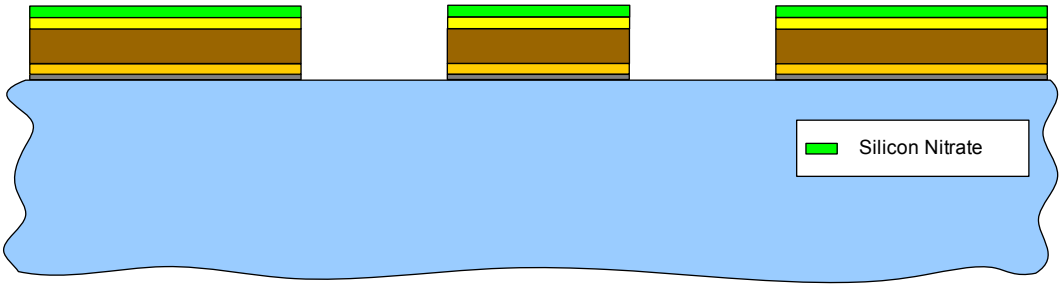

(f) Silicon nitride is removed with RIE.

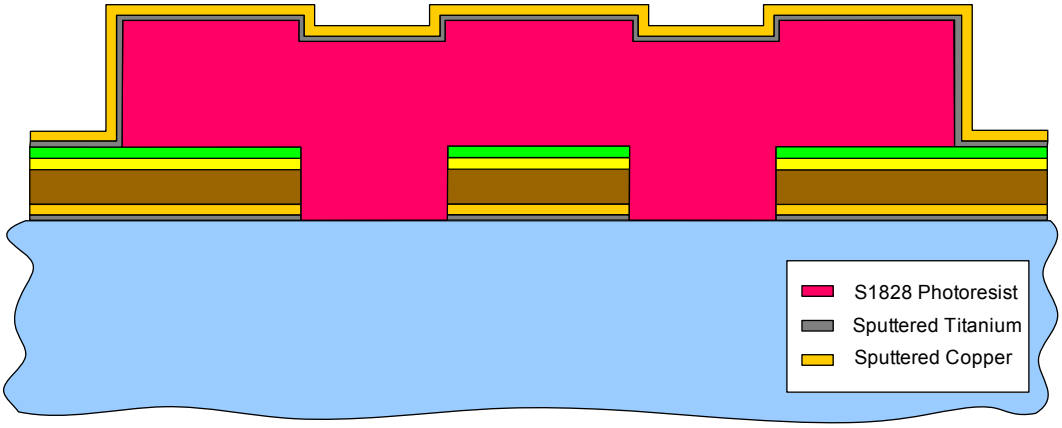

(g) Photoresist is coated as sacrificial layer, and Ti/Cu is sputtered for Ni electroplating.

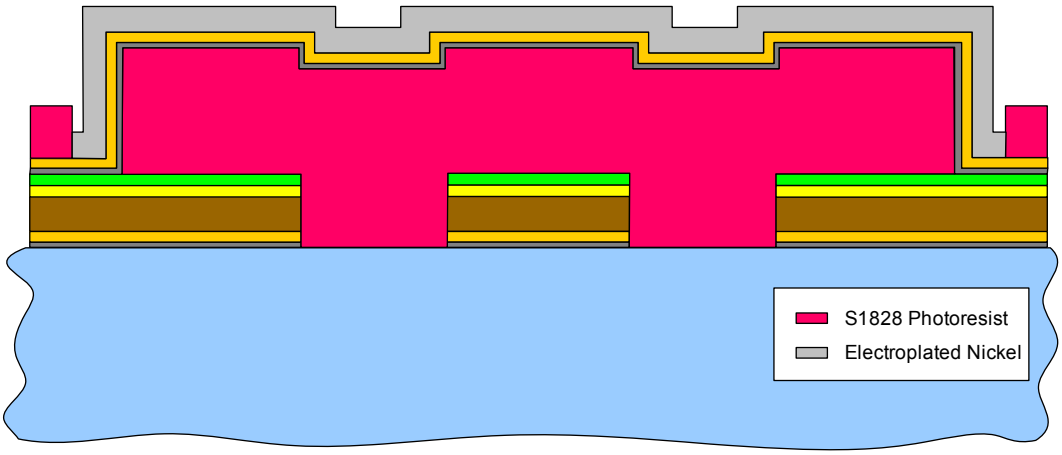

(h) Mold photoresist is coated for Ni plating and Ni is electroplated.

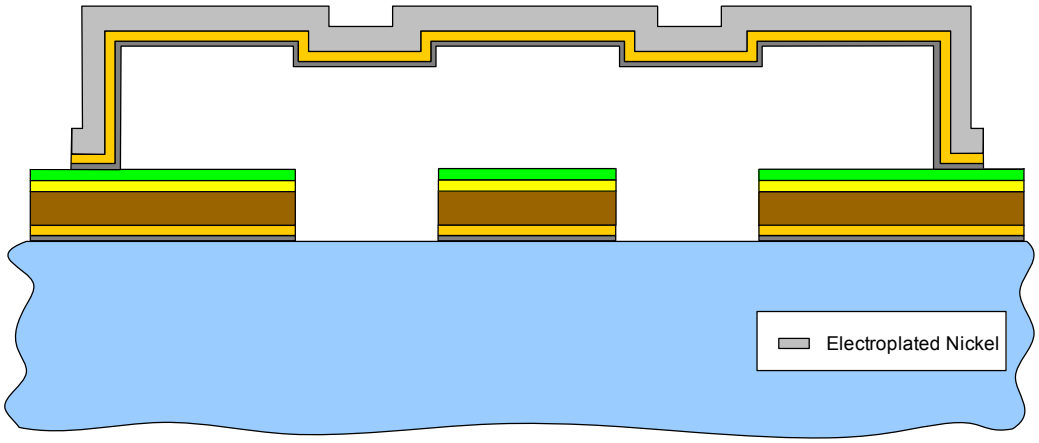

(i) Mold photoresist is removed, Ti/Cu is etched, and sacrificial photoresist is removed.

Figure 4.4 (a) to (i) The process flow followed during the production of MEMS impedance matchers.

CHAPTER V

FABRICATION AND TEST RESULTS OF THE MEMS IMPEDANCE MATCHER

The testing of the MEMS impedance matcher is as important as its fabrication and requires care. The testing of the devices require a well-calibrated measurement setup, because errors occurring during the testing phase can misdirect the designer about understanding the device behavior.

The testing actually goes parallel with the fabrication. Every layer of the structure is monitored during fabrication. This is required to have mechanically alive structures at the end of the fabrication. The first phase of the testing is the visual check. The devices are checked under the microscope at any phase of the fabrication to control any defects on the devices. Another visual checking mechanism is scanning electron microscope (SEM). SEM lets us see 3-D views of the MEMS impedance matcher.

Other than the visual monitoring of the process, some measurements are also made one of which is the testing of the first metallization. The loss inserted by the MEMS impedance matcher is dominated by the loss of the first

metallization. So, the first metallization of the structures should be tested and the fabrication must be paused until acceptable values are obtained. The testing of the first metallization has two parts which are four-point probe resistivity measurement and RF measurement. In the first type, the resistivity of the first metallization is found that is supported by the thickness information coming from SEM measurements. The second type is the RF measurement. A CPW is measured and since its characteristics is well-known, the first metallization material properties are tuned to fit the measured characteristics.

At the end of the fabrication procedure, the devices are again checked under the microscope. Then to ensure that MEMS bridges are alive, AC voltage is applied and movement of the bridge is observed. If they are alive, an SEM session is also done. With the SEM session, it can be more clearly ensured that the MEMS bridges are suspended. It is also possible to measure the dimensions of each part of the device. Since the dimensions of the device directly change the characteristics of the device, accurate measurement of them helps us to guess the device performance. For example, the sacrificial layer thickness directly changes the up state capacitance of the MEMS bridges and the actuation voltage.

After visually seeing that the devices are reliable, the next step is to check the mechanical characteristic of the device. DC voltage is applied to MEMS bridges to examine the safe actuation of the bridges. The actuation voltage is measured in this step as well. And finally, the RF measurements are done by means of a network analyzer and a probe station.

This chapter presents the measurement setups used and measurements obtained of the MEMS variable impedance matcher. The first subsection introduces the RF measurement setup and details of RF measurement. The following subsections give the tests results of the CPWs and MEMS variable

length stub. And the final subsection gives the SEM photographs taken of the fabricated devices.

4.4 RF Measurement Setup

RF measurements of the MEMS variable impedance matcher are done using HP 8720D 0.5-20 GHz vector network analyzer and Cascade Microtech Summit 9000 manual probe station. Picoprobe 40A-GSG-150P CPW probes are used at the connection points of the probe station to the devices. The photograph of the setup can be seen in Figure 0.1 below.

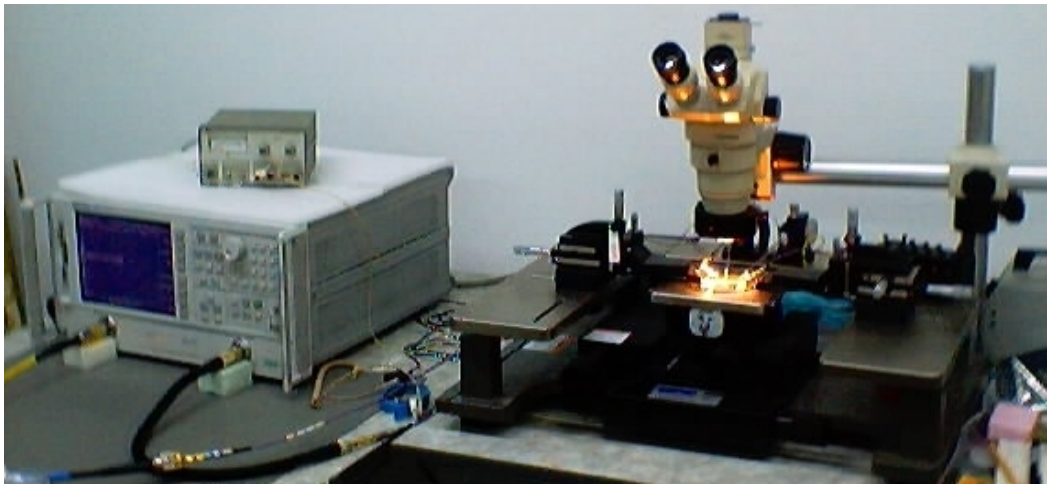

Figure 0.1 Photograph of the RF testing setup used for MEMS variable impedance matcher measurements.

Several types of errors, which significantly change the device response, are inserted by measurement system, so calibration is required during the testing. Making calibration is just trying to calculate the errors inserted by the measurement device parts (such as probes, connection cables, or adapters) or

discontinuities at the connection of those parts. For this purpose, some devices with well-known characteristics are measured first and their responses are compared with the ideal expected characteristics. From the difference between the ideal and the measured results of these known devices, the errors inserted by the whole measurement system is calculated, and in a sense "subtracted" from the response of the real device to be measured. This operation is basically similar with the multimeter calibration where the probes of the multimeter are shorted to each to other before the measurement to exclude the resistances coming from the cables or the probes.

There are several different calibration techniques in the literature [80]-[81]. They all use different models and require different calibration standards (known devices) to calculate the errors. The method used in the measurement of the MEMS impedance matcher is the short-open-load-thru (SOLT) calibration technique. The names short-open-load-thru are the names of the calibration standards used during the calibration. With this calibration technique, it is possible to remove the following errors: directivity, source match, load match, reflection tracking, transmission tracking, and crosstalk [81]-[84].

The performance of the calibration standards and the RF probes is also very important for an accurate calibration. The standards should be precisely produced and well-characterized. They also should be produced on the same wafer with the devices to be measured if possible. To satisfy these needs, probe station manufacturers produce impedance standard substrates (ISS) which include all the necessary calibration standards such as short, open, load etc. The ISS should be compatible with the probes also. In the measurements of MEMS impedance matcher, Picoprobe ISS CS-5 and probes (Picoprobe 40A-GSG-150P) are used. Some data of the ISS and probe should be known and inserted into the VNA for the calculations such as thru line delay, open circuit capacitance or short

circuit inductance [80]. The values used in the SOLT calibration used for the measurements can be seen in Table 0.1.

Table 0.1 Calibration coefficients of Picoprobe 40A-GSG-150P CPW probe [79].

Calibration Standard Name	**Calibration Coefficient (For Calibration Substrate CS-5)**
Open	C_0 = 6.5fF or Offset Length = 98μm
Short	L_0 = 8.8pH or Offset Length = 53μm
Load	0.0080ps long, 5Ω line (for HP)
Thru	1ps (for Cascade ISS PN101-190)

4.5 First Metallization Measurements

The measurements for the first metallization are very important to guess the performance of the final device. The first metallization is composed of four layers as given in Figure 4.3. It is mainly made of electroplated Cu (1.5-2μm), but a very thin Ti/Cu (100/3000Å) layer is sputtered underneath as a seed layer for the electroplating. An Au (1000-2000Å) layer is also used for protecting the electroplated Cu layer from oxidation and further processing steps. Of course, this composite structure affects the resistivity of the whole metallization. Especially, Ti has a much lower conductivity, 0.27×10^7 S/m, compared to Cu (5.8×10^7 S/m) and Au (4.1×10^7 S/m), which increases the losses for the first metallization. The conductivity of the whole first metallization layer is measured as $4\text{-}5\times10^7$ S/m with the four-point probe technique. The thickness and conductivity of the electroplated Cu directly affects the losses considerably, so electroplating setup must be adjusted to get an optimum thickness and conductivity. Another source of measured loss is the loss coming from the dielectric. For Pyrex 7740, the loss

tangent is given as 0.005 at 1MHz, which is not a low value for high frequency devices. There are no reported values about the loss of this substrate at higher frequencies to our knowledge, but we expect that the dielectric loss may be more affective in the X-band. The simulated and measured first metallization characteristics for a sample 22000μm CPW line can be seen in Figure 0.2. The discrepancies on the S_{21} characteristics mostly come from the defects on the CPW line and the calibration efficiency. Here, for the 2μm thick line, the measured loss is 0.75 dB/cm which is acceptable.

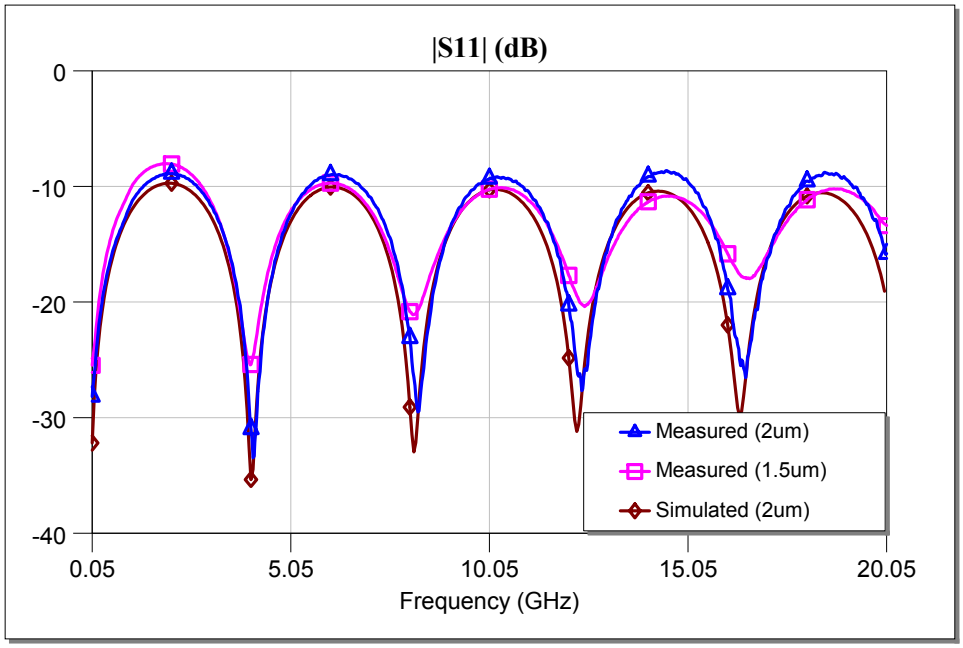

(a) Simulated and measured $|S_{11}|$ characteristics.

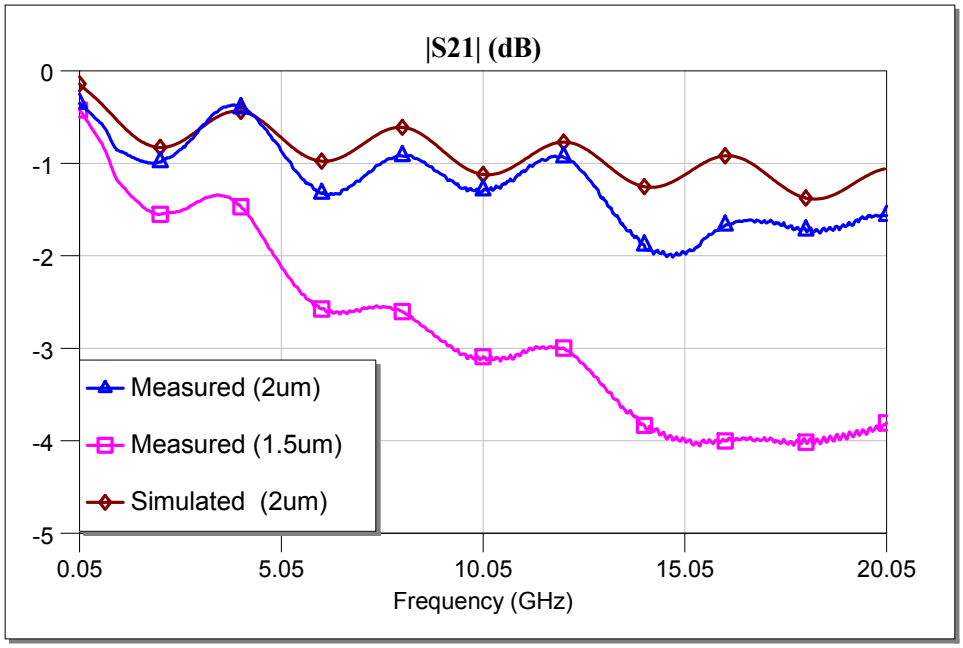

(b) Simulated and measured $|S_{21}|$ characteristics.

Figure 0.2 (a) to (b) Simulated and measured S-parameters of the first metallization.

4.6 Stub Measurements

The stub measurement is the only measurement obtained up to date during the development of the MEMS adjustable impedance matcher. The reason for not obtaining a measurement result for the whole device is the defective isolation layer. Since it is the silicon nitride layer that isolates first and second metal layers, defects on this layer directly results with short circuits between these two layers. This prevents us to apply DC voltages to MEMS bridges which means that the device becomes nonfunctional.

The simulation and results for a separate, 20-bridge, and short-circuited stub can be seen in Figure 0.3. Here, no voltage is applied to the device, and the short circuit is the metallic short circuit at the position of the 20th bridge. In other words, this is the up-state measurement result of the stub. The characteristics are close to each other which means that all bridges are mechanically alive.

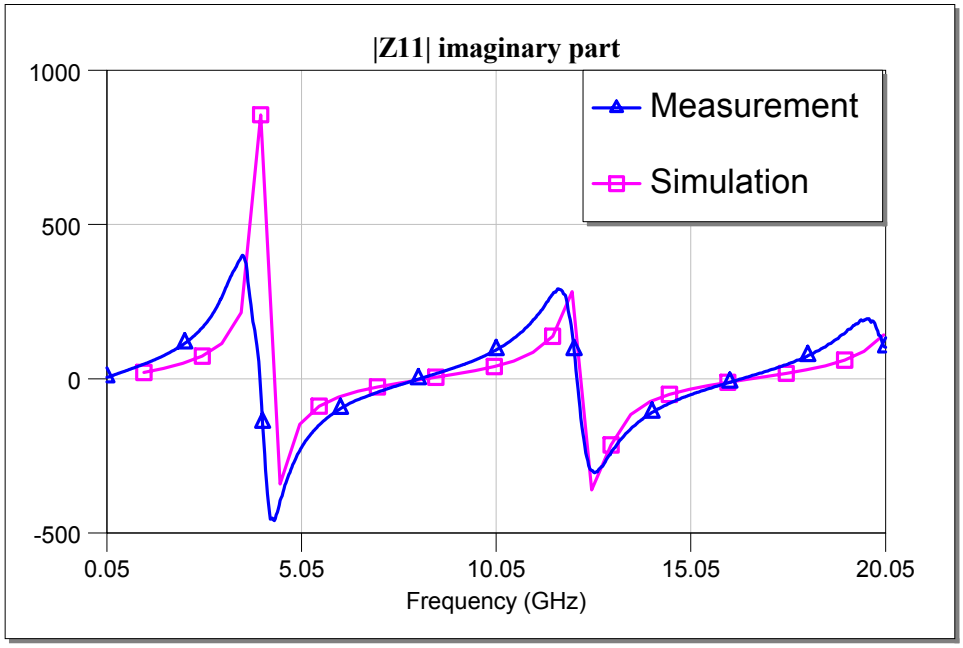

(a) Imaginary part of Z_{11} for the 20-bridge MEMS short circuited stub.

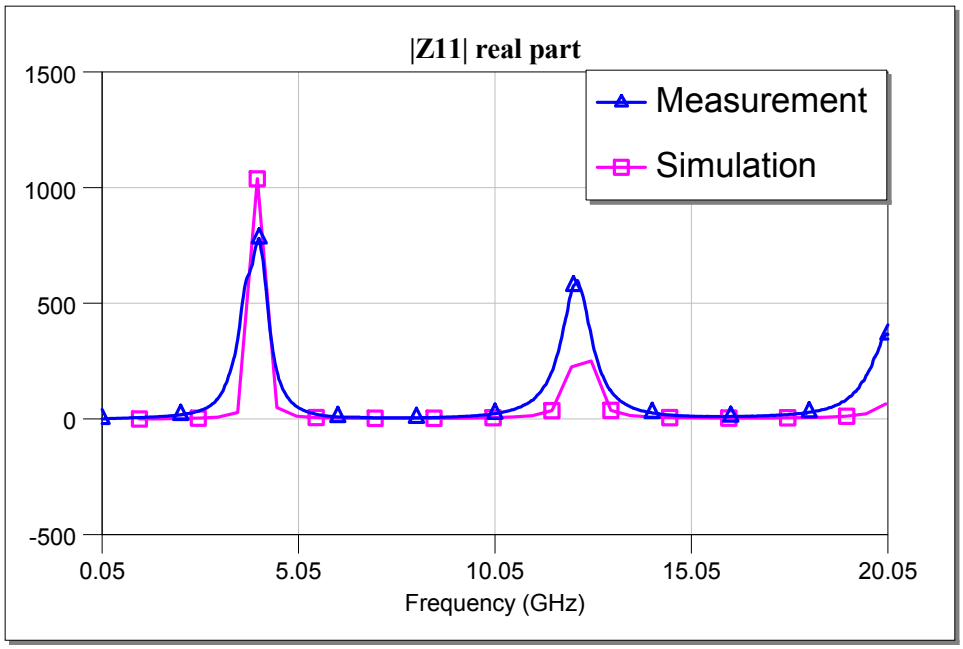

(b) Real part of Z_{11} for the 20-bridge MEMS short-circuited stub.

Figure 0.3 (a) to (b) Measurement results for the 20-bridge MEMS short-circuited stub.

4.7 SEM Pictures

Although the devices are not fully functional, they are mechanically alive. In order to show that the structures are alive, scanning electron microscope (SEM) photographs of the devices were taken. SEM photos of the MEMS impedance matching network can be seen in Figure 0.4, Figure 0.5, and Figure 0.6. The SEM device used is in the Microelectronics Laboratories of METU and was denoted by ASELSAN.

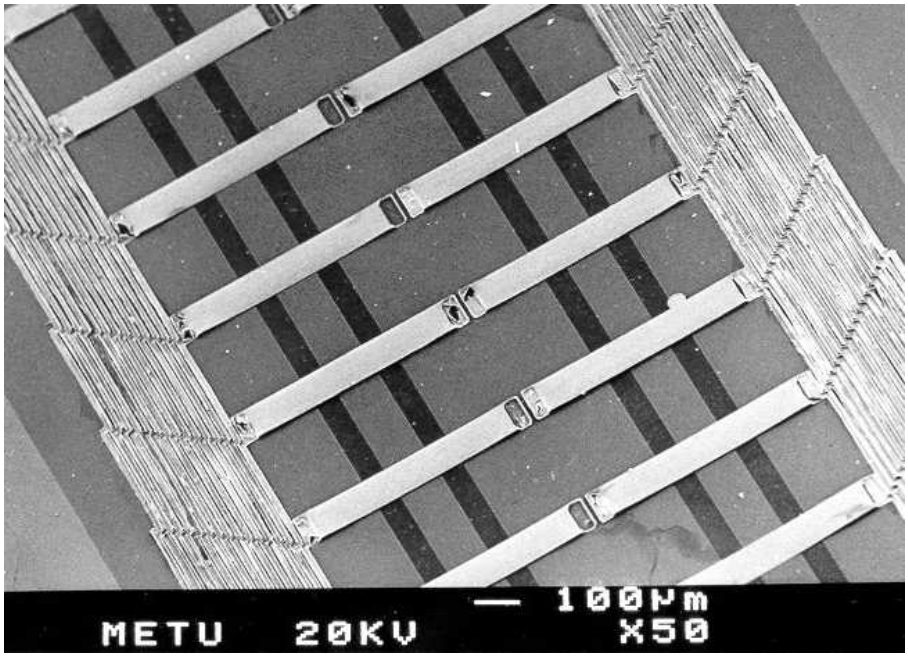

Figure 0.4 Two stubs of the MEMS adjustable impedance matching network.

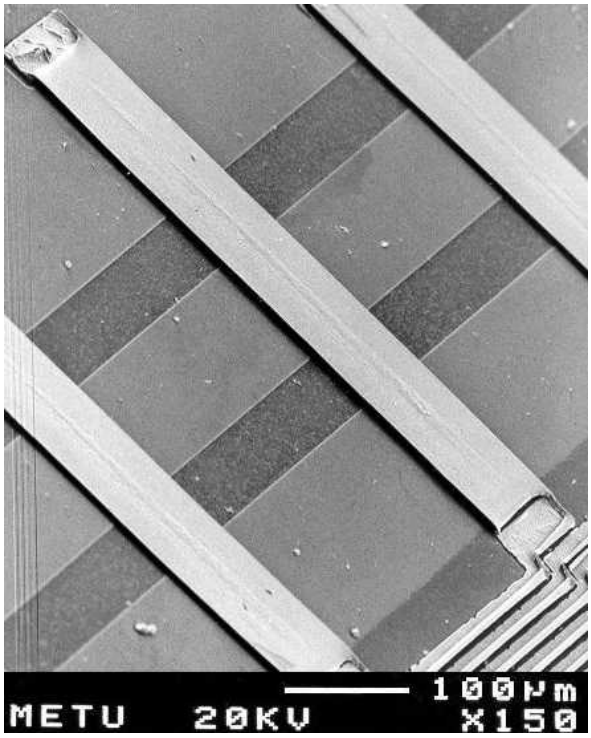

Figure 0.5 A closer view of a stub of the MEMS impedance matching network.

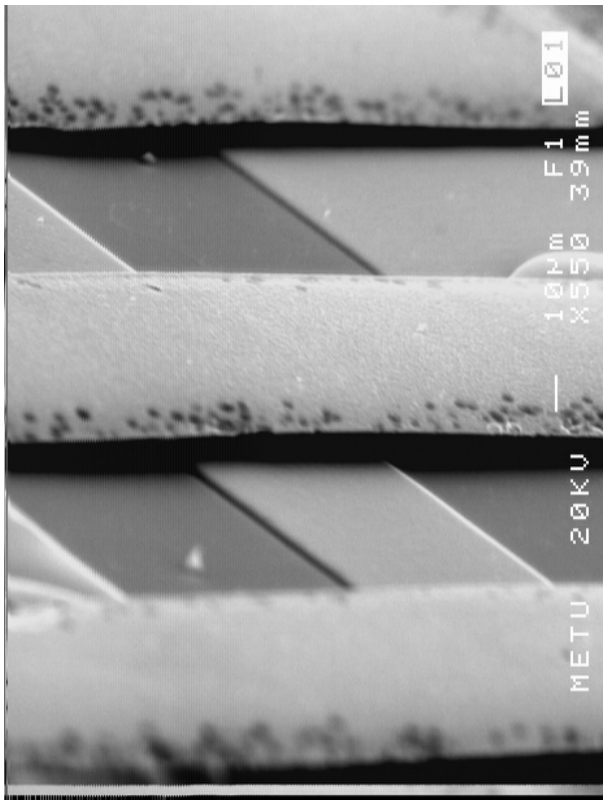

Figure 0.6 Close view of the MEMS bridge that is used to load the CPW.

CHAPTER VI

CONCLUSION AND FUTURE WORK

The research presented in this thesis involves development of a novel adjustable impedance matching network. The device is based on the basic triple stub matching theory. With this technique, the device is capable of making transformations to every point on the Smith chart. The adjustability property of the device is obtained using variable length stubs. These stubs are implemented by placing shunt, capacitive MEMS switches evenly on the stub. The whole device is fabricated monolithically using the surface micromachining technology.

Based on the achievements up to date of this research, the following conclusions can be drawn:

1. A fixed-fixed beam, low loss, high isolation, shunt, capacitive MEMS switch is designed, modeled, and fabricated. The switch design is used as for capacitive loading of the variable length stub. A novel and more accurate model is developed for the characterization of the switch.
2. A capacitively terminated variable length stub is designed, modeled, fabricated, and measured. The stub is implemented upon coplanar waveguide and is loaded with MEMS switches. The

variability of the stub is achieved by closing the MEMS switch at the required length, and making a capacitive termination to ground. The new model developed for the MEMS switch is applied to the stub design, and verified with the electromagnetic simulations. Since the stub is adjustable, the design is independent of the line losses and end capacitances which may vary between different runs of the process.

3. An adjustable impedance matching network is designed, modeled, and fabricated. The device is designed using the triple stub matching method and modeled with the new model developed for the capacitively loaded MEMS stubs. The final simulations are made using this new model and the affects of T-junctions are also included.
4. The domestic process for the fabrication of the RF MEMS devices at the Microelectronic facilities of Middle East Technical University is mostly completed. Cu electroplating method is applied for the first metallization of the device, and the problems of high quality patterning and high losses are solved. The development of the structural layer, which is used for building MEMS bridges, is completed. The stress problems are solved optimizing the electroplating environment. Also, a major problem of the surface micromachining, sacrificial layer release, is solved for our case using the critical point drying technique.

Although the modeling of the device is fully completed and the development of the fabrication process is almost finished, some more worked is required for a fully optimized device:

1. The silicon nitride isolation layer processing should be optimized to solve the shorting problems occurring in the device.

2. An optimization work should be carried to optimize the first metallization to reduce the conductor losses. A new method should be developed to embed the thick first metallization into the substrate.
3. New MEMS switches should be designed with lower actuation voltages and better performance.
4. The band of the impedance matching network can be improved with new techniques. The device can be furthermore investigated and modified for multi-frequency operation.
5. Novel structures can be designed such as power divider and vector modulator with the idea of adjustable impedance matching technique.

As a result, with the new model developed for RF modeling of the device and processing experience gained, we believe that we made a significant contribution to the development of MEMS technology in our country. Our aim is to keep this research going and finally arrive to the target of development of domestic technology in our country. We hope that we will continue our way with more support and partners.

REFERENCES

[1] W. Bischof, "Variable impedance tuner for MMICs," IEEE Microwave Guided Wave Lett., June 1994, pp. 172–174.

[2] C. E. McIntosh, R. D. Pollard, and R. E. Miles, "Novel MMIC source impedance tuners for on-wafer microwave noise-parameter measurements," IEEE Trans. Microwave Theory Tech., Feb. 1999, pp. 125–131,.

[3] J. H. Sinsky and C. R. Westgate, "Design of an electronically tunable microwave impedance transformer," IEEE MTT-S International Digest, June 1997, pp. 647–650.

[4] L. E. Larson, R. H. Hackett, M. A. Melendes, and R. F. Lohr, "Micromachined microwave actuator (MIMAC) technology – a new tuning approach for microwave integrated circuits," Microwave and Millimeter-Wave Monolithic Circuits Symposium Digest, June 1991, pp. 27-30.

[5] J.J. Yao, M. F. Chang, "A surface micromachined miniature switch for telecommunications applications with signal frequencies from DC up to 4 GHz," The 8th International Conference on Solid-State Sensors and Actuators Digest, June 1995, pp. 384-387.

[6] C. Goldsmith, J. Randall, S. Eshelman, T. H. Lin, D. Denniston, S. Chen, B. Norvell, "Characteristics of micromachined switches at microwave frequencies," IEEE MTT-S International Digest, June 1996, pp. 1141 -1144.

[7] S. P. Pacheco, C. T. Nguyen, and L. P. B. Katehi, “Micromechanical electrostatic K-band switches,” IEEE MTT-S International Digest, June 1998, pp. 1569-1572.

[8] S. P. Pacheco, C. T. Nguyen, and L. P. B. Katehi, “Design of low actuation voltage RF MEMS switch,” IEEE MTT-S International Digest, June 2000, pp. 165-168.

[9] J. Y. Park, G. H. Kim, K. W. Chung, and J. U. Bong, “Fully integrated Micromachined capacitive switches for RF applications,” IEEE MTT-S International Digest, June 2000, 283-286.

[10] J. Y. Park, G. H. Kim, K. W. Chung, and J. U. Bong, “Electroplated RF MEMS capacitive switches,” IEEE International Conference on Microelectromechanical Systems, January 2000, 639-644.

[11] S.-C. Shen and M. Feng, “Low actuation voltage RF MEMS switches with signal frequencies from 0.25 to 40 GHz,” IEEE International Electronics Devices Meeting Proceedings, December 1999, pp. 689-692.

[12] C. Chang and P. Chang, “Innovative micromachined microwave switch with very low insertion loss,” Sensors and Actuators, vol. 89, pp. 71-75, 2000.

[13] D. Hyman, A. Schmitz, B. Warneke, T. Y. Hsu, J. Lam, J. Brown, J. Schaffner, A. Walston, R. Y. Loo, G. L. Tangonan, M. Mehregany, and J. Lee, “Surface Micromachined RF MEMS switches on GaAs subtrates,” International Journal of RF Microwave CAE, vol. 9, no. 4, pp. 348-361, 1999.

[14] M. Sakata, Y. Komura, T. Seki, K. Kobayashi, K. Sano, and S. Horike, “Micromachined relay which utilizes single crystal silicon electrostatic actuator,” IEEE International Conference on Microelectromechanical Systems, pp. 21-24, 1999.

[15] P. M. Zavracky, N. E. McGruer, R. H. Morrison, and D. Potter, "Microswitches and microrelays with a view toward microwave applications," International Journal of RF Microwave CAE, vol. 9, no. 4, pp. 338-347, 1999.

[16] C. Bozler, R. Drangmeister, S. Duffy, M. Gouker, J. Knecht, L. Kushner, R. parr, S. Rabe, and L. Travis, "MEMS microswitch arrays for reconfigurable distributed microwave components," IEEE MTT-S Digest, June 2000, pp. 153-156.

[17] D. Hah, E. Yoon, and S. Hong, "A low voltage actuated Micromachined microwave switch using torsion springs and leverage," IEEE MTT-S International Digest, June 2000, pp. 157-160.

[18] P. Blondy, D. Mercier, D. Cros, P. Gullion, P. Rey, P. Charvet, B. Diem, C. Zanchi, L. Lapierre, J. Sombrin, and J. B. Quoirin, "Packaged mm-wave thermal MEMS switches," European Microwave Conference, September 2001, vol. 1, pp.283-286.

[19] M. Ruan, J. Shen, and C. B. Wheeler, "Latching micromagnetic relays," IEEE Journal of Microelectromechanical Systems, vol. 10, pp. 511-517, December 2001.

[20] Y. Wang, Z. Li, D. T. McCormick, and N. C. Tien, "Low-voltage lateral-contact microrelays for RF applications," IEEE International Conference on Microelectromechanical Systems, January 2002, pp.645-648.

[21] G. Rebeiz, "RF MEMS Theory, Design, and Technology," John Wiley & Sons, 2003.

[22] J. Y.-C. Chang, A. A. Abidi, and M. Gaitan, "Large suspended inductors and their use in a 2μm CMOS RF amplifier," IEEE Electron Devices Letters, vol. 14, pp. 246-248, May 1993.

[23] H. Jiang, Y. Wang, J.-L. A. Yeh, and N. C. Tien, "On-chip spiral inductors suspended over deep copper-lined cavities," IEEE Transactions on Microwave Theory and Techniques, vol. 48, no.12, pp. 2415-2423, December 2000.

[24] G. W. Dahlmann, E. M. Yeatman, P. R. Young, I. D. Robertson, and S. Lucyszyn, "MEMS high Q-microwave inductors using solder surface tension self-assembly," IEEE MTT-S International Digest, June 2001, pp. 394-403.

[25] J.-B. Yoon, B.-K. Kim, C.-H. Han, E. Yoon, K. Lee, and C.-K. Kim, "High-performance electroplated solenoid-type integrated inductor (SI^2) for RF applications using simple 3D surface micromachining technology," IEEE International Electron Devices Meeting, December 1998, pp. 544-547.

[26] A. Dec and K. Suyama, "Micromachined electro-mechanically tunable capacitor and their applications to RF IC's," IEEE Transactions on Microwave Theory and Techniques, vol. 46, no.12, pp. 2587-2595, December 1998.

[27] J. Zou, C. Liu, and J. Schutt-Aine, "Development of a wide tuning-range two-parallel-plate tunable capacitor for integrated wireless communications," International Journal of RF Microwave CA, vol.11, pp. 322-329, August 2001.

[28] J. Y. Park, Y. J. Yee, H. J. Nam, and J. U. Bu, "Micromachined RF MEMS tunable capacitors using piezoelectric actuators," IEEE MTT-S International Digest, May 2001, pp. 2111-2114.

[29] R. L. Borwick, P. A. Stupar, J. DeNatale, R. Anderson, C. Tsai, and K. Garnett, "A high-Q, large tuning range, tunable capacitor for RF applications," IEEE International Conference on Microelectromechanical Systems, January 2002, pp.669-672.

[30] C. L. Goldsmith, A. Malczewski, Z. L. Yao, S. Chen, J. Ehmke, and D. H. Hinzel, "RF MEMS variable capacitors for tunable filters," International Journal of RF Microwave CA, vol.9, pp. 362-374, July 1999.

[31] N. Hoivik, A. Michalicek, Y. C. Lee, K. C. Gupta, and V. M. Bright, "Digitally controllable variable high-Q MEMS capacitor for RF applications," IEEE MTT-S International Digest, May 2001, pp. 2115-2118.

[32] J. W. Digby, C. E. McIntosh, G. M. Parkhurst, B. M. Towlson, S. Hadjiloucas, J. W. Bowen, J. M. Chamberlain, R. D. Pollard, R. E. Miles, D.

P. Steenson, L. S. Karatzas, N. J. Cronin, and S. R. Davis, “Fabrication and characterization of Micromachined rectangular waveguide components for use at millimeter-wave and terahertz frequencies,” IEEE Transactions on Microwave Theory and Techniques, pp. 1293-1302, 2000.

[33] K. J. Herrick, J. G Yook, and L. P. B. Katehi, “Microtechnology in the development of three-dimensional circuits,” IEEE Transactions on Microwave Theory and Techniques, pp. 1832-1844, December 1998.

[34] V. Milanovic, M. Gaitan, E. D. Bowen, and M. E. Zahloul, “Micromachined microwave transmission lines in CMOS technology,” IEEE Transactions on Microwave Theory and Techniques, pp. 630-635, December 1997.

[35] C. T.-C. Nguyen, “Micromechanical resonators for oscillators and filters,” IEEE Ultrasonics Symposium, pp. 489-499, 1995.

[36] K. Wang and C. T.-C. Nguyen, “VHF free-free beam high-Q micromechanical resonator,” Journal of Microelectromechanical Systems, pp. 347-360, 2000.

[37] V. K. Varadan, K. J. Vinoy, and K. A. Jose, “RF MEMS and their applications,” John Wiley & Sons, 2003.

[38] N. S. Barker and G. M. Barker, “Optimization of distributed MEMS transmission line phase shifters – U-band and W-band designs,” IEEE Transactions on Microwave Theory and Techniques, pp. 1957-1966, November 2000.

[39] J. S. Hayden and G. M. Rebeiz, “Very low loss distributed X-band and Ka-band MEMS phase shifters using metal-air-metal capacitors, IEEE Transactions on Microwave Theory and Techniques, January 2003.

[40] H.-T. Kim, J.-H. Park, Y.-K. Kim, and Y. Kwon, “V-band low loss and low-voltage distributed MEMS digital phase shifter using metal-air-metal capacitors,” IEEE MTT-S International Digest, pp. 341-344, June 2002.

[41] Y. Liu, A. Borgioli, A. S. Nagra, and R. A. York, "K-band 3-bit low loss distributed MEMS phase shifter," IEEE Microwave Guided Wave Letters, vol. 10, no.10, pp. 415-417, October 2000.

[42] A. Malczewski, S. Eshelman, B. Pillans, J. Ehmke, and C. L. Goldsmith, "X-band RF MEMS phase shifters for phase array applications," IEEE Microwave Guided Wave Letters, vol. 9, no.12, pp. 517-519, December 1999.

[43] C. Quan et al., "Wideband X-band phase shifters using metal-to-metal contact RF switches," Workshop on MEMS for Antenna Applications, IEEE APS International Symposium, July 2000.

[44] M. Kim, J. B. Hacker, R. E. Mihailovich, and J. F. DeNatale, " A DC-to-40 GHz four-bit RF MEMS true-time delay network," IEEE Microwave Wireless Components Letters, vol. 11, no. 2, pp. 56-58, February 2001.

[45] G. L. Tan, R. E. Mihailovich, J. B. Hacker, J. F. DeNatale, and G. M. Rebeiz, "A very-low-loss 2-bit X-band RF MEMS phase shifter" IEEE International Microwave Symposium Digest, June 2002.

[46] B. Pillans, S. Eshelman, A. Malczewski, J. Ehmke, and C. L. Goldsmith, "Ka-band RF MEMS phase shifters," IEEE Microwave Guided Wave Letters, vol. 9, no. 12, pp. 520-522, December 2002.

[47] R. Simons, D. Chun, and L. P. B. Katehi, "Micromechanical systems actuators for antenna reconfigurability," IEEE MTT-S International Digest, pp. 215-218, June 2001.

[48] D. M. Pozar, S. D. Tagonski, and H. D. Syrigos, "Design of millimeter wave microstrip reflectarrays," IEEE Transactions of Antennas and Propagation, vol. 45, no. 2, pp. 287-296, May 1998.

[49] J. C. Chiao, S.-Y. Cheng, J. L. Chang, I. M. Chio, Y. Kang, and J. Hayasaka, "MEMS reconfigurable antennas," International Journal of RF Microwave CAE, vol. 11, pp. 301-309, 2001.

[50] J. Brank, J. Yao, M. Eberly, A. Malczewski, K. Varian, and C. L. Goldsmith, "RF MEMS-based tunable filters," International Journal of RF Microwave CAE, vol. 11, pp. 276-284, 2001.

[51] J.-H. Park, H.-T. Kim, Y. Kwon, and Y.-K. Kim, "Tunable millimeter-wave filters using coplanar waveguide and micromachined variable capacitors," Microengineering and Micromechanics, pp. 706-712, 2001.

[52] A. Abbaspour-Tamijani, L. Dussopt, and G. M. Rebeiz, "Miniature and millimeter-wave filters using MEMS capacitors," European Microwave Conference, pp. 813-815, September 2002.

[53] J.-C. Chiao, Y. Fu, D. Choudhury, and L.-Y. Lin, "MEMS millimeterwave components," IEEE MTT-S International Digest, pp. 463-466, 1999.

[54] H.-T. Kim, S. Jung, K. Kang, J.-H. Park, Y.-K. Kim, and Y. Kwon, "Low-loss analog and digital micromachined impedance tuners at the Ka-Band," IEEE Transactions on Microwave Theory Techniques, vol. 49, pp. 2394–2400, December 2001.

[55] J. Papapolymerou, K. L. Lange, C. L. Goldsmith, A. Malczewski, and J. Kleber, "Reconfigurable double-stub tuners using MEMS switches for intelligent RF front-ends," IEEE Transactions on Microwave Theory Techniques, vol. 51, pp. 271–278, January 2003.

[56] H. Sagkol, K. Topalli, M. Unlu, O. A. Civi, S. S. Koc, S. Demir, and T. Akin, "A monolithic phased array with RF MEMS technology," IEEE APS International Symposium, pp. 760-763, June 2002.

[57] M. Unlu, K. Topalli, H. Sagkol, S. Demir, O. A. Civi, S. S. Koc, and T. Akin, "New MEMS switch structures for antenna applications," IEEE APS International Symposium, pp. 134, June 2002.

[58] M. Unlu, K. Topalli, H. Sagkol, S. Demir, O. A. Civi, S. S. Koc, and T. Akin, "RF MEMS adjustable impedance matching network and adjustable power divider," IEEE APS International Symposium, pp. 26-29, June 2002.

[59] H. Sagkol, “A phase shifter using RF MEMS technology,” M. Sc. Thesis, Middle East Technical University, September 2002.

[60] R. E. Collin, “Foundations for microwave engineering,” McGraw-Hill, 1992.

[61] C. P. Wen, “Coplanar waveguide: a surface strip transmission line suitable for non-reciprocal gyromagnetic device application,” IEEE Transactions on Microwave Theory Techniques, vol. 17, pp. 1087–1090, 1969.

[62] C. Veyres and V. F. Hanna, “Extension of the application of conformal mapping techniques to coplanar lines with finite dimensions,” Int. J. Electron, vol. 48, pp. 47-56, 1980.

[63] G. Ghione and C. U. Naldi, “Coplanar waveguides for MMIC applications: Effect of upper shielding, conductor backing, finite extent ground planes, and line-to-line coupling,” IEEE Transactions on Microwave Theory Techniques, vol. 35, pp. 260–267, 1987.

[64] S. S. Bedair and I. Wolff, “Fast, accurate, and simple approximate analytic formulas for calculating the parameters of coplanar waveguides,” IEEE Transactions on Microwave Theory Techniques, vol. 40, pp. 41–48, 1992.

[65] K. C. Gupta, R. Garg, I. Bahl, and P. Bhartia, “Microstrip line and slotlines,” Artech House, Inc., 1996.

[66] G. Hasnain et al., “Dispersion of picosecond pulses in coplanar transmission lines,” IEEE Transactions on Microwave Theory Techniques, vol. 34, pp. 738–741, 1986.

[67] N. K. Das and D. M. Pozar, “Full-wave spectral domain computation of material, radiation, and guided wave losses in infinite multilayered printed transmission lines,” IEEE Transactions on Microwave Theory Techniques, vol. 39, pp. 54–63, 1991.

[68] W. Hilberg, “From approximations to exact relations for characteristic impedances,” IEEE Transactions on Microwave Theory Techniques, vol. 17, pp. 259-265, 1969.

[69] D. M. Pozar, “Microwave engineering,” Addison-Wesley, 1990.

[70] M. J. W. Rodwell, S. T. Allen, R. Y. Yu, M. G. Case, U. Bhattacharya, M. Reddy, E. Carmen, M. Kamegawa, Y. Konishi, J. Pusl, and R. Pullela, “Active and nonlinear wave propagation devices in ultrafast electronics and optoelectronics,” Proceedings of IEEE, vol. 82, pp. 1037-1059, 1994.

[71] Corning 7740 wafer sheet, www.corning.com.

[72] G. Ghione, “A CAD-oriented analytical model for the losses of general asymmetric coplanar lines in hybrid and monolithic MICs,” IEEE Transactions on Microwave Theory Techniques, vol. 32, pp. 108-110, 1984.

[73] D. S. Phatak et al., “Dispersion characteristics of optically excited coplanar striplines: Comprehensive full-wave analysis,” IEEE Transactions on Microwave Theory Techniques, vol. 38, pp. 1719-1730, 1990.

[74] M. Y. Frankel et al., “Terahertz attenuation and dispersion characteristics of coplanar transmission lines,” IEEE Transactions on Microwave Theory Techniques, vol. 39, pp. 910-916, 1991.

[75] www.webelements.com

[76] R. N. Simons, “Coplanar waveguide circuits, components, and systems,” John-Wiley & Sons, 2001.

[77] M. Naghed, M. Rittweger, and I. Wolff, “A new method for the calculation of the equivalent inductances of coplanar waveguide discontinuities,” IEEE MTT-S International Symposium, pp. 747-750, 1991.

[78] M. Naghed and I. Wolff, “Equivalent capacitance of coplanar waveguide discontinuities and interdigital capacitors using a three-dimensional finite

difference method," IEEE Transactions on Microwave Theory Techniques, vol. 38, pp. 1808-1815, 1990.

[79] Picoprobe 40A-GSG-150P datasheet, GGB Industries, Inc.

[80] Application note, "On-wafer vector network analyzer calibration and measurements," Cascade Microtech.

[81] Application note, "Applying error correction to network analyzer measurements," Agilent AN 1287-3, Agilent Technologies.

[82] Product note, "Specifying calibration standards for the Agilent 8510 network analyzer," Agilent product note 8510-5B, Agilent Technologies.

[83] Product note, "Network analysis applying the 8510 TRL calibration for non-coaxial measurements," Agilent product note 8510-8A, Agilent Technologies.

[84] User manual, HP 8720D 0.5-20 GHz VNA.

APPENDIX

RF MEMS PROCESS FLOW

	Process Name		Conditions	Comments
Base Metallization	**Sputtering**	Ti	~125 counter @ ~125 C°	Presputtering should be considered.
		Cu	~2500 counter @ ~190 C°	
	PR coating	Spin	500 rpm dispense; 1500 rpm spin for both primer & S1813	3 ml. of primer and S1828 is sufficient
		SB*	115 C° on hotplate for 1 min.	
	Exposure		110 sec. exposure @ Karl Suss 8 sec. exposure @ EVG 620	
	Development		~3-5 min. @ MF-319	
	Copper Electroplating		Duration:2.5 min; Current: 2 A Solution @ room temp, pH=2.5-3.5	~2 µm thickness (estimated).
	Gold Evaporation		3 min. evaporation with 0.3g Au @ 100 A current flow	Thin gold layer deposition ~2000-2500 Å thickness
	PR Strip, Lift-off		Acetone @ room temp.	Buzzer with low power is recommended
	Copper seed etch		HNO_3:DI 1:160	Etching time is ~1-2 min.
	Titanium seed etch		HF:H_2O_2:DI 1:1:640	Etching time is ~1-1.2 min. Undercut warning.

Nitride coating and etching	**Nitride Coating**		PECVD oven	0.1-0.3 µm thick silicon nitride layer is obtained
	PR Strip	Spin	500 rpm dispense; 1500 rpm spin for both primer and S1813	3 ml. of primer and S1828 is sufficient
		SB	115 Cº on hotplate for 1 min.	
	Exposure		110 sec. exposure @ Karl Suss 12 sec. exposure @ EVG 620	
	Development		~3-5 min. @ MF-319	
	Post Bake		30 min. @ 130°C oven	
	Nitride Etching		Orthophosphoric acid @ 180ºC RIE *	Undercut warning for wet etching
	PR strip		Acetone	
Sacrifial layer & seed coating	**PR coating**	Spin	500 rpm dispense; 1500 rpm spin for both primer and S1828	3 ml. of primer and S1828 is sufficient for sacrificial layer formation.
		SB	115 Cº on hotplate for 1 min.	
	Edge Bead Removal		1000 rpm	
	Exposure		120 sec. exposure @ Karl Suss 20 sec. exposure @ EVG 620	
	Development		~3-5 min. @ MF-319	
	Baking before sputtering		5 min @ 115 Cº on hotplate	Essential to avoid cracks after sputtering.
	Sputter		~2500 counter @ room temp	Try not to overshoot temperature

Mold formation & Ni E-plating	**PR coating**	Spin	500 rpm dispense; 2000 rpm spin for both primer and S1828	3 ml. of primer and S1828 is sufficient for mold layer formation.
		SB	115 Cº on hotplate for 1 min.	
	Exposure		20 sec. exposure @ EVG 620	
	Development		~3-5 min. @ MF-319	

	Nickel Electroplating	Duration:30 sec; Current: 5.1 A Solution @ 50 C°, pH=3.5-4.5	1 µm thickness is estimated.
Release	**PR strip**	Acetone (room temperature)	
	Copper seed etch	$CH_3COOH:H_2O_2$:DI 1:1:18	Ni selective Cu etch
	Titanium seed etch	HF:H_2O_2:DI 1:1:640	Etching time is ~1-1.2 min. Undercut warning.
	Sacrificial resist removal	SVC-175 remover @50 C° for 30 min.	No deformation is observed on metallic surfaces. Be careful about the temp. of the chemical. It is flammable over 80 C°
	IPA Rinse	5 min. @ room temprature	Try to be quick while immersing the wafer to the solutions to avoid drying off and stiction.
	Critical Point Drying	CO_2 in IPA	